OULU 2023
C 872

ACTA UNIVERSITATIS OULUENSIS

Pekka Kantanen

THE ROLE OF FINELY DIVIDED RETAINED AUSTENITE ON THE MECHANICAL PROPERTIES OF QP AND ART PROCESSED NOVEL 0.3C ULTRAHIGH STRENGTH STEELS

UNIVERSITY OF OULU GRADUATE SCHOOL;
UNIVERSITY OF OULU,
FACULTY OF TECHNOLOGY

ACTA UNIVERSITATIS OULUENSIS
C Technica 872

PEKKA KANTANEN

THE ROLE OF FINELY DIVIDED RETAINED AUSTENITE ON THE MECHANICAL PROPERTIES OF QP AND ART PROCESSED NOVEL 0.3C ULTRAHIGH STRENGTH STEELS

Academic dissertation to be presented, with the assent of the Doctoral Programme Committee of Technology and Natural Sciences of the University of Oulu, for public defence in the Oulun Puhelin auditorium (L5), Linnanmaa, on 17 March 2023, at 12 noon

UNIVERSITY OF OULU, OULU 2023

Acta Univ. Oul. C 872, 2023

Supervised by
Professor Mahesh Somani
Professor Jukka Kömi

Reviewed by
Doctor Peter Sandvik
Associate Professor Ilchat Sabirov

Opponents
Professor Esa Vuorinen
Associate Professor Ilchat Sabirov

ISBN 978-952-62-3606-3 (Paperback)
ISBN 978-952-62-3607-0 (PDF)

ISSN 0355-3213 (Printed)
ISSN 1796-2226 (Online)

Cover Design
Raimo Ahonen

PUNAMUSTA
TAMPERE 2023

Kantanen, Pekka, The role of finely divided retained austenite on the mechanical properties of QP and ART processed novel 0.3C ultrahigh strength steels.
University of Oulu Graduate School; University of Oulu, Faculty of Technology
Acta Univ. Oul. C 872, 2023
University of Oulu, P.O. Box 8000, FI-90014 University of Oulu, Finland

Abstract

Both 0.3C (high) Si-Al and 0.3C medium-Mn steels are considered ideal recipes for developing the third-generation advanced high strength steels using the innovative quenching and partitioning (QP) and austenite reversion transformation (ART) treatments, respectively. This study reports the effects of QP and ART processing on the evolved microstructural characteristics, focusing on phase transformation behavior and resultant mechanical properties, augmented by the presence of finely divided retained austenite (RA). While QP processing trials were carried out with (high) Si-Al steels, both QP and ART treatments were utilized to optimize the processing of medium-Mn steels to achieve high strength-ductility combinations. The processes were later scaled up for laboratory rolling simulations, involving thermomechanical rolling followed by direct quenching and partitioning (TMR-DQP) in the case of (high) Si-Al steels, and TMR-QP and TMR-ART treatments for medium-Mn steels. The prime objective was to gain in-depth knowledge about the effects of processing on evolved microstructures, operating structural mechanisms and corresponding mechanical properties.

Physical simulation experiments were conducted on a Gleeble simulator, followed by scaling up of the experiments on a laboratory rolling mill. Detailed microstructural characterization, including the differences in fractions, morphology, C-content, and stability of RA were performed by X-ray diffraction (XRD) and electron probe microanalysis (EPMA), besides using various materials characterization and electron microscopy techniques. Mechanical properties were evaluated in respect of hardness, tensile and impact toughness properties, and structure-property correlations established.

The result showed that fine division of RA between martensitic laths, besides the refinement of martensitic packets and laths, notably improved the low-temperature impact toughness. Various combinations of high tensile strengths with good elongations could be achieved with QP and ART treatments, depending on the volume fraction, size, shape, distribution and carbon content of RA and morphology of martensite. Implementation of TMR-DQP and TMR-QP and TMR-ART processing on the laboratory rolling mill was challenging, as the properties were known to be sensitive to the processing parameters, particularly the quenching temperature (T_Q).

Keywords: advanced high strength steel, austenite reverse transformation, bainite, grain size, martensite, mechanical properties, medium-Mn steel, quenching and partitioning, retained austenite

Kantanen, Pekka, Hienojakoinen jäännösausteniitti mikrorakenteessa ja sen vaikutus 0.3 % hiiltä sisältävien uusien ultralujien teräksien mekaanisiin ominaisuuksiin.

Oulun yliopiston tutkijakoulu; Oulun yliopisto, Teknillinen tiedekunta
Acta Univ. Oul. C 872, 2023
Oulun yliopisto, PL 8000, 90014 Oulun yliopisto

Tiivistelmä

0.3C (korkea) pii- ja alumiiniseostetut sekä 0.3C keskimangaaniteräkset ovat houkuttelevia kandidaatteja uudeksi kolmannen sukupolven autoteollisuuden muovattavaksi suurlujuusteräkseksi. Tässä väitöskirjassa on tutkittu näiden teräksien mikrorakenteiden ominaisuuksia, austeniitti-martensiitti- ja martensiiti-austeniittifaasimuutosilmiöitä sekä näiden vaikutusta mekaanisiin ominaisuuksiin. Keskeytettyä sammutusta yhdistettynä matalan lämpötilan hehkutus (QP) prosessiin sekä austeniitin reversiomuutos (ART) -prosessiin on käytetty hyvien lujuus-sitkeysominaisuuksien saavuttamiseksi. Tavoite oli lisätä tietoa siitä, kuinka mikrorakenteen eri piirteet vaikuttavat termomekaanisesti valssatun suorasammutetun QP (TMR-DQP) ja termomekaanisesti valssatun ART (TMR-ART) teräksen ominaisuuksiin.

Termomekaanista Gleeble-simulaattoria ja laboratoriokuumavalssainta on käytetty mikrorakenteen ominaisuuksien ja jäännösausteniitin hajaantumisen tutkimisessa. Lisäksi käytettiin erilaisia elektronimikroskooppeja ja analysaattoreita. Mekaanisten ominaisuuksien määrittämiseen käytettiin kovuusmittareita, veto- ja iskusitkeyskokeita.

Tulokset osoittivat, että iskusitkeyteen vaikuttaa jäännösauteniitin määrän lisäksi myös rakenteen sälekoko. QP- ja ART-käsittelyillä voidaan saavuttaa erilaisia suuria vetolujuus-/venymäyhdistelmiä riippuen jäännösausteniitin määrästä, koosta, muodosta, jakaantumasta ja jäännösausteniitin hiilipitoisuudesta sekä martensiitin ja mahdollisen bainiitin morfologiasta. On haasteellista ottaa DQP-käsittely käytäntöön, koska keskeytetyn sammutuksen lämpötila vaikuttaa teräksen ominaisuuksiin ja sen hallinta tarkasti teollisessa mittakaavassa on haasteellista. ART-käsittelyssä haasteena on kapean prosessi-ikkunan (lämpötila ja hehkutusaika) hallinta ART-hehkutuslämpötiloissa.

Asiasanat: bainiitti, jäännösausteniitti, keskimangaaniteräs, martensiitti, mekaaniset ominaisuudet, raekoko

”Se olisi ollut kiva nähdä.”
Äiti

Acknowledgements

The research work for this study has been done at the Materials and Mechanical Engineering research unit of the University of Oulu during 2015–2022. The research work started under the auspices of research project *SUPERHIGH* funded by the Research Fund for Coal and Steel (RFCS), an EU funding program. The work was later continued in successive research programs, viz., Steel Ecosystem for Focused Applications (StEFA), Intelligent Steel Applications (ISA) and Fossil-free Steel Applications (FOSSA). Jenny and Antti Wihuri Foundation (2018 and 2020) and Tauno Tönning Foundation (2022) are also gratefully acknowledged for their financial support during the course of this research work. Furthermore, I express my gratitude to the SSAB Europe Oy for providing a part of the experimental materials and technical support enabling smooth progress of the research.

I express my deepest gratitude to my supervisor Professor Mahesh Somani, Professor Jukka Kömi, Professor Emeritus David Porter and Professor Emeritus Pentti Karjalainen for giving me the opportunity, unstinted support, and guidance to carry out this work for the doctoral degree. Special thanks also go to Dr. Antti Kaijalainen and Dr. Vahid Javaheri for sharing their knowledge and providing precious advice during my doctoral work. Additionally, I want to thank my doctoral committee members, Professor Jari Larkiola and Dr. Aarne Pohjonen, for their timely assessment and guidance. Many colleagues in our unit have helped me with this reseach: Dr. Oskari Haiko, Dr. Renata Latypova, Dr. Jaakko Hannula, M.Sc. Johannes Sainio, M.Sc. Sampo Uusikallio, M.Sc. Pentti Kaikkonen, M.Sc. Henri Tervo, Dr. Olli Nousiainen, Dr. Sakari Pallaspuro, M.Sc. Joonas Ilmola, M.Sc. Oskari Seppälä, M.Sc. Sami Koskenniska and M.Sc. Ilkka Miettunen. They are thanked for their support. The practical work would not have been possible without the assistance of M.Sc. Seppo Järvenpää, M.Sc. Juha Uusitalo, Mr. Ilpo Saarela, M.Sc. Tun Tun Nyo, M.Sc. Jussi Paavola. I also want to say special thanks for my industrial partners, Dr. Saara Mehtonen and Dr. Severi Anttila for supporting me in my research projects.

What would be life without friends? I owe my gratitude to all my friends outside the work sphere, too. In particular, Tuomas Hirvonen, Veli-Pekka Putila, Mikael Sorri and Heikki Tokola are acknowledged for the time we spent together from which some of the most meaningful moments of my life emerged. I would like to also thank my old colleagues from Nokia, Hannes Huotelin and Lasse Kähkönen, and their families, for the time we spent together. Additionally, my

“Taistelutoverit” and “Hossa” group of friends have been very important in bringing variation in my everyday work life.

I am extremely grateful to my parents Anni and Matti Kantanen for all their affection and support during the course of this work. I also wish to thank my sisters Liisa Kantanen and Kaisa Kantanen, Kaisa’s spouse Aslak Savolainen, and my parents-in-law, Marja-Liisa and Esko Luttinen, for their help in so many ways.

Finally, I would like to thank my wife Mari-Selina and our children Reetta, Akseli and Iisakki for their profound love, great patience, and undying support during all these years.

Oulu, 26.01 2023 Pekka Kantanen

List of abbreviations and symbols

AHSS	advanced high strength steel
ART	austenite reverse transformation
bcc	body-centered-cubic
bct	body-centered-tetragonal
BF	bright field
CPE	constrained paraequilibrium
DF	dark field
DQP	direct quenching and partitioning
EBSD	electron backscatter diffraction
EDS	energy-dispersive spectrometer
EFTEM/STEM	energy-filtered scanning transmission electron microscope
EPMA	field emission probe microanalyzer
etc.	et cetera; and so on
fcc	face-centered-cubic
FESEM	field emission scanning electron microscope
FM	fresh martensite
FRT	finish rolling temperature
i.e.	id est; that is
IPF	inverse pole figure
IQ	image quality
K-M	Koistinen-Marburger
K-S	Kurdjumov-Sachs
LOM	light optical microscope
LSCM	laser scanning confocal microscope
N-W	Nishiyama-Wasserman
PAGS	prior austenite grain size
QP	quenching and partitioning
RA	retained austenite
RT	room temperature
SAED	selected area diffraction pattern
SFE	stacking fault energy
SRX	static recrystallization
TEL	total elongation
TM	tempered martensite
TMR	thermomechanical controlled rolling

UEL	uniform elongation
UTS	ultimate tensile strength
viz.	videlicet namely
WHR	work hardening rate
XRD	X-ray diffraction
YS	yield strength

γ	*austenite*
ε	*strain*
α'	*martensite*
ε_c	*initiation of dynamic recrystallization*
ε_p	*peak strain*
a_γ	*lattice parameter*
A	*total elongation*
A_g	*uniform elongation*
A_{C1}	*lower critical temperature*
A_{C3}	*upper critical temperature*
B_s	*bainite start temperature*
d	*mean effective grain size*
d_l	*mean lath size*
$d_{90\%}$	*effective grain size at 90% in the cumulative size distribution*
d_{gauge}	*gauge diameter*
L_0	*gauge length*
L_C	*length of reduced section*
M_f	*martensite finish temperature*
M_s	*martensite start temperature*
n	*work hardening exponent*
t_{50}	*the time for 50% recrystallization*
T_{NR}	*no-recrystallization temperature*
T_P	*partitioning temperature*
t_P	*partitioning time*
T_Q	*quenching temperature*
T_R	*austenite reverse transformation temperature*
t_R	*austenite reverse transformation time*
V_A	*volume fraction of austenite*
$V_{Mdilatation}$	*initial transformed martensite fraction*
V_M	*volume fractions of martensite*
$\dot{\varepsilon}$	*strain rate*

List of original publications

This thesis has been compiled based on the following publications, which are referred throughout the text with respective Roman numerals I–VI:

I Kantanen, P. K., Javaheri, V., Somani, M. C., Porter, D. A., & Kömi, J. I. (2021). Effect of deformation and grain size on austenite decomposition during quenching and partitioning of (high) silicon-aluminum steels. *Materials Characterization, 171,* 110793. https://doi.org/10.1016/j.matchar.2020.110793

II Somani, M. C., Porter, D. A., Karjalainen, L. P., Kantanen, P. K., Kömi, J. I, & Misra D. K. (2019). Static recrystallization characteristics and kinetics of high-silicon steels for direct quenching and partitioning. *International Journal of Materials Research, 110 (2019) 3,* 183–193. https://doi.org/10.3139/146.111744

III Kantanen, P. K., Somani M. C., Porter D. A., Kömi, J. I., & Misra, D. K. (2018). Microstructures and mechanical properties of tough ductile ultrahigh-strength steels processed through direct quenching and partitioning. *Materials Science Forum*, *941,* 468–473. https://doi.org/10.4028/www.scientific.net/MSF.941.468

IV Kantanen, P., Somani, M., Kaijalainen, A., Haiko, O., Porter, D., & Kömi, J. (2019). Microstructural characterization and mechanical properties of direct quenched and partitioned high-aluminum and high-silicon steels. *Metals*, *9*(2), 256. https://doi.org/10.3390/met9020256

V Haiko, O., Somani, M., Porter, D., Kantanen, P., Kömi, J., Ojala, N., & Heino, V. (2018). Comparison of impact-abrasive wear characteristics and performance of direct quenched (DQ) and direct quenched and partitioned (DQ&P) steels. *Wear*, *400–401*, 21–30. https://doi.org/10.1016/j.wear.2017.12.016

VI Kantanen, P., Anttila, S., Karjalainen, P., Latypova, R., Somani, M., Kaijalainen, A., & Kömi, J. (2022). Microstructures and mechanical properties of three medium-Mn steels processed via quenching and partitioning as well as austenite reversion heat treatments. *Materials Science & Engineering: A*, 847, (2022), 143341. https://doi.org/10.1016/j.msea.2022.143341

In Publications I, III, IV and VI, Pekka Kantanen has been the main corresponding author and in Publications II and V, a co-author with Professor Mahesh Somani and Dr. Oskari Haiko. In all these papers, the conceptualization, planning, detailed experiments including microstructural examination and mechanical property evaluation, analyses of the results, structure-property correlations and writing of the articles were done by the main author.

As a co-author, Pekka Kantanen has participated in planning of the steels, conducting the experiments and analysis and heat treatments for Publication II.

As a co-author, Pekka Kantanen has carried out the laboratory hot-rolling simulations, all the necessary heat treatments for the experimental steels,

preliminary microstructural analysis, and the subsequent evaluation of the mechanical properties, as required for Publication V. Pekka Kantanen has also assisted in carrying out the wear tests and holding scientific discussion regarding the role of retained austenite on the mechanical properties as well as wear resistance of the martensitic steels. Besides, the electron backscatter diffraction (EBSD) and X-ray diffraction (XRD) measurements were conducted by Pekka Kantanen for the characterization of requisite microstructures and clarification of the role of retained austenite on the mechanical properties and wear behavior, respectively, as reported in Publication V.

The supervisors throughout the research work were Professor Mahesh Somani (Publications I, II, III, IV, and VI), Professor Jukka Kömi (Publications I, III, IV, and VI), Professor Emeritus David Porter (Publication I, III and IV), Dr. Antti Kaijalainen (IV and VI) and Professor Emeritus Pentti Karjalainen (Publication VI). All the supervisors are acknowledged for their valuable comments and help in writing the publications.

In Publication I, Dr. Vahid Javaheri has done work related to the austenite grain reconstruction based on an assumed Kurdjumov-Sachs (K-S) orientation relationship between the austenite and transformed martensite and/or bainite. Dr. Javaheri is also acknowledged for his valuable comments and help in writing the publications.

The transmission electron microscopy (TEM) investigations included in Publication III were performed at the University of Texas at El Paso, USA under the supervision of Professor Devesh Misra, and he is acknowledged for the valuable guidance and scientific discussions.

In Publication IV, Dr. Oskari Haiko has helped with the scanning electron microscopy (SEM) and is acknowledged for his valuable comments and help in writing the publications.

Thermo-Calc calculations in Publication VI were performed with the help of Dr. Severi Anttila, SSAB Europe Oy, Raahe, Finland. Dr. Anttila is also acknowledged for his valuable comments and help in writing this publication. In Publication VI, Dr. Renata Latypova has carried out the work related to the austenite grain reconstruction and is hereby gratefully acknowledged for her contribution.

Contents

1 Introduction

The ever-increasing demand for new lighter and safer structures, such as those required in the automotive and transportation sectors, has been a subject of keen interest for decades. As regards the economic efficiency, the focus has continuously been on the light-weighting of the structures by developing advanced high strength steel (AHSS) grades to reduce the energy consumption as well as carbon footprint. On the other hand, achieving satisfactory strength-ductility balance continues to be of main importance for manufacturing critical vehicle components that need to have excellent crash-resistance in order to withstand any instance of collision, besides imparting adequate rigidity to the cabin to protect the passengers. Hitherto, the growing complexity of safety design with the necessity to ensure expected stiffness with smaller wall thicknesses required special combinations of strength and formability properties. Those requirements were included in the term AHSS [1]. In recent years, intensive research has been directed to develop the new, third generation AHSSs aimed at providing an even higher strength-ductility balance with improved strain hardening capacity and low temperature toughness compared to the conventional AHSS grades. A combination of formability and strength expected from the third generation AHSS assumes strength criterion based not only on the tensile strength, but the yield strength (YS) as well. Presently, the QP-processed Si and/or Al alloyed medium carbon steels and ART-processed medium-Mn steels (3–10% Mn) are being considered as some of the most promising third-generation AHSSs. Both approaches utilize a requisite fraction of metastable austenite in the microstructure to ensure enhanced ductility, whereas the high strength is imparted by low temperature transformation products such as martensite.

1.1 Background

In the first decade of the 2000s, an innovative development of AHSS already started with the aim to foster their role in making vehicles lighter, while securing their safety features. The third generation AHSSs include carbide-free bainitic steels, medium-Mn steels and QP steels, of which the latter two are included in this study. Even though the initial research investigations on medium-Mn steels started as early as 70s, a more intensive study, however, began only in early 2000s under the auspices of the development of third generation AHSSs. First, the QP treatment was proposed in 2003, which showed immense promise with an all-round improvement

in mechanical properties, and a few years later, renewed research efforts were directed at the medium-Mn steels because of their potential to become a part of third generation steels [2]. For medium-Mn steels, various microstructures can be generated using different heat treatments, and accordingly, steels with a broad range of strength-ductility combinations can be produced.

As schematically presented in Fig. 1a, in QP processing, the steel is austenitized (or subjected to intercritical annealing in some cases) and quenched to a temperature between martensite start (M_s) and finish (M_f) temperatures, followed by holding at quench stop temperature or higher (generally, in M_s–M_f temperature range) for a suitable time to facilitate the partitioning of carbon from supersaturated martensite to austenite, which can thereby be partly or fully stabilized down at room temperature (RT). Unlike in the case of quenching and tempering, the decomposition of austenite and the precipitation of carbides are deliberately suppressed by alloying with elements like Al and Si. Not only the volume fraction of RA, but also its stability in respect of shape, size, distribution, morphology (preferably, finely divided interlath film-like) and carbon content, is important for optimized property combinations. There are many factors that affect the stability of RA, such as the austenitization temperature, deformation history, quenching rate, T_Q temperature, partitioning temperature (T_P) and time (t_P), austenite defect structure, size, and type (block- or film-like), crystallographic orientation, constraining effect of the neighboring phase and the casting morphology [3]–[6] Not only the amount of RA and its stability, strength-ductility balance is related also to the formation of bainite, isothermal martensite and fresh martensite (FM) as well as tempering of martensite. In addition to QP process, the present study also includes implementation of the TMR-DQP process, which essentially comprises thermomechanical rolling followed by direct quenching and partitioning [7]. The partitioning treatment in a furnace can be either for a specified duration, or alternatively, the rolled samples are cooled slowly over several hours along with the furnace in order to simulate the cooling of the coiled strips in actual industrial practice. The specific aim here was to establish the TMR-DQP processing route for the studied steels to achieve excellent property combinations.

ART treatment is an established heat treatment, whereby austenite is stabilized down to room temperature by means of the austenite reversion from fully martensitic or cold rolled partially transformed martensitic microstructure, subjected to intercritical annealing [8]. In the ART treatment, the partitioning is not just limited to interstitials, but substitutional elements like Mn too participate in stabilizing the austenite [9]. During the intercritical annealing process, the austenite

stabilizing elements such as C and Mn tend to partition from martensite into austenite, which helps stabilize a significant fraction of intercritical austenite at RT. ART treatment is generally applied to both hot and cold rolled medium-Mn steels, but in this study, the focus was only on hot rolled samples. As mentioned in the case of QP processing, factors such as shape, size, distribution, morphology, and enrichment with austenite stabilizing elements, i.e., C and Mn, affect the stability of RA in ART-processed steels. Intercritical annealing is performed at a suitable temperature between lower and upper critical temperatures (A_{C1} and A_{C3}, respectively) during reverse transformation from ferrite (or martensite) to austenite. After quenching to RT, the microstructural features may comprise of tempered martensite (TM), FM, ferrite and RA depending on the specified austenite reverse transformation temperature (T_R) and austenite reverse transformation times (t_R). ART process is schematically depicted in Fig. 1b.

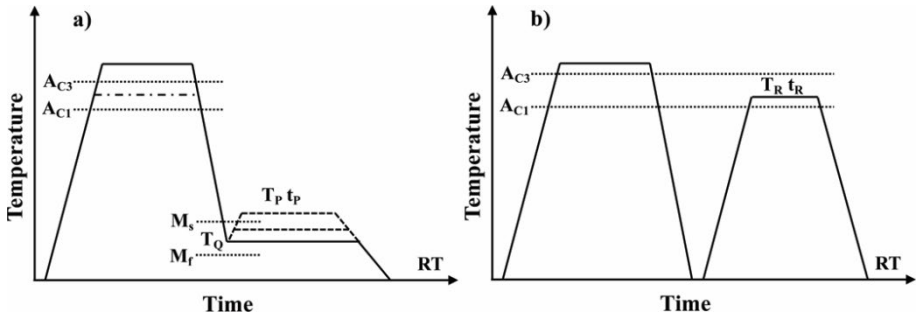

Fig. 1. Schematic sketches of a) QP and b) ART processing schedules.

Even though numerous studies are available in literature regarding the QP- and ART-processed steels with significantly improved properties, there still is a lot of scope to improve the strength-ductility combinations in these alloys. For instance, there are various possibilities for both the alloy and process designs to impart a set of desired properties. On the other hand, there are challenges of accomplishing various process targets. For example, in the case of QP processing, quenching at the exact T_Q temperature is very challenging and difficult to control on industrial scale. Similarly, in the case of ART treatment, the process windows for intercritical annealing are often very narrow and difficult to achieve and control. These possibilities and challenges, therefore, call for conducting future studies in order to solve the practical challenges and difficulties, while implementing the optimized thermomechanical processing parameters, determined through laboratory-scale

simulations with extensive characterization and evaluation in respect of microstructures, mechanisms and properties. The ultimate aim, however, would be to establish feasible processing routes based on parametric optimization for a set of chemistries. This work is related to the futuristic goals targeting the development of tough, high/ultrahigh strength steels via QP/DQP and ART processing.

1.2 Aim and objective of the study

The scope of this thesis is to develop novel QP/DQP- and ART-processed steels with improved strength-ductility properties via Gleeble thermomechanical simulations and laboratory hot rolling. This thesis also compiles the information regarding the microstructure and mechanical properties of futuristic steels that are amenable for industrial processing. In these steels, the presence of finely divided RA plays a very important role in imparting the desired strength-ductility combinations with high/ultrahigh strength and excellent toughness. Besides, the morphology of martensite and other possible phases too have a significant effect on the mechanical properties. The research aims are the following:

1. To clarify the occurrence of austenite decomposition and other mechanisms operating during partitioning treatment and subsequent cooling to RT in the case of 0.3C, (high) Si-Al QP steels.
2. To study the effect of prior deformation and grain refinement on the subsequent QP behavior of 0.3C, (high) Si-Al QP steels.
3. To characterize the microstructures of 0.3C, high-Si and high-Al steels processed via novel TMR-DQP process based on optimized QP parameters.
4. To evaluate the mechanical properties of 0.3C, high-Si and high-Al steels processed via novel TMR-DQP process and to reach YS ≥ 1200 MPa, ultimate tensile strength (UTS) 1700–1900 MPa and T28J (transition temperature for impact energy of 28 J) ≤ –60 °C.
5. To comprehend and elucidate the mechanisms operating during QP/DQP and ART processes.
6. To determine the appropriate hot rolling and subsequent QP as well as ART processing parameters to reach the UTS level of 1500 MPa, at least 20% total elongation (TEL) and with > 10% RA in the microstructures of the 0.3C, medium-Mn steels.
7. To examine the microstructural differences following relatively short periods of QP (1000 s) and ART (100–5000 s) processing in 0.3C, medium-Mn steels.

The study on research aims 1 and 2 are reported in Publication I. This work focused on the effect of steel composition and prior controlled deformation on the subsequent decomposition of austenite during partitioning treatment. The test was conducted using the Gleeble simulator and was intended at optimizing the QP parameters for subsequent laboratory hot rolling simulations (TMR-DQP). In Publication II, the static recrystallization characteristics and kinetics of QP steels were elucidated for high-Si steels and, hence, are connected with the study in Publication I. The data are useful in planning the thermomechanical rolling schedule prior to DQP processing.

Research aims 3 and 4 are reported in Publications III, IV and V. The work focused on the microstructures and mechanical properties of the TMR-DQP-processed steels. The effect of RA on the wear resistance of TMR-DQP steels was clearly elucidated in Publication V. In these studies, TMR-DQP processing of the steels was carried out using a laboratory hot rolling mill, suggesting its amenability for industrial processing.

Research aims 5–7 were pursued in Publication VI. This work encompasses the details of the processing routes and their influence on the evolving microstructures as well as the morphology, amount and stability of RA based on Gleeble simulations for QP- and ART-treated steels. Limited tensile property data obtained on the laboratory rolled plates were included in these studies to understand the efficacy of the two processing routes in accord with the target UTS level selected with requisite ductility.

A long-term objective of this research study is to develop QP and ART processing routes based on novel steel concepts with superior strength-ductility combinations and good toughness for structural applications, such as in automotive and transportation sectors.

2 Theoretical background

Microstructure is the key to the mechanical and other properties of steels, which in turn depend on the alloy design, heat treatment and deformation history. This chapter on theoretical background focuses on the three main phases formed in the examined steels, besides the QP and ART treatments as well as various microstructural mechanisms operating during these processes from the perspective of mechanical properties.

2.1 Austenite

Austenite has a face-centered-cubic (fcc) crystal structure, and it is a simple solid solution in which the interstitial carbon atoms are randomly arranged. In a fcc unit cell, lattice parameter is longer than that in bcc, but the packing density of unit cell is tighter because of the larger number of atoms per unit cell. The maximum radius ratio of an assumed hard, spherical atom that can be fitted into a body-centered-cubic (bcc) lattice is ~0.29, whereas in fcc lattice, without distorting it is considerably bigger at ~0.41. For carbon and iron, the radius ratio is actually ~0.60, which means that significant distortion of the iron lattice occurs, when it contains carbon. Carbon in bcc affects severe tetragonal distortion, which is mainly the cause of the hardening effect. Further, the solubility of carbon is also expected to be much more in fcc than in bcc [10].

The high temperature form of austenite can be retained at lower temperatures when suitably added with alloying elements, and carbon especially is very effective in lowering the M_S temperature. In QP process, metastable RA is enriched with interstitial carbon atoms by partitioning from martensite to austenite in order to be able to stabilize it down to room temperature. In the ART process, only at relatively high temperatures in the intercritical range, the diffusion of substitutional atoms, such as Mn, becomes possible from martensite (ferrite) to austenite [11].

2.2 Martensite

Generally, martensitic transformations are concerned with the formation of martensite during the cooling of steels, whereby the high-temperature phase austenite under certain conditions transforms into bcc or body-centered-tetragonal (bct) martensite depending on its carbon content [12]. Martensite has been originally considered to describe the hard microconstituent that achieves the

highest hardness and strength among carbon steels [13]. Many factors influence the strength of martensite phase in steels. Martensitic microstructures are complex, often containing RA and several possible levels of carbide distributions, in addition to hard martensite crystals of different morphologies. It is difficult to outline a broad definition of martensite, but the following features are associated with martensitic transformations. During transformation, chemical composition does not change and the orientation relationship between the parent and product lattices remain. The martensite forms thin laths or plates that do not cross the parent austenite grain boundaries. Martensitic transformation is a diffusionless, solid state transformation, during which a shear-dominant lattice distortion accompanies the cooperative movement of all the atoms. Furthermore, martensitic transformations involve the coordinated movement of atoms within an interatomic distance such that the neighboring atoms in parent phase remain as neighbors in the martensite (military transformation) [6], [12]. The growth rate of the martensitic phase transformation proceeds by the migration of relatively sharp interfaces at the speed of sound. The growth rate does not significantly depend on temperature and thermal activation usually involved in the growth process. Martensite nucleates heterogeneously and it can form athermally or isothermally.

Lath martensite, a typical structure of low and medium carbon martensitic steels, is one of the most important constituent phases in high- and ultra-high-strength steels. Lath martensite displays a hierarchical microstructure in steel comprising essentially of packets, blocks, and laths, as shown in Fig. 2. The prior austenite grains transformed to martensite comprise of a number of packets which in turn consist of blocks. These blocks having the same habit plane in a packet contain sub-blocks corresponding to a single variant of K-S orientation relationship with austenite. High-angle grain boundaries delineate the packet and block boundaries, whereas low-angle grain boundaries separate the sub-blocks and laths from each other [14], [15]. Even sub-block boundaries are low angle boundaries and they can act as barriers to the gliding of dislocations and increase the strength of the lath martensite [15]. An austenite grain is divided into several packets, which are composed of laths with the same habit plane. The martensite laths generally have a K-S orientation relationship with the parent austenite: $\{111\}_{\gamma} \| \{011\}_{\alpha'}$, $<110>_{\gamma} \| <111>_{\alpha'}$ [16], [17]. There are other types of martensitic ferrite and austenite relationships also and the most notable among them are the Bain and Nishiyama-Wasserman (N-W) orientation relationships [18].

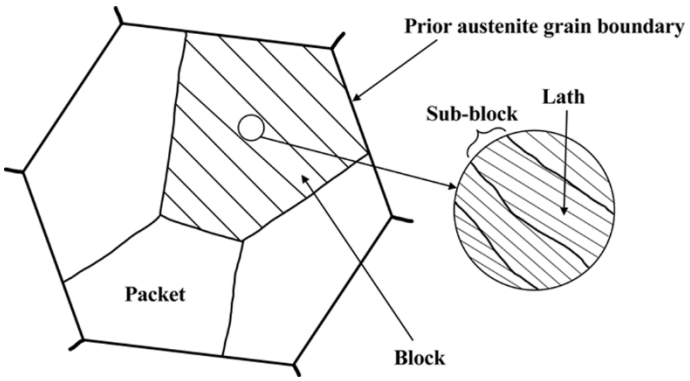

Fig. 2. Schematic illustration of multi-scale structure of lath martensite.

2.3 Bainite

Bainite has a bcc crystal structure and with the carbon-rich volumes, and it would probably assume a bct crystal structure [12]. In this chapter, the focus is on lower bainite because upper bainite formation was not observed under the conditions of processing in this work. Bainite forms at a temperature above the M_s temperature but below the temperature regime, where pearlite is formed. Bainite can also form at temperatures below M_s under specific conditions [19], [20]. During austenite to bainite transformation, the sub-units of bainite first nucleate at austenite grain boundaries and as bainite formation continues, bainite sub-units nucleate at bainitic ferrite/austenite interfaces as well. Bainite formation is accompanied by carbon partitioning into the ambient austenite matrix. If the austenite carbon concentration exceeds the solubility limit, cementite precipitates. Depending on the composition of alloy and the bainite formation temperature, the nature of cementite precipitation varies resulting in upper bainite or lower bainite [21]. Both upper and lower bainite are composed of aggregates of plates of ferrite, separated by cementite, RA or martensite [22]. Cementite precipitates in between the bainitic ferrite sub-unit in upper bainite, and within the sub-units as well as between them in lower bainite. Cementite layers are normally coarser in upper bainite than in lower bainite and the temperatures of upper and lower bainite formation are in the range of 550 to 400 °C and 400 to 250 °C, respectively [21].

Lower bainite as well as athermal martensite are formed in a displacive manner, which results in a high dislocation density both in the parent austenite as well as the product phase [23]. Both cementite and ferrite in bainite have an orientation

relationship with the austenite grain in which they grow [12]. In this thesis, QP or ART treatments have been carried out following cooling from the austenitization temperature using a linear cooling rate fast enough to prevent bainite formation before reaching the M_s temperature. It is to be noted that isothermal bainite can form under M_s temperatures as well, though the kinetics will depend on the stability (composition) of the austenite. In QP process of medium-C steels, bainite formation occurred during partitioning in the temperature range 200–400 °C, for 1000 s, but the possibility of bainite transformation in medium-Mn steels was evidently mitigated during the partitioning under similar conditions (200–400 °C; 1000 s), because of higher Si and Mn contents [24], [25]. It has been confirmed that the bainite transformation kinetics of Fe-C-Si-Mn alloys are much slower than those of Fe-C-Mn and Fe-C-Si alloys, even though the concentrations of Si and Mn in these alloys are approximately the same, i.e., the interaction of Si and Mn retard bainite formation [26]. Calculations based on JMatPro software further corroborated the retarding effect of Si and Mn (and also Ni) on bainite transformation [25]. Alloying additions, such as Mn, Cr and Mo retard bainitic reaction and can be intentionally added in higher amounts, together with approximately 1% Ni, to enable carbon partitioning from martensite to austenite, while preventing the occurrence of other competing reactions [2], [27]. Increasing carbon content does decrease bainite start temperature (B_s) [28]. On the other hand, both Cr and Mn delay bainite transformation but result in slightly higher fractions of bainite. In comparison, Mn does increase incubation time of bainite transformation and decreases B_s temperature [2], [29]. Besides, Mo significantly delays the decomposition of austenite in the upper temperature range and extends the range of cooling rates for bainite transformation [2].

Interestingly, bainitic steels too in the past have displayed a behavior similar to that seen in martensitic QP steels. For example, some bainitic steels with specific composition designs have displayed isothermally transformed nanostructured bainite plates interspersed with finely divided C-enriched RA (20–40 nm thick), thus imparting exceptionally high strengths and toughness in bainitic steels with reasonably ductility [30], [31].

2.4 Quenching and partitioning

In the QP processing, the steel is fully austenitized or in some cases, intercritically annealed between A_{C1}–A_{C3} temperature (leading to mixtures of austenite and ferrite), quenched to a temperature between M_s and M_f temperatures, followed by holding

at the quenching stop temperature or at slightly higher temperature for a suitable time to allow the partitioning of carbon from supersaturated martensite to untransformed austenite, which can thereby be completely or partly stabilized at RT as finely divided interlath films, or pools where laths have not formed. If enough carbon cannot partition to austenite, or if there are carbon concentration gradients in the austenite, some of the austenite with lower stability or inadequate carbon enrichment may transform to FM upon cooling to RT. When QP process is combined with direct quenching after thermomechanical rolling comprising recrystallization controlled rolling followed by controlled rolling in no-recrystallization (T_{NR}) regime, the process is termed as TMR-DQP treatment or just DQP [32].

Unlike in the case of conventional quenching and tempering, the precipitation of iron carbides and the decomposition of austenite are intentionally suppressed in QP processing by alloying with Si, Al, or P, of which Si is the most commonly used alloying element in QP steels [33]–[38]. The advantageous effects of P in hindering carbide formation are found only in the presence of Si and Al [6]. Si increases the chemical potential of carbon in ferrite, raises the ferrite formation temperature and being a strong graphitizer, it promotes carbon partitioning into the austenite by preventing carbide formation [6]. The effect of Si in the retardation of cementite precipitation in austenite is explained by the fact that when cementite forms under the paraequilibrium conditions, it traps the silicon as it grows, which results in decreasing the free energy of the reaction and results in slowing down the kinetics of precipitation [39]. In ferrite, Si is effective in preventing cementite precipitation only when its carbon content is very low. Comparing steels containing Al or Si alloying, it is suggested that Al might be less effective than Si in retarding the formation of transition carbides [40]. Although Al does enlarge the two-phase (A_{C1}–A_{C3}) range and facilitates carbon partitioning into austenite, it also has the possible adverse effect of indirectly decreasing the RA stability by increasing the M_s temperature. In addition, Si provides a higher level of solid solution strengthening in comparison to Al [6]. Cr is known to stabilize ferrite at high Cr content but when added in small amounts, Cr can act as an austenite stabilizer along with Si due to the synergetic effect of Si and Cr additions in increasing RA fraction during QP processing [41]. Mn is a strong austenite stabilizer and hence, reduces the M_s temperature, the ferrite growth kinetics, and the activity of C in austenite. In a C-Si-Mn steels, Si enhances Mn segregation to austenite grain boundaries (500 °C, <30 min) and hinders the carbides precipitation, thereby increasing the C content of the untransformed austenite during partitioning and decreasing the nucleation

rate of bainitic ferrite [6], [42]. Cr, Mo, Nb and Ni also suppress the formation of bainite and isothermal martensite during partitioning [34], [43]–[47].

Under the constrained paraequilibrium (CPE) conditions, most of the carbon partitions from martensite into austenite. The three main conditions for CPE are: i) a stationary martensite-austenite interface, ii) preclusion of carbide precipitation and iii) an identical chemical potential for carbon in ferrite (i.e., carbon depleted martensite) and austenite [48], [49] The assumption that martensite - austenite phase boundaries are stationary during QP processing is due to the fact that T_P is relatively low (normally ≤450 °C), suggesting that the diffusivities of the substitutional alloying elements are too low to partition [49]. Nevertheless, it has been shown that during QP treatment, partitioning of Mn and Si might occur near the martensite - austenite boundaries, within the characteristic thickness range of RA with a lath morphology [49]. The isothermal growth of the existing martensite during partitioning results in wavy, irregular interfaces between austenite and martensite due to the formation and migration of ledges that allow the martensitic laths to grow into the austenite isothermally and this has been linked to the relaxation in austenite as carbon partitioning progresses [50].

Besides carbon partitioning from martensite to austenite, a host of other microstructural mechanisms may also take place during the partitioning process, such as formation of transition carbide (ε-carbide) and cementite, decomposition of austenite into bainite and the ledged growth of isothermal martensite [33], [50]. With the increase in T_Q and T_P temperatures and t_P time, the volume fraction of RA increases until it reaches a maximum value and then starts to decrease again [25], [33], [40]. The carbon enrichment of austenite, on the other hand, increases with the increase in T_P, until carbide precipitation starts, generally at high temperatures (≥450 °C). For a given set of processing parameters, the above-mentioned mechanisms that compete with the carbon partitioning from martensite to austenite, as well as the presence of different alloying elements in the steel render the prediction of stabilized volume fraction of RA and its carbon content far more complicated. Even lowering the finish rolling temperature (FRT) close to A_{C3} temperature is shown to raise the volume fraction of RA [51].

2.5 Austenite reverse transformation

The ART process is a heat treatment, by which a suitable fraction of austenite is stabilized down to room temperature by means of austenite reversion from full or partial martensitic microstructure, followed by intercritical annealing for a suitable

duration, thus enabling austenite stabilizing elements such as C and Mn to partition from martensite into austenite. ART treatment is generally applied to hot or cold rolled medium-Mn steels (3–10% Mn). To obtain the austenite phase, intercritical annealing is performed between A_{C1} and A_{C3} temperatures enabling reverse transformation of a fraction of martensite (or ferrite) to austenite. As stated earlier, in addition to the interstitials, even the substitutional elements, like Mn, participate in stabilizing the austenite [9]. Mn has an essential role to play in the ART process, thereby enabling the accomplishment of desired mechanical properties, particularly the high combination of strength and ductility. A decrease in Mn content leads not only to a decreased stacking fault energy (SFE), but also the RA volume fraction, thereby weakening the TRIP effect and lowering the strength-ductility combination [52]. In general, increasing the carbon content in a steel will decrease the A_{C3} temperature and hence narrow down the A_{C1}–A_{C3} range [53]. However, an addition of aluminum does increase the A_{C1} and A_{C3} temperatures, but the effect on A_{C1} temperature is insignificant, at least with low Al alloying content (≤1%), and hence, a suitable addition of Al favorably broadens the intercritical annealing window. On the other hand, the single-austenite-phase region will disappear with the addition of 3% Al [54]. In contrast, Si does not only promote enhanced stability of reverted austenite, but also increases the hardenability of the steel and results in high strain hardening rate of ferrite by suppressing the cross-slip [55].

Intercritical annealing of a hot rolled steel (Fe-0.05C-9Mn, T_R 620 °C and t_R 600 s) resulted in a microstructure comprising of lath-shaped ferrite with a high density of dislocations due to low recovery, and RA (~30%) with a low dislocation density and high Mn (11.7%) and C (0.12%) concentration [56]. On the other hand, intercritical annealing of a cold rolled steel led to the formation of an equiaxed ferrite with a low dislocation density due to active recovery, and RA (~37%) with a low dislocation density and high Mn (12.2%) and C (0.19%) concentration. Higher RA fraction of cold rolled specimen indicates that cold rolling accelerated the reverse transformation from martensite to austenite [56].

With the increase in the intercritical annealing temperature, i.e., T_R, the volume fraction of RA also increases, until it reaches a maximum value and then starts to decrease again [57]. This is related to the annealing conditions of reversion transformation from martensite to austenite, partitioning of alloying elements and grain growth during the intercritical annealing [55]. The Mn content of austenite decreases with the increase in T_R because at high temperatures both the chemical stability as well as the grain growth of reverted austenite deteriorate, leading to the low stability of austenite [58], [59]. In contrast, austenite grain refinement lowers

the M_s temperature, especially at small grain size <20 μm, and improves the mechanical stability of reverted austenite [55], [60].

In view of the above facts, in the ART process, intercritical annealing at low T_R (close to A_{C1}) improves the stability of reverted austenite, though its volume fraction would be low and, hence, the fraction of RA will remain low. On the other hand, a high T_R (close to A_{C3}) for intercritical annealing does lead to a high-volume fraction of reverted austenite, but with low stability, and most of this austenite transforms back to fresh martensite during final cooling to RT, resulting in a low fraction of RA at room temperature. Hence, to get an appropriate mix of RA and martensite (or ferrite) volume fractions in the final microstructure, T_R should be chosen appropriately, somewhere in the middle of A_{C1}–A_{C3} temperature range. Table 1 presents the relative effect of T_R on the resultant microstructures of ART-processed samples, both during the intercritical annealing as well as subsequent cooling to RT.

Table 1. Effect of T_R on austenite fraction, grain size, Mn content of austenite, stability of austenite and fresh martensite fraction during ART annealing and subsequent cooling to RT.

Microstructure	During ART annealing			at RT		
	High T_R	Med T_R	Low T_R	High T_R	Med T_R	Low T_R
Austenite%	high	medium	low	low[1]	high[1]	low[1]
Grain size	large	medium	small	large	medium	small
Mn% of austenite	low	medium	high	low	medium	high
Stability of austenite	low	medium	high	low	medium	high
Fresh martensite%	N/A	N/A	N/A	high	-	-

[1]Retained austenite fraction

The effects of the annealing time on the evolved microstructures of medium Mn steels are similar to the effects of T_R [9], [11], [59], [61], [62]. At a given T_R, the volume fraction of reverted austenite increases with the increase in annealing time (t_R), reaches a peak and then starts decreasing on further holding [59]. When the t_R increases, the volume fraction of reverted austenite increases too, until it reaches a saturated equilibrium fraction. C and Mn concentrations of reverted austenite will also increase during this time and reach a saturated equilibrium concentration. Besides, the grain size of reverted austenite will also grow with increasing t_R [11], [59]. Long t_R, therefore, allows the formation of a large fraction of reverted austenite resulting in a significant formation of FM during final cooling.

The heating rate too affects the reverse transformation mechanism. At a slow heating rate to the ART temperature, reverse transformation from martensite to austenite can proceed diffusively and cementite can precipitate along various martensite boundaries, including the lath boundaries, where the austenite grains start to form close to these cementite particles. This can lead to the formation of globular-shaped austenite with a low density of dislocations, and corresponding A_{C1} and A_{C3} temperatures can decrease, too [63]. At a fast heating rate to the ART temperature, the reverse transformation can occur without diffusion and the precipitation of cementite, thereby leading to the formation of lath-like austenite with a high, inherited dislocation density. At least in the beginning of reversion transformation, globular austenite has a higher stability compared to the lath-shaped austenite. This is most probably due to the finer grain size and higher Mn concentration in austenite [63]. Low cooling rates, e.g., furnace cooling, decrease the RA fractions due to the precipitation of cementite along the austenite boundaries [55].

2.6 Mechanical properties

2.6.1 QP processing

Not only the volume fraction of RA, but also its stability in respect of shape, size, distribution, type (preferably, finely divided interlath film-like), carbon content etc. are important in the design of the QP treatments to achieve desired mechanical properties. There are a lot of factors that affect the stability of RA, such as the interdendritic segregation morphology after casting, austenitization temperature, deformation history, quenching rate, quenching and partitioning temperatures, partitioning time, size and shape (block- or film-like) of austenite, austenite defect structure, crystallographic orientation and constraining effect of the neighboring phase [3]–[6]. A fully austenitized QP-processed microstructure mainly comprises of carbon depleted primary martensite and carbon enriched RA. At a relatively low T_Q temperature, a high YS and UTS can be obtained along with reasonable ductility. The RA stability can be high due to the possibility of enrichment with a high carbon content (low untransformed austenite fraction), besides a fine grain size of RA (often lath-like films). During straining, a high stability of the austenite results in slow transformation kinetics for a given strain. In one study, when T_Q exceeded a certain characteristic temperature, the microstructure also consisted of untempered,

high carbon FM, which resulted in a high initial work hardening rate (WHR) and high UTS during subsequent straining, but the plastic instability (necking) occurred at a relatively low strain level [64]. This indicated that the presence of FM contributed to a reduction of tensile ductility. In our research study, only small fractions of FM were noticed in exclusive cases of medium-Mn steels during final quenching to RT (mostly evident at low T_P of 200 °C) [25].

The overall mechanical properties of QP-treated steels are dependent on the volume fractions and compositions of the phases present. Tempered martensite has a relatively high YS, and it constitutes for the highest volume fraction of the constituent phases and consequently, it has the greatest effect on the YS of the QP steels [65]. The dislocation density of tempered martensite is inversely proportional to the T_Q, i.e., the YS and volume fraction of tempered martensite decrease with increasing T_Q [66]. The RA transforms to strain induced martensite during straining. Deformation induced twins in tensile specimens, which possibly could be beneficial in terms of providing plasticity, can also be observed in the strained RA of QP-treated steel [64]. While RA exhibits a high WHR over a strain range mostly due to the TRIP effect, the WHR of the tempered martensite reaches a high saturation value at small strains because of the fast dislocation density saturation. The FM with a large solid solution strengthening from carbon enrichment and a high dislocation density acts as a brittle phase [64].

2.6.2 ART processing

Both the QP and ART treatments utilize a requisite fraction of metastable austenite for enhancing ductility, whereas high strength is provided by the matrix phase comprising essentially of martensite and, in some cases, with a fraction of bainite. As in the case of the QP processing, similar factors affect the stability of RA in ART-processed steels, as mentioned in the previous chapter. Medium-Mn steels have been commonly processed through the ART route, and Mn has invariably played an important role in accomplishing the desired martensite(-bainite)-austenite structure that can impart the high strength-ductility balance. Increasing the Mn content does enhance the hardenability, austenite stabilization, microstructural refinement, and solid-solution hardening [67]. Si enhances Mn segregation to austenite grain boundaries, which retard the carbide precipitation. This increases the carbon content of untransformed austenite through partitioning and retards the nucleation rate of bainitic ferrite. Mn is also known to be a strong solid solution strengthener [6]. During long annealing at T_R, C and Mn have been

found to have significantly enriched the austenite. Furthermore, long annealing times lower the dislocation density due to tempering and result in low WHR [68].

Microalloying elements, such as Mo, Nb, Ti and V, are also strong carbide formers and are typically used for ferrite grain refinement, strengthening, and increasing the hardenability of steels. These alloying elements reduce the M_s temperature when present in solid solution in the austenite, in addition to promoting the solid solution strengthening, but these elements also decrease C from the solid solution if they form carbides and carbonitrides [6], [69], [70].

The size of the RA has a direct influence on the mechanical properties. Coarse RA can be unstable and transform to martensite at low strains. A decrease in the size of the dispersed residual austenite films/grains can significantly decrease the M_s temperature, when the grain size is as small as 0.1 μm. If the effect of chemical stability is disregarded, the RA grain size itself inhibits the number of available nucleation sites for martensite that is proportional to the surface area, retards the plastic accommodation accompanying the martensite formation and martensite lath propagation, increases elastic strain energy required for martensite lath formation and controls the martensite interfacial energy. The influence of the retained austenite grain size can be a significant factor in decreasing the M_s temperature with respect to the TRIP steels [6], [71], [72]. During deformation-induced transformation, two factors control the plastic flow behavior of the steels: the dynamic softening, which is dominant at low strains, arising from plastic straining due to the dilatation effect upon formation of martensite grains, and the static hardening caused by increasing the harder martensitic volume fraction [6].

Not only the stability and fraction of RA, but also the neighboring phases affect the strength-ductility balance. Due to the presence of hard martensite, external stresses directly propagate to RA due to strain partitioning and most of the RA may easily transform to martensite in the early stage of straining [51]. Furthermore, RA orientation and stress-state affect the RA stability. The plasticity of the steel is increased by deformation under high hydrostatic pressure, as this results in a low ratio of normal to shear stresses. RA is more stable under compressive loading than in tension. Pure shear, as in torsion, results in lowest austenite stability [73].

3 Materials and methods

In this chapter, the studied materials, the employed research methods, and the laboratory hot rolling schedules are described. In addition, an account of various characterization techniques employed for the interpretation of microstructural features as well as the testing methods used for the evaluation of mechanical properties is presented.

3.1 Materials

All the materials investigated in this study are experimental steels procured from different vendors, viz., OCAS, Belgium (DQP steels) and Outokumpu Oy (Medium-Mn steels), Tornio, Finland. The chemical compositions of the steels were suitably designed to understand the efficacy of the DQP (I–V) and the ART (Publication VI) processes, with a thorough investigation planned in respect of understanding the effects of alloying elements and processing parameters on the evolving microstructures, related mechanisms, and corresponding mechanical properties. The DQP medium carbon steels with ~0.3 wt.% C were alloyed with either Si or a combination of Si with Al to prevent the formation of carbides and/or retard their growth during the partitioning process. For the ART processing, medium-Mn steels were suitably alloyed with high Mn contents (3–4 wt.% Mn) to be able to accomplish high retained austenite fractions after reversion treatment. To accomplish low impurity levels, steels for DQP and ART processing were vacuum induction melted and cast as laboratory-size ingots, each weighing about 65 kg. The chemical compositions of the steels are shown in Table 2, along with a mention of the publications, in which the investigation details and results are summarized.

Table 2. Chemical compositions of experimental steels [Publications I–VI].

Material	Alloying element content (wt.%)										
	C	Si	Mn	Al	Cr	N	S	P	Ni	Mo	V
Publication I, III, IV, V											
Steel A (High-Al)	0.30	0.56	2.00	1.10	2.20	0.0010	0.0010	0.0010	-	-	-
Steel B (High-Si)	0.30	0.99	1.86	0.01	1.01	0.0031	0.0009	0.0026	-	-	-
Publication I											
Steel C (Al-Si)	0.29	0.48	1.88	0.49	1.02	0.0030	0.0009	0.0017	-	-	-

Material	Alloying element content (wt.%)										
	C	Si	Mn	Al	Cr	N	S	P	Ni	Mo	V
Publication II											
2Mn-1Si	0.30	0.99	1.86	0.01	1.01	0.0031	0.0009	0.0026	-	-	-
3Mn-1.5Si	0.25	1.45	2.91	0.02	0.01	-	-	-	-	-	-
Publication VI											
Steel A	0.30	1.0	2.9	0.47	-	-	-	-	1.0	0.20	-
Steel B	0.31	1.0	3.9	0.42	-	-	-	-	2.0	0.21	-
Steel C	0.32	1.0	2.7	0.54	-	-	-	-	1.3	0.41	0.20

3.2 Gleeble simulations

Prior to Gleeble simulations, all the experimental steels were soaked for two hours at 1200 °C in a furnace, followed by hot rolling to 12 mm thickness. After hot rolling, cylindrical specimens of dimensions Ø6 x 9 mm were machined for conducting QP and ART treatments in a Gleeble 3800 thermomechanical simulator. In addition, specimens of dimensions Ø8 x 10 mm suitable for stress relaxation testing were machined for conducting studies on the static recrystallization characteristics and kinetics of select steels, as reported in Publication II. To understand the effect of grain size and prior deformation on subsequent austenite decomposition characteristics during QP processing, two sets of parallel experiments were carried out in the Gleeble simulator: without or with a prior straining step, as shown in Fig. 3a and b, respectively (Publication I). To investigate the static recrystallization (SRX) characteristics of select steels, stress relaxation testing was carried out on the Gleeble simulator over a wide range of temperature, strain, strain rate and grain size. The experimental plan is schematically presented in Fig. 3c (Publication II). In Publication IV, dilatation measurements were made by employing a contact dilatometer in the Gleeble simulator to be able to estimate the initial martensite fractions during the QP processing using linear analysis. For medium Mn steels, the aim of Gleeble simulation trials was to compare their microstructural response on the QP and ART processing route, as shown in Fig. 3a and d, respectively (Publication VI).

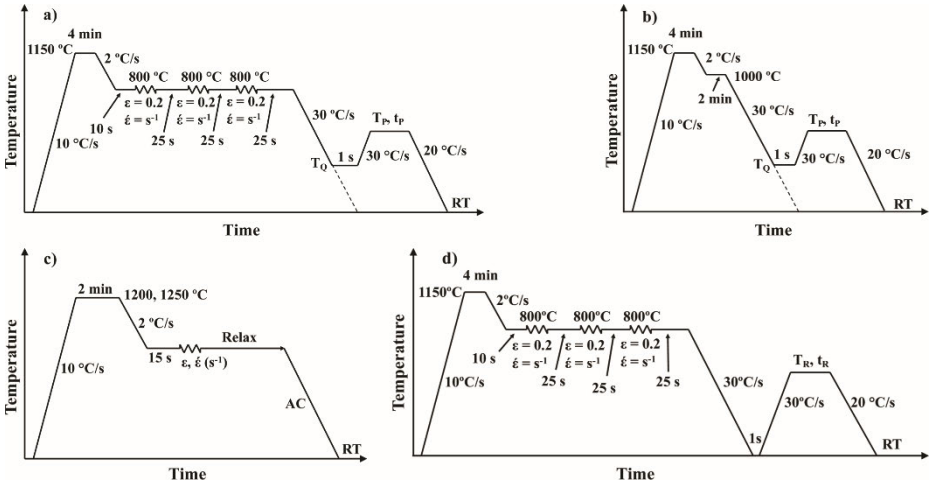

Fig. 3. Schematic sketches of QP processing schedules with prior straining a) and without straining b), stress relaxation testing c) and ART processing schedule d) (Adapted, with permission, from Publications I, II and VI).

Table 3 lists (i) the experimental ranges of T_Q and T_P temperatures and t_P times for QP experiments, (ii) the deformation temperatures (T), strains (ε) and strain rates ($\dot{\varepsilon}$) for stress relaxation, and (iii) the T_R temperatures and t_R times for ART processing. In Publication VI, the details of studies carried out on medium-Mn steels, encompassing various QP and ART treatments, respective microstructures, mechanisms, and mechanical properties are presented. On the other hand, Publications III and V did not have any Gleeble simulation tests and, hence, they are not included in Table 3.

Table 3. Schedules for Gleeble tests.

Treatment	T_Q (°C)	T_P (°C)	t_P (s)	T (°C)	ε	$\dot{\varepsilon}$ (s^{-1})	T_R (°C)	t_R (s)
Publication I								
QP	200–260	200–400	10–1000	-	1	0.2	-	-
Publication II								
SRX	-	-	-	850–1200	0.125–0.4	0.01–5	-	-
Publication VI								
QP	100–150	200–500	1000	-	1	0.2	-	-
ART	-	-	-	-	1	0.2	630–770	100–5000

3.3 Thermomechanical rolling

Based on the results of Gleeble QP simulations, the potential use of thermomechanical rolling followed by direct quenching and partitioning (TMR-DQP) was investigated. In Publications III and IV, the results of TMR-DQP experiments conducted on Steel A (High Al) and Steel B (High Si) are reported. Thermomechanical rolling trials were carried out in a two-high, reversing laboratory rolling mill equipped with direct quenching facilities. Blocks of dimensions ~120x80x60 mm were cut from the cast ingots and subjected to thermomechanical rolling in accord with planned rolling schedules comprising recrystallization-controlled rolling followed by controlled rolling in the T_{NR} regime, resulting in 12 mm thick plates. A schematic of the TMR-DQP schedules is shown in Fig. 4, with the FRT controlled at 820 °C. Samples from laboratory hot rolling simulations were further used for the evaluation of mechanical properties and microstructure characterization.

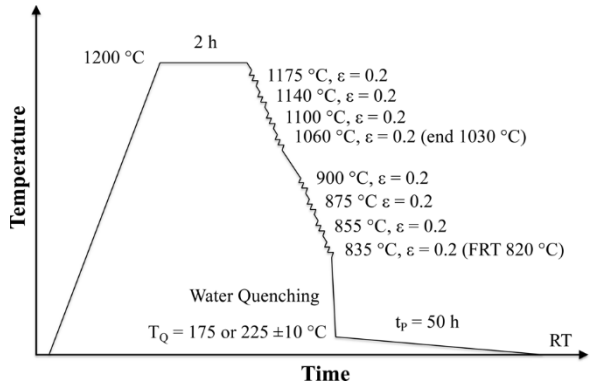

Fig. 4. Schedules for thermomechanical rolling followed by direct quenching and partitioning.

For carrying out preliminary tensile property evaluation of the QP- and ART-treated medium-Mn steel samples (Publication VI), a number of blocks of 120x75x55 mm were cut from the cast ingots, followed by thermo-mechanical rolling on the laboratory rolling mill, as per the schedule presented in Table 4. The final thickness of the rolled plates was ~6 mm. After the last pass, samples for QP treatment were immediately quenched to the desired T_Q temperature (100 or 150 °C) and quickly transferred to a furnace maintained at the preferred T_P temperature (350 or 400 °C). These samples are termed as TMR-QP-processed medium-Mn steel samples. The

samples were held in the furnace for a short partitioning duration (t_P) of 1000 s, followed by quenching to RT. Some of the quenched samples were later moved to a furnace maintained at the desired T_R temperature (630 or 710 °C) for enabling the ART treatment and held for t_R = 1000 or 5000 s, followed by quenching to RT. These samples are termed as TMR-ART-processed medium-Mn steel samples.

Table 4. Thermomechanical rolling schedule of Med-Mn steel samples prior to QP and ART treatments.

Thickness (mm)	Strain	Rolling temperature (°C)
55	-	1250 °C
41	0.29	n.a.
31	0.28	n.a.
23	0.30	~1200
-	-	Reheating
17	0.30	1150
12	0.35	1100–1120
8	0.41	1010–1030
5.8	0.32	890–920

3.4 Microstructural characterization

The microstructural characterization of the studied materials was carried out using the facilities available both at the Centre for Material Analysis, as well as Materials and Mechanical Engineering Research group, University of Oulu. To reveal the microstructural details, specimens were polished using standard metallographic procedure according to the ASTM E3 standard and etched with Nital solution (2 vol.%). General microstructural features were examined by employing a Keyence VK-X200 laser scanning confocal microscope (LSCM) and a Nikon Eclipse MA100 light optical microscope (LOM). A Zeiss Sigma field emission scanning electron microscope (FESEM) was utilized for detailed microstructural characterization at higher magnifications. In Publications I and VI, high resolution metallographic examinations were conducted utilizing a 200-kV Jeol JEM-2200FS energy-filtered scanning transmission electron microscope (EFTEM/STEM). Thin slices (~100 μm) of samples were cut to prepare the thin foils for the TEM study. The foils were further grounded to ~80 μm followed by punching 3 mm discs using a Gatan disc punch system and subjected to twin-jet electro-polishing at 23.5 V using an electrolyte consisting of 75 ml perchloric acid, 90 ml distilled water, 100 ml butyl Cellosolve and 730 ml ethanol. The electrolyte was maintained at −5 °C.

For investigated steels, it was not possible to satisfactorily reveal the parent austenite grain structure using different etching reagents and techniques. Therefore, the EBSD facility equipped with the FESEM was used for studying the microstructures, whereby the reconstruction of prior austenite grain boundaries was carried out using the inverse pole figures (IPF) data (Publication I). For grain reconstruction, based on K-S orientation relationship between the austenite and resultant martensite and/or bainite, the Matlab software with an MTEX toolbox was employed [74]–[76].

The cleanness measurements were performed using a Jeol JMS 7000 FESEM equipped with an energy-dispersive spectrometer (EDS) for the detection of the inclusions in the steels (Publication I).

The RA fractions of the steel samples were determined by employing the XRD technique. For the RA fraction measurements in Publication I, a Siemens D500 X-ray diffractometer was used, where the X-ray radiation source was a Mo-K_α anode and the unit were operated at 40 mA and 40 kV conditions with 2θ angle ranging from 18.5 to 42°. On the other hand, a Rigaku SmartLab 9kW XRD unit with a Co-K_α source combined with PDXL2 analysis software was used for the determination of different phases including RA fractions, and the results were reported in Publications III–VI. During the XRD measurements, the samples were tilted (chi, χ) with 10° steps from 0 to 60° and rotated (phi, ϕ) 360°. This de-texturing method was used to eliminate any possible effects of crystallographic texture of the steel samples on the phase fraction measurements. The average carbon contents in the RA for QP- and DQP-processed steels were estimated based on the lattice parameter measurements using the following empirical equation [77], [78]

$$\begin{aligned} a_\gamma = {} & 3.556 + 0.0453x_{\mathrm{C}} + 0.00095x_{\mathrm{Mn}} + 0.0056x_{\mathrm{Al}} \\ & + 0.0006x_{\mathrm{Cr}} - 0.0002x_{\mathrm{Ni}} + 0.0031x_{\mathrm{Mo}} + 0.0017x_{\mathrm{V}}, \end{aligned} \quad (1)$$

where a_γ is the lattice parameter (Å) and x_C, x_{Mn}, x_{Al}, x_{Cr}, x_{Ni}, x_{Mo} and x_V are the concentrations (in wt.%) of C, Mn, Al, Cr, Ni, Mo, and V, respectively. As Equation 1 overestimated the carbon contents of ART-processed steels, a_γ was determined using equation [79]

$$\begin{aligned} a_\gamma = {} & 3.578 + 0.033x_{\mathrm{C}} + 0.00095x_{\mathrm{Mn}} + 0.0056x_{\mathrm{Al}} \\ & - 0.0002x_{\mathrm{Ni}} + 0.0031x_{\mathrm{Mo}} + 0.0018x_{\mathrm{V}}. \end{aligned} \quad (2)$$

To determine the microtexture of TMR-DQP samples, a Zeiss Ultra Plus FESEM-EBSD was used, and the results are presented in Publication IV. As reported in

Publication VI, the local variation of Mn and other alloying elements was detected using a Jeol JXA-850FPlus EPMA.

3.5 Mechanical testing

Vickers hardness measurements were conducted on the Gleeble simulated QP samples using a 5 kgf load (Publication I). On the other hand, Vickers hardness measurements were performed using a 10 kgf load for TMR-DQP samples (Publications III and IV). For tensile testing at room temperature, samples were machined according to the SFS-EN ISO 6892-1 standard with the axis of the bar transverse to the longitudinal direction in the rolling plane for the TMR-DQP steels and the corresponding dimensions were: size Ø6 mm gauge diameter (d_{gauge}), 40 mm length of reduced section (L_C) and gauge length 30 mm (L_0). Similar samples were also used to conduct the interrupted tensile tests. For tensile tests conducted on medium-Mn steels, as reported in Publication VI, samples of dimensions: d_{gauge} Ø4 mm, L_C 25 mm and L_0 20 mm were machined from TMR-QP and TMR-ART samples, in accordance with the standard ASTM/ E8/E8M – 16a, wherein the axis of the sample was parallel to the longitudinal direction in the rolling plane. All the tensile tests were carried out in a 100-kN Zwick Roell Z100 tensile testing equipment.

To evaluate the impact toughness of the TMR-DQP-processed medium-C steels, Charpy V notched specimen were machined (according to EN 10045-1 standard) with the axis of the bar parallel to the longitudinal direction in the rolling plane and the tests were carried out in the temperature range −120 to 40 °C (Publications III and IV).

Wear tests were conducted using an impeller-tumbler device at the Tampere Wear Center (TWC), Tampere University, Finland for TMR-DQ and TMR-DQP (at T_Q 175 and 225 °C) processed Steel A (High-Al) and Steel B (High-Si) samples. (Publication V) [80]. The specified sample dimensions for these tests were 75×25 ×10 mm, and two such samples were tested for each steel type. The samples were rotated at high speed by the impeller, whereas the tumbler rotated slowly in the same direction as the impeller enabling lifting of the crushed and sieved dry natural granite (10–12 mm size) used as the abrasive in the tests. Test time was 60 min, and a 15 min running-in phase was done before the actual test to enable the removal of any debris that may have been left by machining of the samples and ensure steady-state wear. The mass of the samples was measured before and after testing every

15 min. The gravel used for the tests was replaced every 15 minutes with a fresh batch of abrasives.

4 Results

The effect of chemical composition and processing parameters on the evolved microstructures and corresponding mechanical properties of experimental high/ultrahigh strength martensitic QP/DQP steels, as well as medium-Mn QP and ART steels, containing various fractions of RA, are broadly elucidated in this chapter. Results from Publications I–VI are summarized here, adapting in outline the similar order of subchapters content as in respective publications.

4.1 Effect of deformation and grain size on austenite decomposition during quenching and partitioning

The effect of QP processing parameters and prior deformation on the subsequent austenite decomposition in High-Al, High-Si and Al-Si steels (Steels A, B and C, respectively) was studied in Publication I. The main objective here was to provide an insight into the structural mechanisms such as carbon partitioning, decomposition of austenite into isothermal martensite and/or bainite and formation of high carbon, untempered FM during final cooling to RT. The fundamental aim of this research work was to optimally design the DQP processes for developing the novel AHSSs.

4.1.1 Microstructural characterization

Both LOM and LSCM metallography techniques illustrated the overall microstructures essentially comprising martensitic laths in both unstrained and strained conditions for the studied steels. Because structures were too fine to discern the presence of carbides or any other phases using LOM and LSCM techniques, both FESEM-EBSD and TEM were employed to reveal the fine microstructures. Fig. 5a-c reveals an example of microstructures recorded on QP-treated Steel A at high magnifications using the FESEM. The samples quenched at 260 °C and partitioned at 300 °C for t_P = 1000 s revealed the occurrence of TM, RA, some lower bainite and FM. The straining of the matrix did result in the occurrence of similar microstructural features as in the case of unstrained samples, but with a significantly refined grain structure, as shown in Fig. 5a and b. In comparison, the samples quenched and partitioned at 200 °C for a short holding time of t_P = 10 s resulted in a higher fraction of fresh martensite, besides retaining a small fraction of RA at room temperature, as shown in Fig. 5c. Needle-shaped,

transition type carbides were observed in all the samples within the primary martensite, even in direct quenched specimens [81].

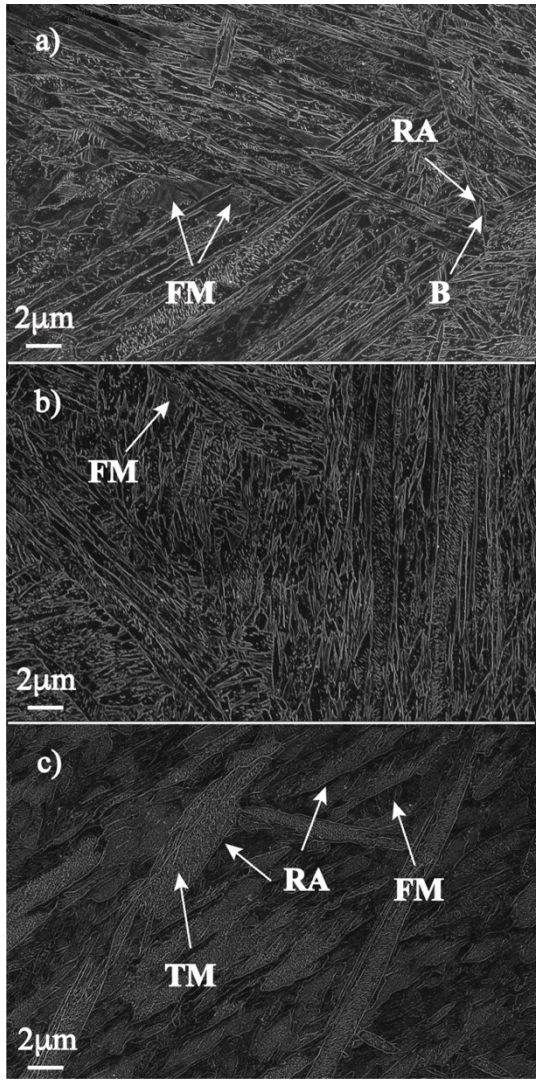

Fig. 5. Micrographs of QP-treated Steel A illustrating various phase constituents as fresh martensite (FM), retained austenite (RA), bainite (B), tempered martensite (TM), shown by arrows: a) unstrained; T_Q = 260 °C, T_P = 300 °C and t_P = 1000 s, b) strained; T_Q = 260 °C, T_P = 300 °C and t_P = 1000 s and c) unstrained; T_Q = T_P = 200 °C and t_P = 10 s (Reprinted under CC BY-NC-ND 4.0 license from Publication I © 2020 Authors).

EBSD investigations were conducted for both the unstrained and strained samples subjected to QP treatment at T_Q and T_P 260 °C, and for the short partitioning time of t_P = 10 s to examine the effect of prior straining on the evolved microstructures. According to the IPF and the corresponding relative area fractions of the equivalent circle diameters of the martensite blocks, the block size distribution trend was almost same for the studied steels, both in unstrained and strained conditions. The observed maximum block sizes were ~35 µm and ~12 µm in unstrained and strained conditions, respectively. The reconstructed austenite grain structures of the strained specimens showed apparently partially recrystallized structures, as shown in Fig. 6. These were also discerned using the LSCM, which showed fine grains between the pancaked grains, i.e., partially recrystallized austenite grain structures (Fig. 7). The size of the reconstructed austenite grains ranged from 2 µm to 32 µm in the strained samples.

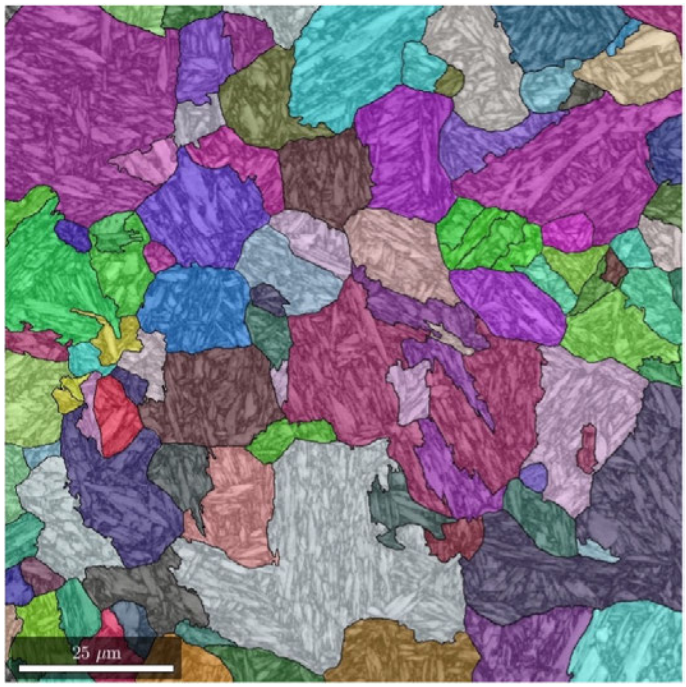

Fig. 6. Reconstructed prior austenite grain structure of the strained Steel B QP specimen treated at T_Q and T_P 260 °C and t_P 10 s (Adapted under CC BY-NC-ND 4.0 license from Publication I © 2020 Authors).

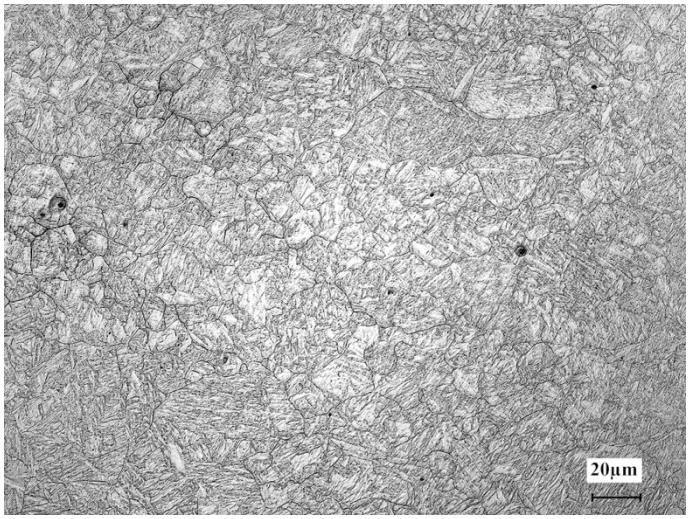

Fig. 7. Laser scanning confocal micrograph recorded on strained Steel B sample treated at T_Q and T_P 260 °C and t_P 10 s (Reprinted under CC BY-NC-ND 4.0 license from Publication I © 2020 Authors).

TEM examinations were carried out to reveal further the martensitic lath microstructure as well as the morphology of RA for Steels A, B and C. The TEM examination of thinned discs revealed the morphology of fine interlath austenite films, tiny pools of RA, formation of lower bainite, the ledged growth of martensitic laths (isothermal martensite) and formation of twinned martensite during final cooling.

4.1.2 Austenite fraction

To design the parameters for QP processing, there is an essential need to determine the M_s and M_f temperatures for having a good understanding of the martensite fraction at a given T_Q as well as the amount of untransformed austenite that is available for stabilization at room temperature after optimal partitioning. Different methods have since been employed to determine the austenite fractions following QP processing at different conditions for the examined steels. In this study, both the dilatometry measurements and the Koistinen-Marburger (K-M) equation were used in order to attempt to determine the fractions of untransformed austenite at T_Q that can be fully or at least partly stabilized down to RT [82], [83]. XRD analysis

was used to determine the fractions of RA in the steel samples and their respective carbon contents.

Experimentally determined M_s temperatures along with the initial volume fractions of martensite (V_M) and austenite (V_A), calculated from K-M equation, are listed in Table 5 for the examined steels. The initial transformed martensite fractions ($V_{Mdilatation}$) at T_Q of 200 and 260 °C were determined according to a simple linear analysis of the dilatation curves recorded on the studied steels, as shown in Table 5.

Table 5. The calculated martensite (V_M) and austenite (V_A) volume fractions using the K-M equation, and the corresponding martensite volume fractions based on the dilatation tests ($V_{Mdilatation}$) for Steels A, B and C at two different quenching temperatures (T_Q). Martensite start temperatures (M_s) are also included in the table. (Reprinted under CC BY-NC-ND 4.0 license from Publication I © 2020 Authors).

Material	M_s	T_Q	V_M	V_A	$V_{Mdilatation}$
	(°C)	(°C)	(%)	(%)	(%)
Steel A	340	200	93	7	85
Steel B	325	200	93	7	85
Steel C	350	200	95	5	86
Steel A	340	260	80	20	69
Steel B	325	260	80	20	66
Steel C	350	260	85	15	75

After quenching to T_Q, subsequent partitioning at T_Q or higher temperatures for various holding times led to a wide range of RA contents. Table 6 and Table 7 summarize the RA fractions of studied steels along with their carbon contents, measured for both unstrained and strained samples, respectively.

Table 6. Retained austenite fractions along with their carbon contents for unstrained QP samples (Adapted under CC BY-NC-ND 4.0 license from Publication I © 2020 Authors).

Unstrained			Steel A		Steel B		Steel C	
T_Q (°C)	T_P (°C)	t_P (s)	RA (vol.%)	RA (C%)	RA (vol.%)	RA (C%)	RA (vol.%)	RA (C%)
200	260	1000	12	-	9	-	8	-
200	300	1000	15	0.55	8	-	7	-
200	350	100	13	0.80	16	0.64	7	-
200	350	1000	13	0.65	11	0.95	7	-
260	260	1000	10	-	9	-	6	-
260	350	100	15	0.58	13	0.64	10	-

Unstrained			Steel A		Steel B		Steel C	
T_Q (°C)	T_P (°C)	t_P (s)	RA (vol.%)	RA (C%)	RA (vol.%)	RA (C%)	RA (vol.%)	RA (C%)
260	400	10	15	-	12	0.53	11	0.90
260	400	100	22	0.72	14	0.73	10	0.90
260	400	1000	16	0.76	15	0.82	10	0.92

Table 7. Retained austenite fractions along with their carbon contents for strained QP samples (Adapted under CC BY-NC-ND 4.0 license from Publication I © 2020 Authors).

Strained			Steel A		Steel B		Steel C	
T_Q (°C)	T_P (°C)	t_P (s)	RA (vol.%)	RA (C%)	RA (vol.%)	RA (C%)	RA (vol.%)	RA (C%)
200	260	1000	12	0.48	11	-	12	0.52
200	300	1000	13	0.60	13	0.74	11	0.87
200	350	100	16	0.74	12	0.66	13	1.05
200	350	1000	14	0.76	14	0.78	17	1.06
260	260	1000	12	0.64	10	-	13	0.89
260	350	100	16	0.64	11	0.71	12	0.64
260	400	10	16	0.70	15	0.54	14	0.61
260	400	100	22	0.55	21	0.74	12	0.75
260	400	1000	21	0.69	14	0.75	11	0.67

4.1.3 Hardness

An increase in the partitioning parameters, T_P and t_P, resulted in a consequent decrease in Vickers hardness for the studied steels. However, increasing the T_Q from 200 to 260 °C seemed to have only a marginal influence on the hardness as shown in Fig. 8. In the case of unstrained samples, the hardness values are of the same order as observed on the strained samples.

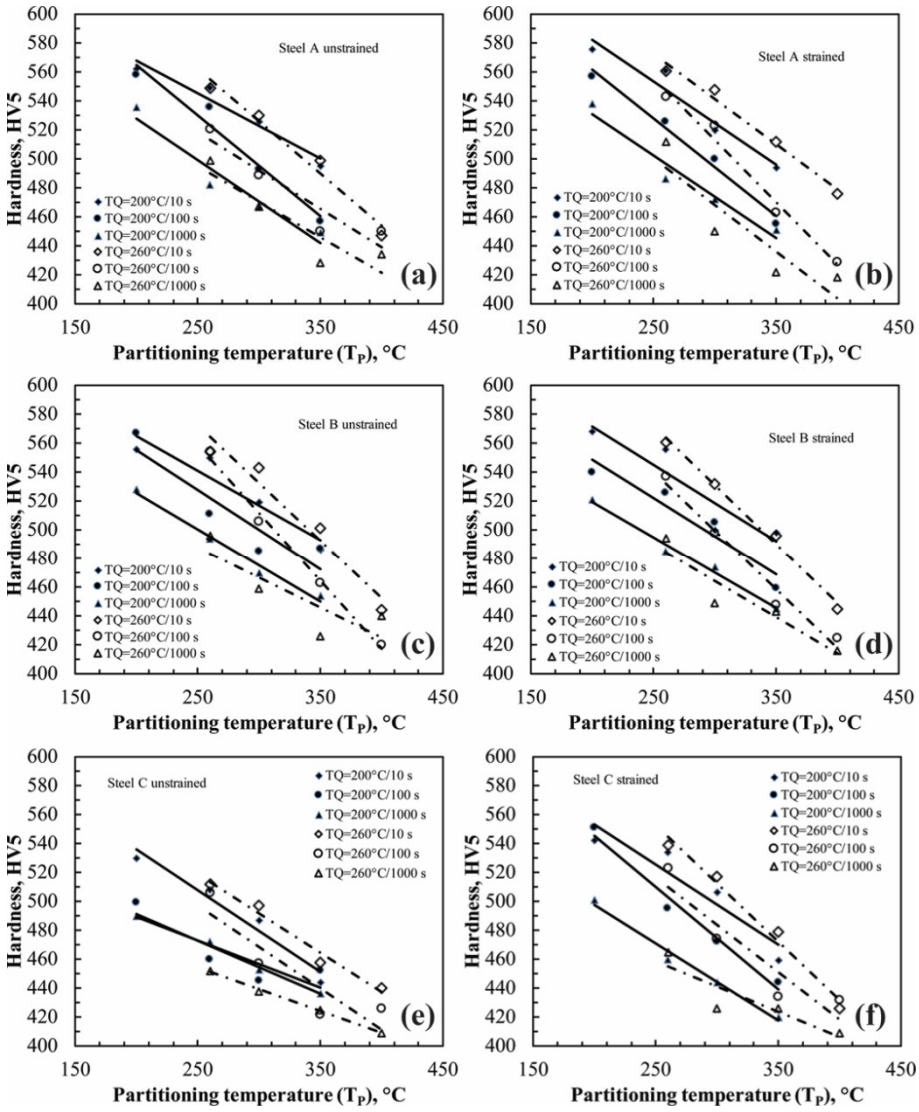

Fig. 8. The range of Vickers hardness (HV5) at T_Q 200 and 260 °C when T_P vary from 200 to 400 °C and t_P from 10 to 1000 s (Adapted under CC BY-NC-ND 4.0 license from Publication I © 2020 Authors).

4.1.4 Dilatation measurements

During partitioning, several mechanisms may operate in parallel or succession, thereby simultaneously affecting the variation in specimen diameter due to dimensional changes. Carbon partitioning starts immediately below M_s during cooling to T_Q and continues thereafter explaining a small part of dilatation during holding at T_P. Fig. 9 shows examples of the variation of sample diameter with holding time after quenching to T_Q, followed by holding at T_P. The dilatation curves showed a gradual expansion during holding and the magnitude was far greater than the dilatation predicted by carbon partitioning alone, thus implying that the austenite decomposition continued during the hold. Three distinct regions (region I–III) can be clearly identified in these dilatation curves, as shown in Fig. 9. After 1 s holding at T_Q, heating at T_P occurs at 30 °C/s, which explains most of the expansion immediately after 1 s. Apart from this, on a logarithmic scale, the diameter increases slowly (region I) and then more rapidly (region II). Together with carbon partitioning, the expansion observed in region I is probably due to the formation of isothermal martensite leading to the formation and migration of ledges that allow the martensitic laths to grow into the austenite isothermally.

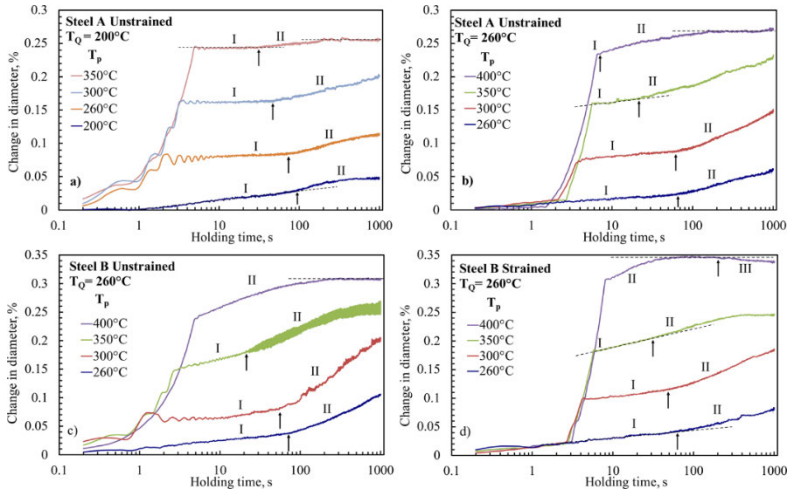

Fig. 9. Variation of specimen diameter with partitioning time at different partitioning temperatures. Unstrained Steel A specimens are quenched at 200 °C a) and 260 °C b). Unstrained c) and strained d) Steel B samples are quenched at 260 °C. The arrows indicate the start of region II and III (Adapted under CC BY-NC-ND 4.0 license from Publication I © 2020 Authors).

The rate of dilatation beyond region I increases abruptly. Some austenite pools transform to lower bainite affecting acceleration of dilatation, marked as region II in Fig. 9.

In this study, it seems that prior straining close to T_{NR}, in general, did not facilitate acceleration of bainite formation during subsequent partitioning. The highest amount of bainite formed in the specimen quenched at T_Q 260 °C, followed by partitioning at T_P 300 °C. At the highest T_P, the strained sample showed accelerated tempering of martensite during partitioning, possibly as a consequence of prior deformation in the T_{NR} regime prior to QP treatment. The contraction due to the tempering of martensite can be clearly seen in region III of the dilatation curve at T_P 400 °C, Fig. 9d. No evidence of carbide precipitation in martensite was apparent even for QP sample partitioned at high T_P of 400 °C. Carbon might have probably clustered, but there was no evidence of formation of carbides, as noted in the TEM study.

During the final cooling after the partitioning treatment, some bainite formation is possible, particularly in the case of high T_P, followed by the formation of untempered, and in some cases, twinned, high carbon martensite (FM) starting at temperatures close to 200 °C. This FM formation was clearly evident in both unstrained and strained samples, held for shortest partitioning times.

4.2 Static recrystallization characteristics and kinetics for direct quenching and partitioning

In Publication II, the SRX characteristics of a 2Mn-1Si steel (same as Steel B in publication I) were evaluated in comparison with a new experimental steel 3Mn-1.5Si (see Table 2) and kinetics modelled utilizing a fractional softening approach combined with metallography to determine the time for 50% recrystallization as a function of grain size, strain, strain rate and temperature.

4.2.1 Flow stress behavior

The flow stress behavior of steel specimens tested in the temperature and strain rates ranges of 850–1200 °C and 0.001 to 5 s^{-1}, respectively, with the true strain ranging from 0.125 to 0.4 was characterized, and examined in respect of the test conditions, where the deformation reached the critical strain for the initiation of dynamic recrystallization (ε_c). ε_c is considered ~0.8 times the peak strain (ε_p) [84], [85]. Following hot compression to 0.2 strain, subsequent relaxation should exhibit

static restoration (recovery and recrystallization) processes, except presumably at 1100 °C in the case of 2Mn-1Si steel and at 1150–1200 °C in the case of 3Mn-1.5Si steels, as the critical strain ε_c might be exceeded. There were no significant differences in flow stress levels between these two steels.

4.2.2 Effect of processing parameters and grain size on static recrystallization rate

Semi-empirical fractional softening equations describing the SRX kinetics can be used in the design of the rough rolling part of the thermomechanical processing. Generally, the time for 50% recrystallized fraction (t_{50}) can be described by the following semi-empirical equation [85]

$$t_{50} = A\varepsilon^p \dot{\varepsilon}^p d^s \exp\left(Q_{app}/RT\right), \quad (3)$$

where A is material constant, Q_{app} is apparent activation energy of recrystallization, d is grain size, R is the gas constant, T is absolute temperature and p, q and s are the material dependent constants describing the power of strain, strain rate and the grain size, respectively.

The SRX rate can be reasonably described for 2Mn-1Si and 3Mn-1.5Si Steels by the SRX equations

$$t_{50} = 1.17 \times 10^{-13} \varepsilon^{-2.8} \dot{\varepsilon}^{-0.23} d^s \exp(224600/RT) \quad (4)$$

and

$$t_{50} = 5.73 \times 10^{-14} \varepsilon^{-2.35} \dot{\varepsilon}^{-0.14} d^s \exp(240600/RT), \quad (5)$$

which are determined on the basis of stress relaxation experiments conducted on the Gleeble simulator over wide ranges of temperature, strain, strain rate and initial grain size, as presented in Publication II. The power of grain size is described by the relation $s = 2.13d^{-0.105}$ [86], [87].

In 2Mn-1Si Steel, with an increase in temperature from 850 to 1100 °C, the rate of SRX increased significantly. Complete softening was obtained in most cases, except at the lower temperatures (≤900 °C). For example, the time for 50% recrystallization (t_{50}) decreased from 68 s at 900 °C to 3.7 s at 1100 °C. On the other hand, coarse grained samples (~400 μm) deformed at 1000 °C/0.1 s^{-1} to 0.2 strain clearly revealed the retardation of SRX rate (t_{50} = 24 s) in comparison to that of the fine-grained samples (~115 μm; t_{50} = 13 s) under similar deformation conditions.

In 3Mn-1.5Si Steel, the t_{50} decreased from 37 s at 950 °C to 2.1 s at 1150 °C following deformation to 0.2 strain at 0.1 s^{-1}. Coarse-grained samples (~480 μm) deformed at 1050 °C / 0.1 s^{-1} to a true strain of 0.2 retarded the SRX rate (t_{50} = 12 s) in comparison to that of the fine-grained samples (~80 μm; t_{50} = 2.6 s) under similar deformation conditions. Data analysis resulted in the estimation of the powers of strain (–2.8 and –2.4) and strain rate (–0.23 and –0.14) and the recrystallization activation energies (303 and 289 kJ mol^{-1}) for the 2Mn-1Si and 3Mn-1.5Si steels, respectively. This suggests that increasing the contents of Mn and Si made the recrystallization kinetics less sensitive to strain, strain rate and temperature, i.e., the powers of strain and strain rate became less negative, and the activation energy of recrystallization was marginally reduced.

4.3 Microstructural characterization and mechanical properties after direct quenching and partitioning treatment

In Publications III and IV, the study mainly focused on the evaluation of the microstructures and mechanical properties of High-Al (Steel A) and High-Si (Steel B) steels, which were processed via TMR-DQP. At the end of this chapter, the impact-abrasive wear performance of TMR-DQ-processed Steels A and B in comparison to their TMR-DQP counterparts, as reported in Publication V, is also considered.

4.3.1 Determination of M_s temperature

According to the dilatation tests carried out in the Gleeble 3800 simulator, the M_s temperatures for both QP steels was very close to 325 °C, even though there were significant differences in Si, Al and Cr contents of Steels A and B, as shown in Table 2.

4.3.2 Retained austenite of hot-rolled and partitioned materials

The targeted austenite phase fractions at the chosen T_Q 175 and 225 °C were in ranges of 5–10 and 10–15%, respectively, depending on the stabilization during the subsequent partitioning treatment. According to the K-M equation, corresponding martensite phase fractions at T_Q 175 and 225 °C were 93 and 83%, respectively, for both the investigated steels [82], [83]. During TMR-DQP processing, following quenching at T_Q 175 and 225 °C, the corresponding RA fractions of ~6 and ~10%,

respectively, were obtained for both the examined Steels A and B after slow cooling of the samples in the furnace for several hours. Fig. 10 shows RA fractions of TMR-DQ and TMR-DQP-processed samples and the corresponding hardness values (HV10) plotted against T_Q. The average carbon contents of RA at T_Q 175 °C were determined to be 0.60 and 0.61%, respectively, for Steels A and B. In comparison, the average carbon contents of RA quenched at T_Q 225 °C were 0.65 and 0.94%, respectively.

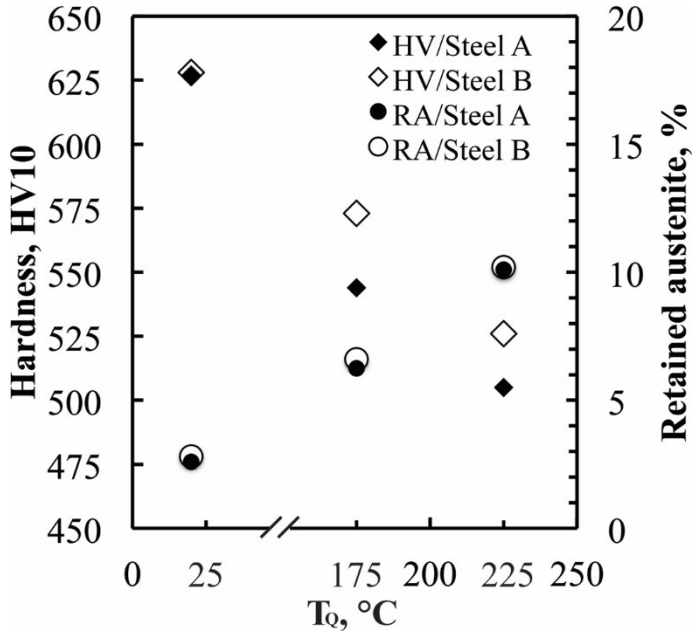

Fig. 10. Effect of quenching temperature (T_Q) on volume fraction of retained austenite (RA) and HV10 hardness in TMR-DQP-processed samples (Reprinted under CC BY 4.0 license from Publication IV © 2019 Authors).

4.3.3 Microstructural characterization

According to LOM characterization, the overall microstructure of both TMR-DQP-processed samples was lath martensite. A more detailed characterization at high magnifications was done using the FESEM for both steels quenched at T_Q 175 and 225 °C, followed by partitioning during slow cooling in furnace. The Investigated steels revealed the occurrence of TM, RA and FM in the

microstructures, as shown in Fig. 11. These microstructures also revealed the occurrence of small carbides, presumably transition ε-carbides, as also seen in Gleeble simulated QP samples of Steels A and B, see Fig. 5 [38].

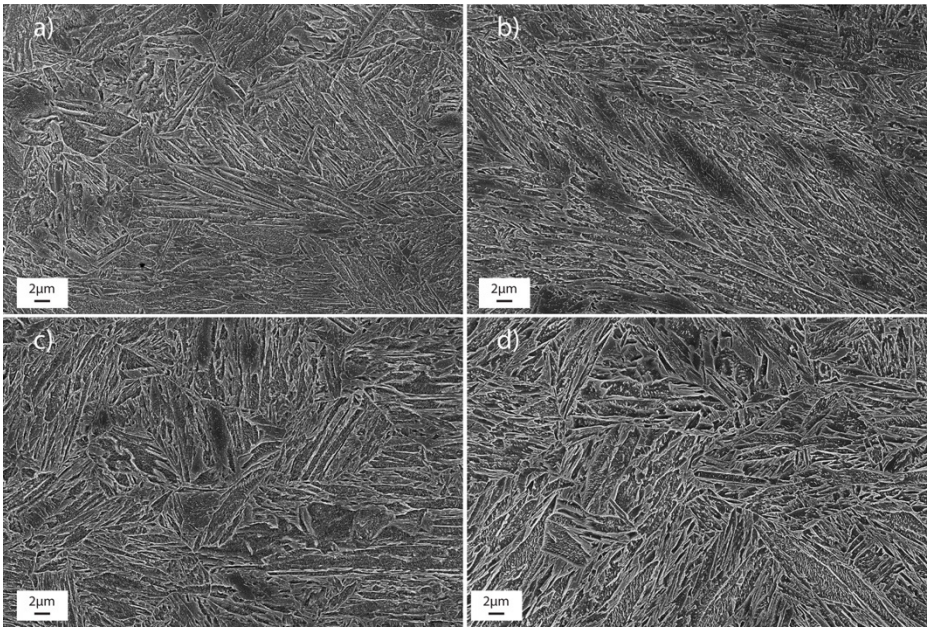

Fig. 11. FESEM micrographs of the martensitic structure of TMR-DQP processed samples. Steel A, a) at T_Q 175 °C and b) 225 °C; and Steel B, c) at T_Q 175 °C and d) 225 °C (Reprinted under CC BY 4.0 license from Publication IV © 2019 Authors).

Thin film TEM investigations for TMR-DQP-processed Steel B revealed that the specimens contained essentially thin films of interlath austenite, besides micrometer-scale pools of RA, as reported in Publication III. Typical examples of bright field (BF) and dark field (DF) images are shown in Fig. 12a and b revealing interlath austenite between martensite laths.

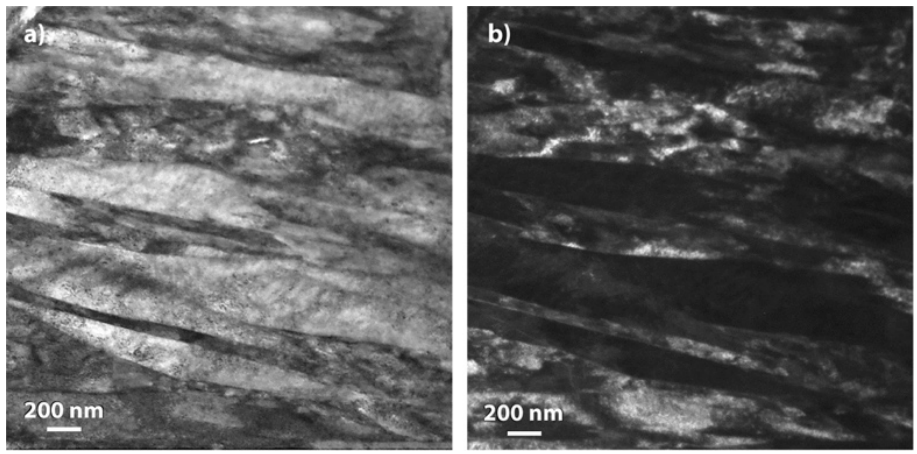

Fig. 12. TEM micrographs recorded on TMR-DQP-treated Steel B illustrating lath martensite with interlath austenite, a) dark in BF image and b) white in DF image.

The EBSD texture analysis indicated weak texture intensity for TMR-DQP-treated steels. The highest texture peaks, 4.2 for {112}<110> and 2.8 for {554}<225>, were observed for Steel A at T_Q 175 °C. In comparison, for a pilot-scale hot rolled and direct quenched C-Si-Mn-Cr-Ti-B ultra-high strength steel, texture intensity peaks as high as 6 for {112}<110> and 7 for {554}<225> were reported [88].

Mean lath size (d_1), mean effective grain size (d) and effective grain size at 90% in the cumulative size distribution ($d_{90\%}$) were determined using the EBSD data for the TMR-DQP samples of Steels A and B (Table 8). Equivalent circle diameter (ECD) values were used as the measure of prior austenite grain sizes (PAGSs). Both the PAGSs as well as grain aspect ratios are included in Table 8. Grain pancaking was small, i.e., grain aspect ratios were low (1.26–1.50). In comparison, low carbon steels subjected to similar laboratory rolling practice did exhibit high aspect ratios of up to 3.5 [89].

Table 8. Prior austenite grain size (PAGS), grain aspect ratio, mean lath size (d_1), mean effective grain size (d) and effective grain size at 90% in the cumulative size distribution ($d_{90\%}$) for TMR-DQP-processed steels (Adapted under CC BY 4.0 license from Publication IV © 2019 Authors).

Steel (T_Q)	PAGS (μm)	Aspect Ratio	d_1 (μm)	d (μm)	$d_{90\%}$ (μm)
Steel A (175 °C)	14.6	1.50	1.28 (±0.025)	1.61 (±0.063)	9.27
Steel A (225 °C)	15.0	1.26	1.29 (±0.026)	1.60 (±0.059)	8.77
Steel B (175 °C)	14.7	1.33	1.33 (±0.021)	1.40 (±0.073)	10.95
Steel A (225 °C)	14.8	1.34	1.32 (±0.029)	1.63 (±0.071)	10.59

4.3.4 Mechanical properties

Table 9 presents a summary of the mechanical properties obtained on TMR-DQ and TMR-DQP-processed samples of Steels A and B. For ready reference, the fractions of retained austenite and corresponding carbon contents for both Steels A and B are also included in Table 9 As expected, DQP processing resulted in somewhat lower hardness and strength values in comparison with the corresponding DQ-processed versions. However, DQP steels showed reasonably high hardness (>500 HV10) and strength values with YS exceeding 1100 MPa in most cases, except for Steel A, DQP-processed at T_Q 225 °C. Additionally, the uniform (A_g) and total (A) elongations reached about 5–6% and 12–13%, respectively, regardless of the steel type and DQP conditions, Table 9. Of particular interest is the remarkable, all-round improvement in impact toughness properties (KV (–40 °C) and T28J) of TMR-DQP samples, particularly at sub-zero temperatures (< –70 °C).

Table 9. Tensile and impact properties obtained with TMR-DQ and TMR-DQP-processed Steel A and B. Hardness and RA fractions along with their carbon contents are also included in the table (Adapted under CC BY 4.0 license from Publication IV © 2019 Authors).

Material	T_Q [°C]	$R_{p0.2}$ [MPa]	$R_{p1.0}$ [MPa]	R_m [MPa]	A_g [%]	A [%]	KV (−40 °C) [J]	T28J [°C]	HV10	RA [vol.%]	RA [C%]
Steel A, DQ	20	1477 ± 110	1477 ± 110	2086 ± 22	3.7 ± 0.3	8.9 ± 1.1	8	>> 40	627 ± 6	2.6	0.43
Steel A, DQP	175*	1322 ± 65	1691 ± 6	1910 ± 30	4.6 ± 0.1	11.9 ± 0.4	38	-80	545 ± 3	6.3	0.60
Steel A, DQP	225*	1027 ± 134	1443 ± 80	1717 ± 49	5.7 ± 0.7	13.6 ± 0.6	43	-92	505 ± 2	10.1	0.65
Steel B, DQ	20	1475 ± 172	1920 ± 57	2095 ± 22	3.9 ± 0.5	10.2 ± 1.5	11	>> +40	628 ± 5	2.8	0.47
Steel B, DQP	175*	1196 ± 175	1626 ± 14	1871 ± 26	4.5 ± 0.5	11.7 ± 2.5	45	-105	573 ± 2	6.6	0.61
Steel B, DQP	225*	1108 ± 109	1455 ± 75	1659 ± 35	5.1 ± 0.9	13.3 ± 1.1	41	-73	526 ± 2	10.2	0.94

Notes: Tensile properties are averages of three tests. 95% confidence intervals for the means are given. $R_{p0.2}$ is the proof stress at 0.2% offset strain, $R_{p1.0}$ is the proof stress at 1.0 % offset strain, R_m is tensile strength, A_g is plastic component of the uniform elongation, A is plastic component of total elongation, KV (−40°C) is Charpy-V impact energy at −40 °C, T28J is the transition temperature for an impact energy of 28 J, HV10 is Vickers hardness 10 kgf, RA [vol.%] is retained austenite proportion, and RA [C%] is carbon content of retained austenite. *Followed by slow furnace cooling.

In Publication III, the stability of RA, i.e., the reduction of RA content with tensile straining and its mean carbon content at a particular strain, were measured on tensile tested specimens machined from TMR-DQP-processed High-Al and High-Si Steels. The XRD measurements were conducted from three different parts of each tensile tested specimen, i.e., undeformed head, uniformly deformed part and near the fractured end of specimens. Samples quenched at T_Q 225 °C still contained RA in uniformly deformed parts of the sample, contrary to the samples quenched at T_Q 175 °C, indicating more stable RA in samples quenched at higher T_Q 225 °C. In Publication IV, results of the interrupted tensile tests carried out on DQP-processed Steels A and B (coded as High-Al and High-Si Steels, respectively, in Publication III) with T_Q 225 °C were reported illustrating the stability of RA during tensile straining. The results of the XRD measurements carried out on interrupted tensile specimens are shown in Table 10. They were aligned with the values obtained for Publication III, which indicated that large fractions of original RA expectedly transformed during the initial stage of straining, whereas small fractions of fine austenite laths/grains with highest carbon content/s were most stable and remained untransformed even at fracture [90].

Table 10. Fractions of retained austenite along with their carbon contents from the interrupted tensile test samples (Reprinted under CC BY 4.0 license from Publication IV © 2019 Authors).

Steel	RA [vol.%]	RA [C%]
Steel A		
Base	7.5	0.95
2%	4.3	1.14
6%	3.0	1.56
10%	-*	-
Steel B		
Base	8.2	1.04
2%	3.8	1.17
5%	2.3	1.32
9.5%	-*	-

Base means the undeformed heads and 2–10% means percentage elongation of the tensile test specimens. RA (vol.%) means retained austenite proportion, RA (C%) means carbon content of retained austenite. *RA content below the detection limit.

Fig. 13 shows the Charpy V notched impact test results for TMR-DQ and TMR-DQP-processed specimens in the temperature range −120 to 40 °C. DQP treatment considerably increased the impact energy at all temperatures in comparison with

those obtained on DQ-processed samples, which were relatively brittle with low upper shelf energies (USE), and none of the samples could reach the T28J (or T34J/cm^2) transition temperature even at the highest test temperature, i.e., 40 °C, regardless of the steel type or DQP conditions. It was clearly shown that the lath size of the DQP steel variant with the lowest transition temperature was significantly finer than that of the other cases. Most of the retained austenite was finely divided between the laths, which indicated that the short distances between the fine interlath austenite films influenced the transition temperature. It has been conclusively shown that it would be better to have a small volume fraction of RA (~6.5%) divided between fine martensitic laths, rather than a large fraction of RA (~10%) divided between relatively coarser laths. The reason for this requires detailed examination, though it could be tentatively due to thinner RA films being more stable against transformation to martensite during impact testing.

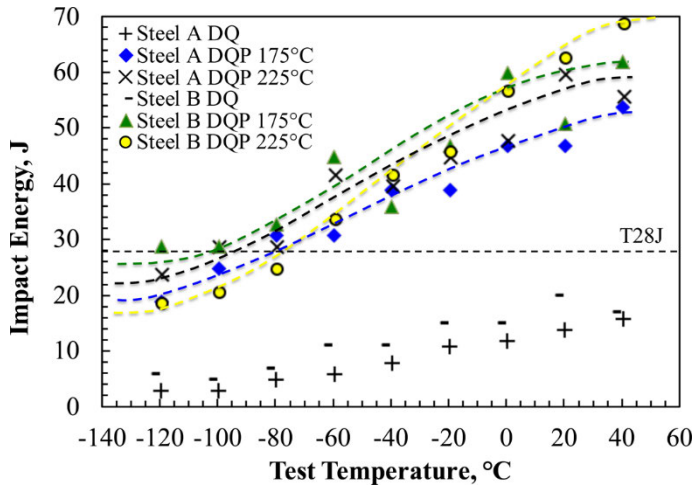

Fig. 13. Variation of impact energy (J) with the test temperature (°C) for TMR-DQ and TMR-DQP-processed samples (Reprinted under CC BY 4.0 license from Publication IV © 2019 Authors).

4.3.5 Impact-abrasive wear performance

According to preliminary impact-abrasion tests, the mass loss of TMR-DQ and TMR-DQP-processed (at T_Q 175 and 225 °C) Steel A (High-Al) and B (High-Si) was mostly dependent on the initial surface hardness. The effect of RA on wear

performance was not clearly discernible. However, the DQ variants exhibited lower mass loss because of the higher initial surface hardness (627 HV10), compared to that of DQP samples (DQP 175 °C: Steel A 535 ± 15, Steel B 565 ± 15; and DQP 225 °C: Steel A 524 ± 15, Steel B 507 ± 15).

4.4 Microstructures and mechanical properties of medium-Mn steels processed via QP as well as ART treatments

Publication VI encompassed the details of the processing routes and their influence on the evolving microstructures as well as the morphology, amount and stability of RA based on Gleeble simulations. Limited tensile property data obtained on the selected laboratory rolled QP- and ART-treated plates are included to understand the efficacy of the two processing routes. Three experimental 0.3C-1Si-0.5Al steels were used in this study: Steel A with contents of Mn 3%, Ni 1%, and Mo 0.2%; Steel B with contents of Mn 4%, Ni 2% and Mo 0.2%; and Steel C with contents of Mn 3%, Ni 1%, and Mo 0.4%, see Table 2.

4.4.1 Initial microstructure and segregation characteristics

For the investigated steels, prior austenite grain reconstruction was carried out for the strained DQ Gleeble samples. Grain sizes were estimated as equivalent circle diameters. The microstructures comprised of both fine as well as coarse grains with the size distribution widely ranging between 10 and 50 μm. The mean PAGS for Steels A, B and C were estimated as 20, 18 and 24 μm, respectively, indicating only minor variation. The fractions of RA in DQ samples were estimated to be moderate to low (2–6%).

EPMA analyses clearly indicated that soaking at 1200 °C for 2 h prior to hot rolling and subsequent reheating at 1150 °C for 4 min during physical simulation experiments on the Gleeble simulator were dismally insufficient for homogenization of the cast structure. The samples for QP and ART processing revealed significant segregation of Mn, Si and Ni in the studied steels, unlike carbon, which was distributed evenly with the possible exception in respect of presence of some carbides. For example, Fig. 14 indicates that Mn varied approximately between 2.5–4.5, 3.5–5.5 and 2.5–4.5% in Steel A, B and C, respectively.

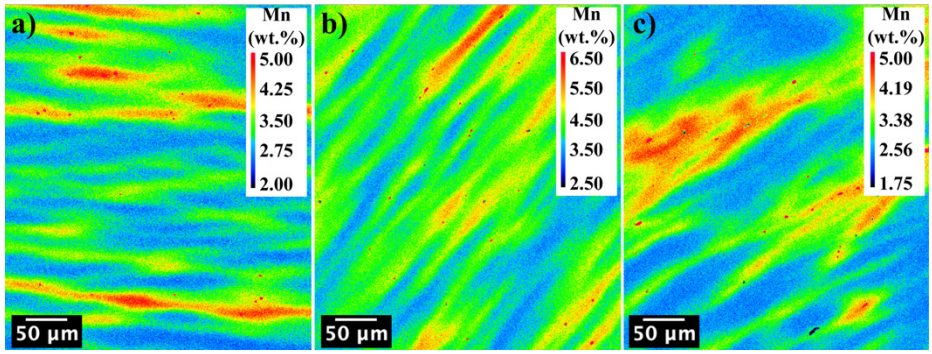

Fig. 14. Variation of Mn content in hot rolled, quenched, and reheated Steel A a), B b) and C c) specimens (Reprinted under CC BY 4.0 license from Publication VI © 2022 Authors).

4.4.2 Determining transformation temperatures

Calculated phase equilibria

Prior determination of the phase transformation temperatures A_{e1} and A_{e3} of steels is necessary for the selection of ART temperatures and annealing times. According to Thermo-Calc calculations, austenite phase becomes stable above 600 °C and the ferrite phase disappears above 780 and 790 °C, respectively, for Steels A and C. In Steel B the austenite transformation begins at a lower temperature of 485 °C and full austenitization can be reached approximately at 730 °C. Accordingly, intercritical A_{e1}–A_{e3} ranges are only 160 and 185 °C, respectively, for Steel A and C, whereas Steel B had a much wider intercritical range of 245 °C. It is to be noted that Mn and C have a significant influence on the stability of austenite, unlike V and Mo alloying elements, which exert a marginal effect.

Transformation during QP

Dilatometric measurements conducted on the Gleeble simulator indicated that the M_s temperatures for Steels A, B and C were about 280, 230 and 285 °C, respectively. A small amount of martensite noticeably started to form somewhat earlier at a marginally higher temperature before the bulk transformation, obviously because of the segregation of Mn, Si and Ni in the steels. Calculations carried out using the JMatPro software gave an estimated difference of as high as 100 °C between the

M_s temperatures of Mn-, Si- and Ni enriched regions and their adjoining areas depleted of these elements.

Fig. 15 shows the variation of the sample diameter with holding time up to 1000 s during partitioning at different T_P in the range 200–500 °C. T_Q for Steels A and B was 100 °C and Steel C 150 °C, corresponding to transformed austenite contents of 17, 22 and 26%, respectively. After reaching the T_P, only a minor gradual expansion (~0.03%) was distinguished during holding for 1000 s at T_P up to 400 °C. It can be considered essentially due to carbon partitioning, though tempering of martensite (contraction) can be offset by the volume increase due to the formation and migration of ledges that allow the martensitic laths to grow into the austenite isothermally (isothermal martensite), which, however, could not be identified despite extensive TEM study, as described later. Nonetheless, bainite transformation that can result in an appreciable expansion was evidently mitigated here during partitioning for 1000 s, except in the case of Steel A at T_P 500 °C, where a small fraction of bainite seemed to have formed starting at about t_P = 40 s, resulting in approximately 0.07% expansion during holding.

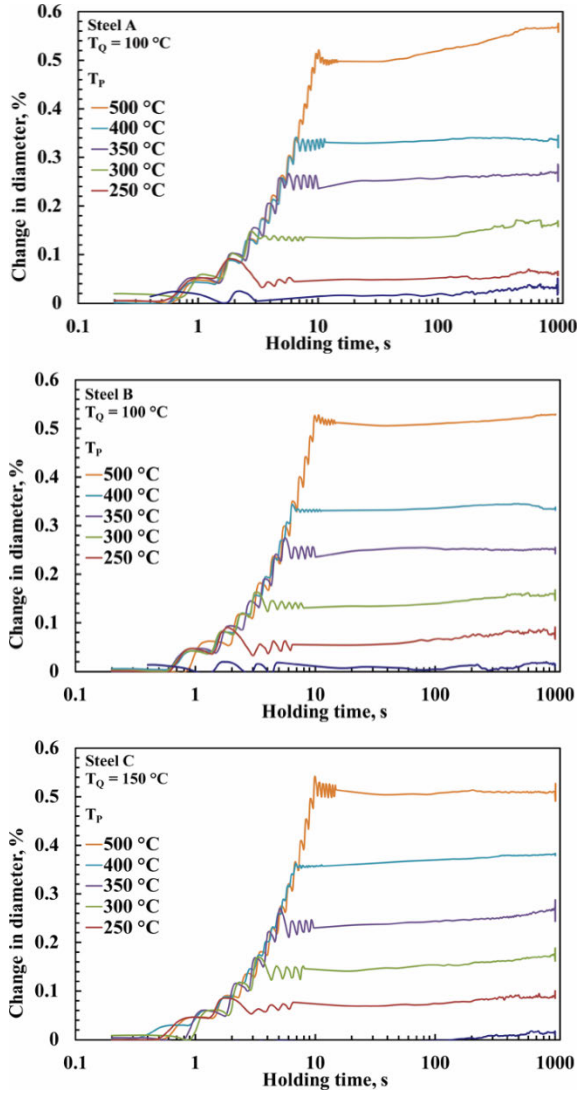

Fig. 15. Variation of specimen diameter with partitioning time (holding time) at different partitioning temperatures (T_P). Quenching temperatures (T_Q) for Steel A and B was 100 °C and Steel C 150 °C (Adapted under CC BY 4.0 license from Publication VI © 2022 Authors).

Only small fractions of high carbon untempered FM formed after the partitioning stage during final quenching to RT, as illustrated by the change in the slopes of

dilatation curves during the final stage of cooling in Fig. 16. The most significant change in the slope was discerned for Steel C, partitioned at 200 °C.

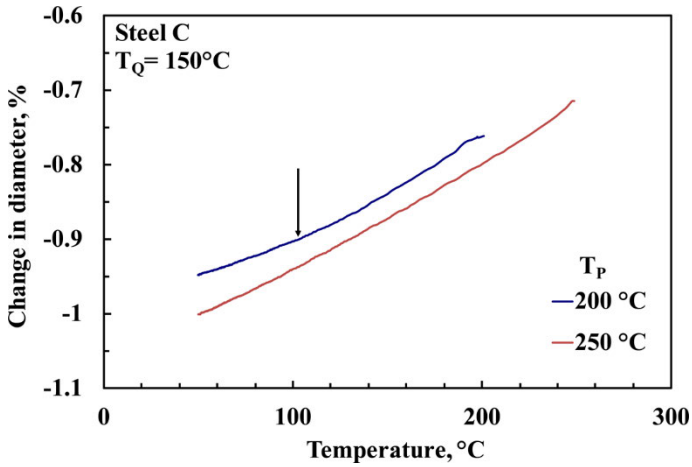

Fig. 16. Formation of fresh martensite during final cooling after partitioning. The arrow marking the inflexion in the cooling curve for partitioning temperature (T_P) = 200 °C shows the start of untempered martensite formation (Reprinted under CC BY 4.0 license from Publication VI © 2022 Authors).

For QP samples, the fractions of RA along with their average carbon contents were determined using XRD. After partitioning for 1000 s at different partitioning temperatures in the range 200–400 °C, the RA fractions in Steel A remained nearly constant at about 10% but increased gradually from 13 to 26% in Steel B, and from 7 to 17% in Steel C, as shown in Fig. 17. In the case of partitioning at T_P 500 °C, the RA fraction dropped approximately to same level as RA fractions of DQ samples, but the carbon content of RA was higher for samples partitioned at TP 500 °C. The RA fractions along with their carbon contents for DQ Steels A, B and C were: 3% and 0.65% C; 6% and 0.59% C; and 2% and 0.49% C, respectively.

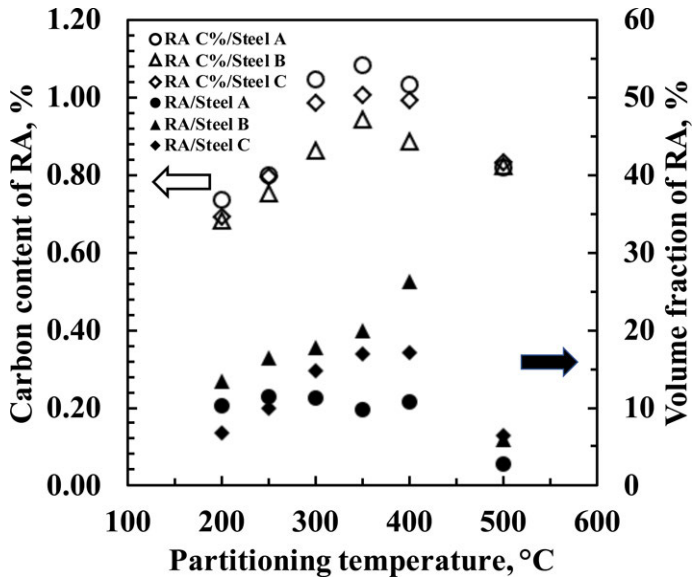

Fig. 17. The fractions of retained austenite along with their average carbon contents for QP specimens (Reprinted under CC BY 4.0 license from Publication VI © 2022 Authors).

Transformation during ART

To discern the possible FM formation and corresponding start temperatures of bulk transformation (FM_S) following ART processing, simulation tests were carried out in Gleeble to record the dilatation data, particularly during the final cooling to RT. Table 11 lists the FM_S temperatures after ART treatments with different t_R times at varied T_R temperatures. Also included in Table 11 are the fractions of RA along with their average carbon contents. Overall, the FM phase constituents at RT seem to increase with increasing ART temperature and time, affirming the decreasing thermal stability of austenite. On the other hand, RA fraction increases with increasing T_R up to a certain point (~660 °C on Steel B), beyond which it drops steeply. This drop is obviously due to a higher fraction of austenite to start with that undergoes relatively low enrichment with C and Mn, and hence a considerable fraction of this austenite transforms to FM during final cooling to RT due to lower stability. At low T_R temperatures with prolonged t_R times, increased fractions of RA are realized, in consistence with earlier observation on medium-Mn steels [91]. In Steel B, at the lowest T_R, the carbon content of RA increased with increasing t_R, most likely due to dissolution of carbides.

Table 11. The FM_S temperatures and RA fractions along with their average carbon contents (Reprinted under CC BY 4.0 license from Publication VI © 2022 Authors).

Time	Steel A				Steel B				Steel C			
t_R	T_R	RA	RAC	FM_S	T_R	RA	RAC	FM_S	T_R	RA	RAC	FM_S
[s]	[°C]	[vol.%]	[wt.%]	[°C]	[°C]	[vol.%]	[wt.%]	[°C]	[°C]	[vol.%]	[wt.%]	[°C]
100	710	18	0.38	160	630	13	0.35	-	690	26	0.62	-
1000	710	22	0.46	130	630	25	0.49	-	690	18	0.66	-
5000	710	11	0.40	160	630	27	0.53	-	690	26	0.45	90
100	730	7	0.41	220	660	27	0.55	-	710	17	0.40	120
1000	730	9	0.33	220	660	36	0.56	-	710	12	0.44	100
5000	730	5	0.36	220	660	49	0.55	-	710	24	0.63	110
100	750	9	0.39	240	690	18	0.35	90	730	6	0.40	200
1000	750	4	0.34	260	690	7	0.48	160	730	10	0.44	210
5000	750	5	0.32	280	690	13	0.32	150	730	9	0.38	200
100	770	5	0.34	270	710	12	0.32	200	750	6	0.31	260
1000	770	6	0.36	280	710	11	0.34	200	750	5	0.38	240
5000	770	4	0.32	280	710	9	0.32	200	750	5	0.40	250

4.4.3 Microstructural features

In addition to the RA fractions, as communicated in previous chapters, various microstructural features of the QP- and ART-treated steels were examined utilizing the LSCM, SEM, EBSD and TEM techniques.

The LSCM images of Gleeble simulated QP-processed samples revealed that the overall microstructures comprised primarily of martensitic laths for the investigated steels A, B and C, as shown in Fig. 18a, Fig. 18c and Fig. 18e, respectively. Corresponding microstructures consisted primarily of tempered martensitic ferrite with lath-like features and some blocky islands of FM/RA (MA) as observed by FESEM microscopy and shown in Fig. 18b, Fig. 18d and Fig. 18f, respectively. Presence of fine interlath films or pools of RA, if any, could not be detected from these micrographs. The largest MA regions had blocky appearance and despite the Al and Si alloying, structures revealed the occurrence of precipitation, as seen in Fig. 18b, Fig. 18d and Fig. 18f. These precipitates are most probably transition carbides [38].

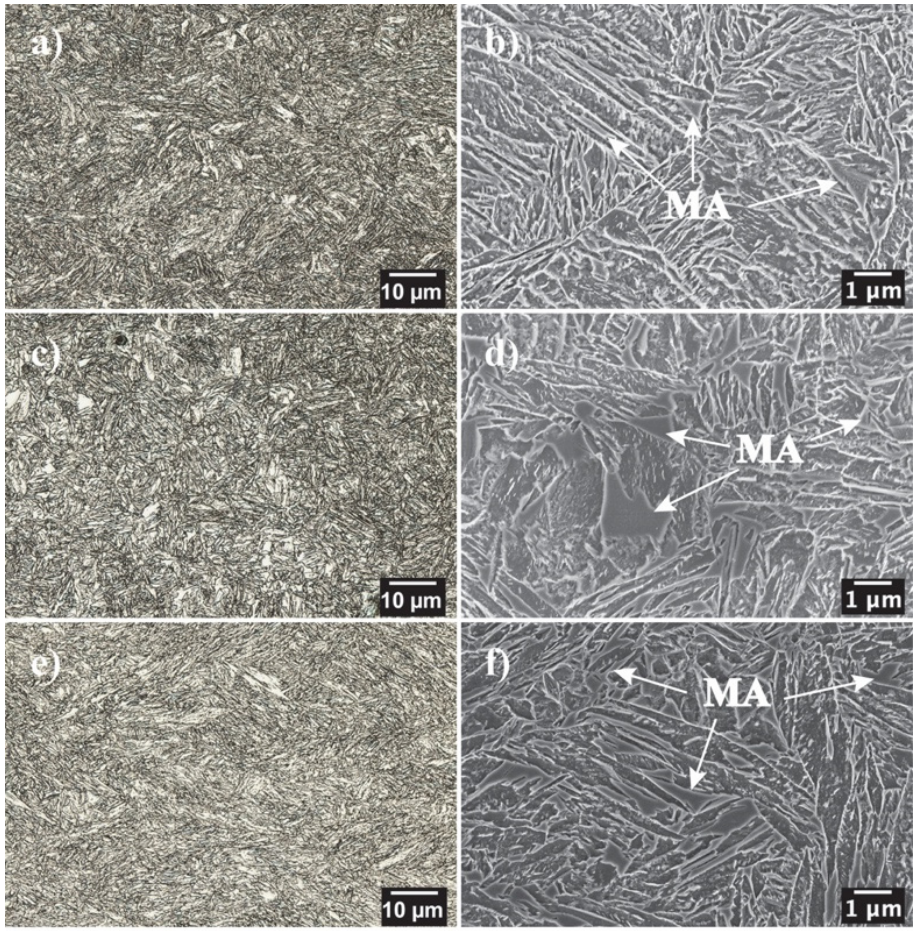

Fig. 18. LSCM a), c), e) and SEM b), d), f) micrographs of QP-treated samples. Steel A processed at T_Q 100 °C, T_P 300 °C and t_P 1000 s a) and b); Steel B processed at T_Q 100 °C, T_P 350 °C and t_P 1000 s c) and d); Steel C processed at T_Q 150 °C, T_P 400 °C and t_P 1000 s e) and f) (Reprinted under CC BY 4.0 license from Publication VI © 2022 Authors).

The ART-treated Gleeble samples exhibited notably different microstructural features in comparison with corresponding QP samples. The austenitic areas were discernible as more elongated (lath-shaped) when compared to the blocky MA islands seen in the QP samples, as shown in Fig. 19. The LSCM images of ART-processed steels A, B and C exhibited generally martensitic lath structure for the investigated steels, as shown in Fig. 19a, Fig. 19c and Fig. 19f, respectively. Subsequent SEM and EBSD analyses confirmed that the uniform darker and

slightly deeper areas corresponded to ferrite (F), whereas somewhat rough, heterogeneous areas were martensite and/or RA, as depicted in Fig. 19b, Fig. 19d and Fig. 19f, respectively. SEM microstructures recorded on Steels A and C and shown here in Fig. 19b and Fig. 19f, respectively, depicted features comprising mainly of FM with some RA and F, whereas the SEM microstructure recorded on Steel B and shown here in Fig. 19d displayed features mainly consisting of TM along with some fine F, RA as well as some carbides.

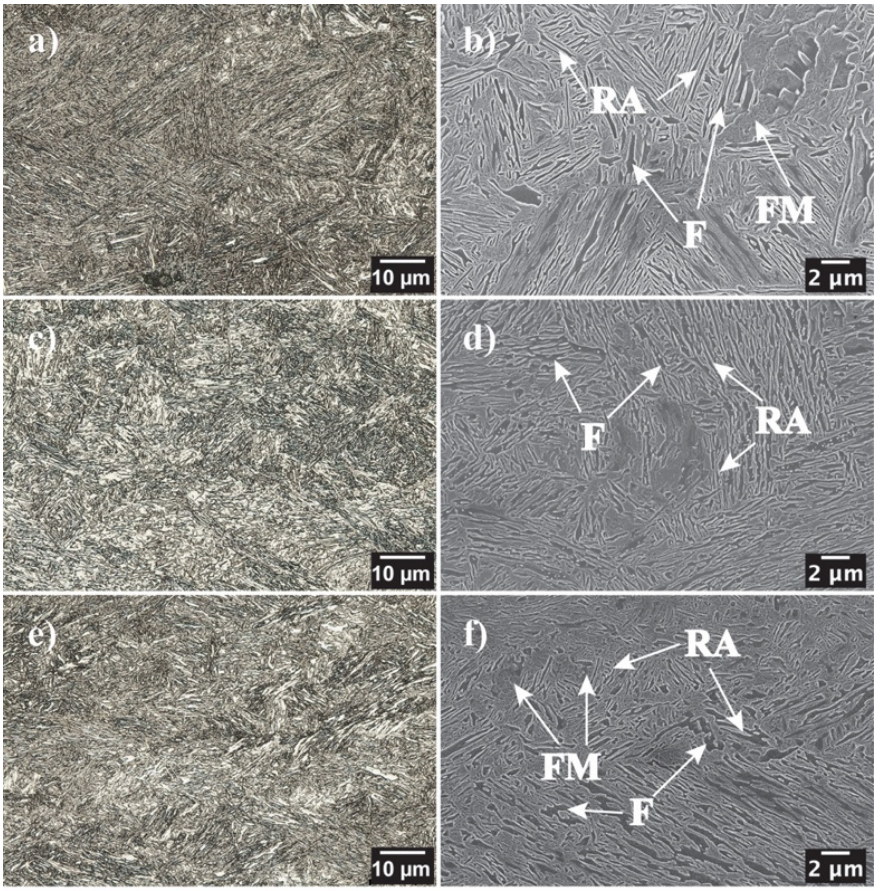

Fig. 19. LSCM a), c), e) and SEM b), d), f) micrographs of ART-treated samples. Steel A processed at T_Q 710 °C and t_R 1000 s a) and b); Steel B processed at T_R 660 °C and t_R 5000 s c) and d); Steel C processed at T_R 710 °C and t_R 5000 s e) and f) (Reprinted under CC BY 4.0 license from Publication VI © 2022 Authors).

The morphology of RA was also investigated by EBSD. Examples of EBSD image quality (IQ) maps superimposed with phase maps are shown in Fig. 20a and Fig. 20b for QP-treated and ART-treated Steel A specimens, respectively. A general comparison of QP- and ART-treated samples indicates that in the case of QP microstructures, RA appears mainly in the form of pools/blocky shapes, whereas in the case of ART microstructures, it is present mainly as interlath films, though some pools can also be seen. Due to the limits of resolution (0.08 μm), presence of fine interlath films of austenite, if any, in QP structure cannot be distinguished by EBSD measurements.

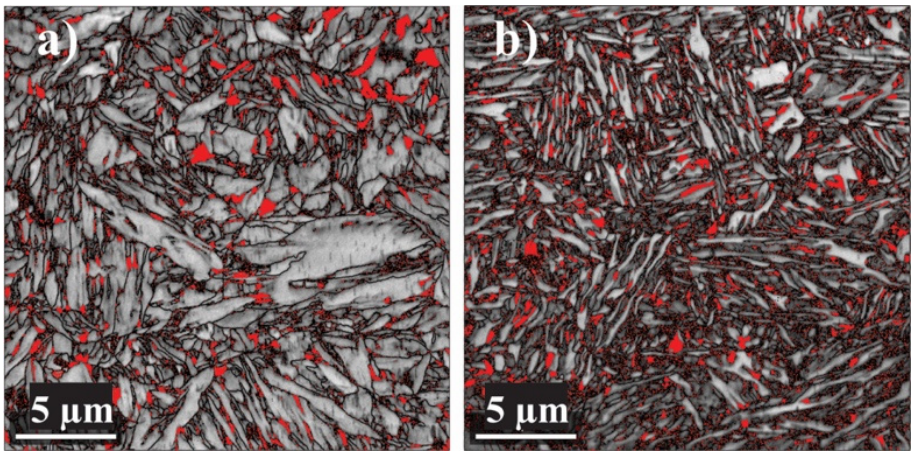

Fig. 20. EBSD measurements showing a) blocky RA in QP-processed (T_Q = 100 °C, T_P = 350 °C and t_P = 1000 s) and b) fine interlath RA in ART processed (T_R = 710°C and t_R = 1000 S) Steel A samples. The different morphology of RA is showing in red color (Reprinted under CC BY 4.0 license from Publication VI © 2022 Authors).

To further study the qualitative details of fine lath structures as well as the morphology, size ranges and locations of RA, TEM examinations were conducted utilizing both the BF and DF imaging. Fig. 21 shows an example of microstructure recorded on QP sample of Steel B containing ~20% RA. The presence of austenite phase was identified by indexing relevant diffraction patterns. Fig. 21a and Fig. 21b showing BF and DF images, respectively, reveal the presence of interlath austenite films (light colored), suggesting that the QP samples did contain film-like RA laths also, and not just the tiny pools, as distinguished in EBSD measurements (Fig. 20).

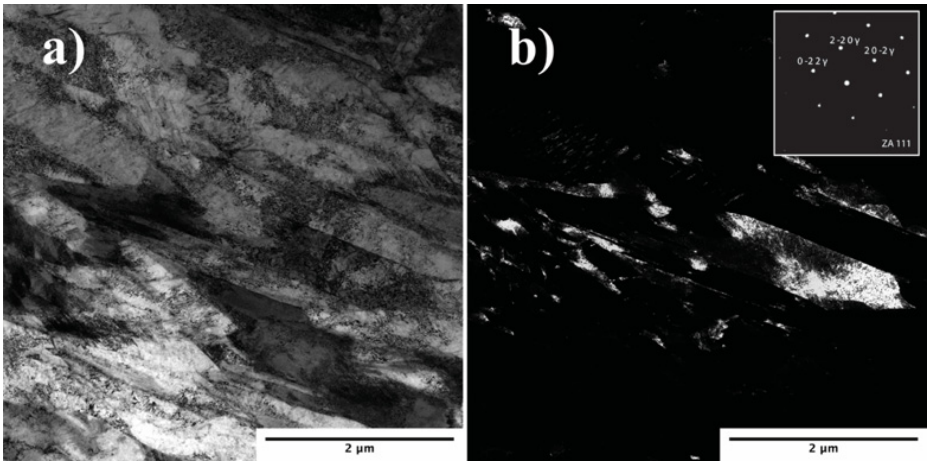

Fig. 21. TEM micrograph recorded on Steel B QP sample treated at T_Q 100 °C, T_P 350 °C and t_P 1000 s: a) BF image showing lath martensite with interlath austenite and b) corresponding DF image revealing the interlath austenite. Inset: SAED pattern showing spots for austenite with <111> zone axis (Reprinted under CC BY 4.0 license from Publication VI © 2022 Authors).

Fig. 22a presents an example of BF image from lath martensite observed in an ART-processed Steel C sample and Fig. 22b depicts corresponding DF image showing the presence of interlath RA. The lath-shaped ferrite, inherited from annealed martensite, presumably forms the part of the image, but it is difficult to discern.

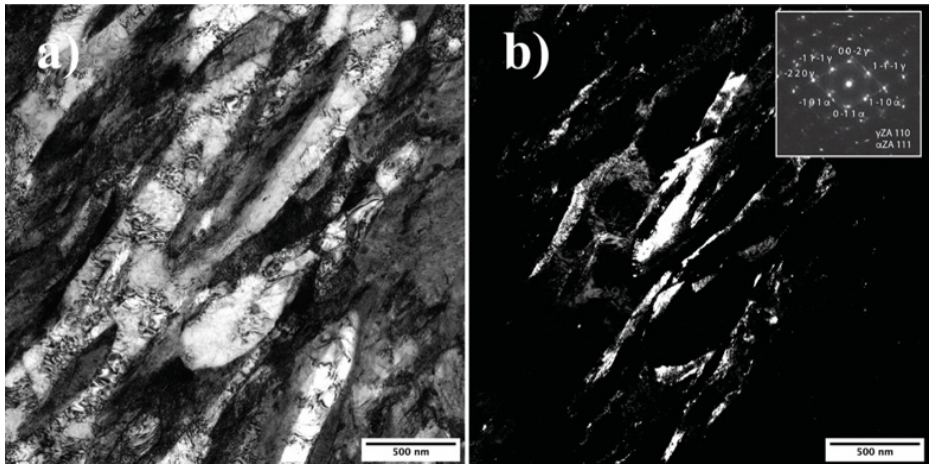

Fig. 22. TEM micrograph recorded on Steel C ART sample treated at T_R 710 °C and t_R 5000 s: a) BF image showing lath martensite with interlath austenite and b) corresponding DF image showing interlath austenite Inset: overlapping SAED patterns showing spots for austenite with <110> and ferrite with <111> zone axis (Reprinted under CC BY 4.0 license from Publication VI © 2022 Authors).

4.4.4 Hardness

The effect of T_P temperature on the hardness of QP-treated Gleeble samples of the three steels, all held isothermally at specific T_P temperatures for 1000 s, is presented in Table 12. Also included in the table are the hardness measurement results obtained on the corresponding DQ specimens. The hardness data of QP specimens expressed a monotonic softening with the increase in T_P temperature up to 500 °C.

Table 12. The mean* Vickers hardness values of the QP-processed Gleeble samples (Adapted under CC BY 4.0 license from Publication VI © 2022 Authors).

Partitioning		Steel A	Steel B	Steel C
T_P [°C]	t_P [s]	HV10	HV10	HV10
200	1000	559 ± 9	538 ± 10	571 ± 14
250	1000	518 ± 11	513 ± 3	508 ± 9
300	1000	512 ± 8	495 ± 11	493 ± 7
350	1000	508 ± 7	486 ± 5	490 ± 9
400	1000	481 ± 12	456 ± 5	486 ± 8
500	1000	403 ± 12	429 ± 11	452 ± 12
DQ	-	594 ± 12	573 ± 23	582 ± 12

*Average of 5 readings

Table 13 presents the extent of scatter noticed in the hardness values of ART-processed Gleeble samples, indicating the complexity of phase mixtures encountered with a particular reversion treatment, i.e., FM, TM, ferrite and RA. Evidently, the ART accomplished at highest T_R temperatures promote the formation of considerable fractions of hard FM.

Table 13. The mean* Vickers hardness values of the ART-processed Gleeble samples (Reprinted under CC BY 4.0 license from Publication VI © 2022 Authors).

Steel A			Steel B			Steel C		
T_R [°C]	t_R [s]	HV10	T_R [°C]	t_R [s]	HV10	T_R [°C]	t_R [s]	HV10
710	100	526 ± 24	630	100	568 ± 35	690	100	421 ± 0
710	1000	477 ± 15	630	1000	361 ± 10	690	1000	404 ± 15
710	5000	504 ± 41	630	5000	340 ± 8	690	5000	407 ± 27
730	100	591 ± 13	660	100	383 ± 0	710	100	500 ± 19
730	1000	576 ± 10	660	1000	361 ± 13	710	1000	529 ± 14
730	5000	576 ± 10	660	5000	332 ± 7	710	5000	464 ± 21
750	100	601 ± 16	690	100	538 ± 15	730	100	577 ± 12
750	1000	598 ± 12	690	1000	551 ± 8	730	1000	557 ± 14
750	5000	587 ± 15	690	5000	551 ± 40	730	5000	542 ± 15
770	100	608 ± 6	710	100	581 ± 12	750	100	606 ± 8
770	1000	584 ± 12	710	1000	598 ± 12	750	1000	584 ± 18
770	5000	577 ± 8	710	5000	578 ± 19	750	5000	566 ± 13

*Average of 5 readings

4.4.5 Tensile properties

To understand the effect of QP and ART treatments on the tensile properties of the investigated steels, laboratory scale TMR-QP and TMR-ART trials were conducted. These TMR trials were based on the conditions relevant to achieve the targeted UTS (~1500 MPa), roughly estimated based on the hardness around 500 HV of the related Gleeble simulated specimens. The corresponding QP and ART processing parameters and accomplished average YS, UTS, uniform elongation (UEL), TEL and UTS x TEL on tensile test specimens are listed in Table 14. The corresponding RA fractions are also included in Table 14. As expected from the higher hardness, the QP-treated specimens showed moderately higher YS and UTS compared to ART-processed ones, but somewhat lower UEL and TEL. It is to be noted that the UTS of ART-processed Steels A and B did not meet the targeted level, Table 14.

Table 14. Tensile properties obtained with TMR-QP and TMR-ART laboratory hot rolled steels (Adapted under CC BY 4.0 license from Publication VI © 2022 Authors).

Material & processing condition	YS (MPa)	UTS (MPa)	UEL (%)	TEL (%)	UTS*TEL (MPa%)	RA (wt.%)
Steel A-QP (T_Q=100 °C T_P=400 °C t_P=1000 s)	1450	1760	2	9	15840	6
Steel B-QP (T_Q=100 °C=T_P 350 °C t_P=1000 s)	1360	1690	5	14	23660	16
Steel C-QP (T_Q=150 °C T_P=400 °C t_P=1000 s)	1020	1530	8	13	19890	15
Steel A-ART (T_R=710 °C t_R=1000 s)	600	1230	15	20	24600	33
Steel B-ART (T_R=630 °C t_R=1000 s)	1050	1200	9	18	21600	11
Steel C-ART (T_R=710 °C t_R=5000 s)	690	1630	11	13	21190	28

5 Discussion

This chapter presents a comprehensive discussion on the results presented in Publications I–VI. In the light of various aspects of the two main processing routes used in this study, i.e., QP/DQP (medium-C steels), and QP and ART (medium-Mn steels) processing, the discussion essentially focuses on evolved microstructures, austenite decomposition during thermomechanical processing, RA fractions and stability, mechanical properties, and structure-property correlations, considering both the Gleeble and laboratory rolled simulations. Additionally, the wear-resistance of TMR-DQP samples in comparison with their DQ counterparts has also been discussed.

5.1 Microstructure

In the QP processes, besides carbon partitioning, decomposition of austenite into bainite, and isothermal martensite can occur, besides the formation of a small fraction of high carbon, untempered martensite (FM) during the final cooling to RT. QP steels, containing 0.3 wt.% C alongside additions of Si and Al, when quenched and partitioned for 1000 s without prior deformation, revealed features typical of TM along with RA, bainite and high carbon FM formed during final cooling to RT. For a short holding time (t_P = 10 s), the microstructures consisted of relatively higher fractions (about 8–10%) of FM. Prior straining in the matrix did show similar features but resulted in the refinement of transformed microstructure via recrystallization with randomization of martensite packets, blocks, and laths in different orientations. High silicon and/or aluminum contents could not completely inhibit the formation of transition carbides within primary martensite block structures. These carbides were observed even in corresponding DQ samples. This suggests that these precipitates formed as a result of martensite auto-tempering [81]. Furthermore, the microstructures of TMR-DQP High-Al and High-Si steel samples revealed the occurrence of carbide precipitation, besides similar formation of carbides in QP-processed medium-Mn steels. These precipitates were probably transition ε-carbides. Si has a high solubility in ε-carbide and may facilitate its formation, whereas it has a lower solubility in cementite and can delay its formation [38]. Carbide precipitations were more conspicuous with the higher T_Q.

TEM examinations of both unstrained and strained QP samples clearly revealed the presence of i) fine films of interlath austenite and micrometer-scale pools of RA, ii) untempered, in some cases, twinned, high carbon martensite,

formed from the carbon-enriched metastable austenite during final cooling to RT, and iii) lower bainite that formed during isothermal holding, often below the M_s temperature (Fig. 23). Though not very clear, the TEM micrograph in Fig. 23b also shows the presence of wavy boundaries (shown by arrows) i.e., the ledged growth of martensitic lath, confirming the isothermal martensite formation [23], [47].

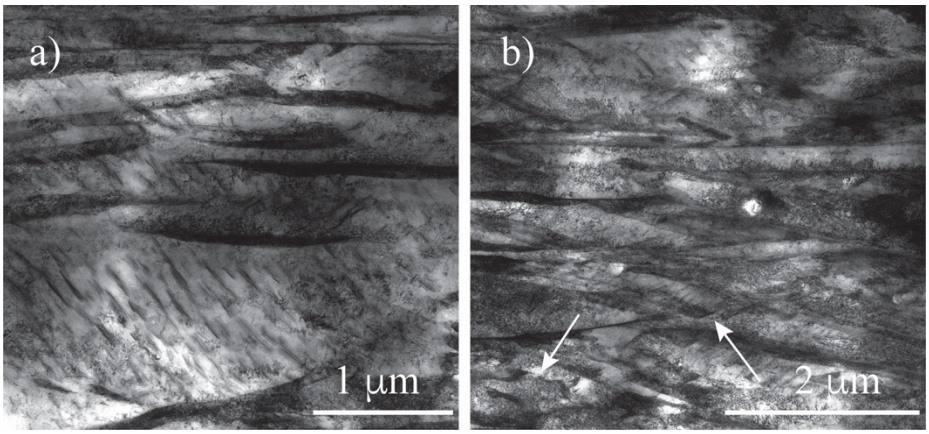

Fig. 23. TEM micrograph recorded on unstrained Steel A QP sample treated at T_Q 200 °C, T_P 300 °C and t_P 1000 s: a) showing lower bainite, and b) martensite with wavy lath boundaries (Reprinted under CC BY-NC-ND 4.0 license from Publication I © 2020 Authors).

For strained QP samples, the reconstructed prior austenite grain structures unexpectedly showed partial recrystallization with the presence of both fine and coarse randomly oriented grains, even though the deformation temperature was low at 800 °C. Additionally, in TMR-DQP processing seemingly partial recrystallization occurred during laboratory hot rolling with FRT at 820 °C, resulting in low aspect ratio at 1.26–1.50, suggesting that the pancaking was not adequate.

In the course of partitioning during the QP process, some micro-scale austenite pools transformed to lower bainite due to lower stability, which explains the increase in the rate of bainite formation [92]. The time required for the initiation of bainite formation decreased as the T_P was increased. Normally, prior deformation of austenite in the T_{NR} regime enhances the bainite formation in microalloyed DQ steels [93]. In this study, in the case of 0.3C (high) silicon-aluminum steels, prior deformation close to T_{NR}, however, did not accelerate formation of bainite, and one

reason could be inadequate pancaking and the occurrence of partial recrystallization leading to the formation of fine grains between the pancaked grains (loss of dislocation density). During isothermal holding during partitioning, the C-curve can also be at a temperature below T_P, but bainite transformation can still occur during final cooling to RT. Furthermore, martensite transformation was apparent during the final cooling for both strained and unstrained specimens, but with highest T_P, the martensite transformation temperature decreased in both cases, regardless of the investigated steel type. Deformation in the T_{NR} regime can slightly accelerate tempering of martensite during partitioning especially at the highest T_P. This can be due to the partial recrystallization seen in the strained samples leading to formation of some fine grains with somewhat lower dislocation density. The decreasing of grain size due to partial recrystallization can, therefore, indirectly increase the fraction of TM [94].

For the TMR-DQP-processed steels, the PAGS and d were approximately in the same range, except for High-Si steel at T_Q 175 °C, which displayed a clearly lower d value as shown in Table 8.

The QP and ART treatments were employed for three 0.3C-1Si-0.5Al medium-Mn steels. Additionally, these steels contained 3Mn-1Ni-0.2Mo (Steel A), 4Mn-2Ni-0.2Mo (Steel B) and 3Mn-1Ni-0.4Mo (Steel C). The aim was to have leaner Mn alloying than generally used in medium-Mn steels (reported as high as 10–12% Mn). Conventionally, it has been considered that a high fraction of RA in the steel with relatively low stability can have favorable characteristics for TRIP-enhanced mechanical properties [91]. A wide range of RA fractions (3–49%) was achieved in medium-Mn steels following the QP and ART processing, with varying morphology, size, and carbon contents of the RA. The QP structures consisted primarily of tempered martensitic ferrite with lath-like features and some blocky islands of MA. For the ART-processed samples, austenitic areas were more elongated and lath-shaped, and ferritic area were depleted of carbon and Mn. In the QP structures, RA appeared mainly in the form of pools/blocky shapes, whereas in ART structures, it was mainly present as interlath films, though some pools could also be seen.

5.1.1 Retained austenite

For excellent ductility in tensile tests, RA fractions on the order of 20% and above with moderate to high stability is often desired to enable enhanced TRIP ductility. In general, an ultrafine-sized lath-like austenite is more stable against strain-

induced transformation than relatively coarser (sub-micron or micron-size) austenite [65]. Large RA pools and/or islands can quickly transform to martensite, even at low strains, thereby leading to lower values of UEL, unlike in the case of small, ultrafine RA.

Significant grain refinement can marginally decrease the M_s temperature, which in turn can affect the RA fraction. In this context, it has been observed that M_s was shifted to lower values, as the PAGS decreased from 67 to 6 μm [94]. Strained samples, which showed partially recrystallized structures, exhibited approximately 10 °C lower M_s temperatures compared to unstrained samples.

In the QP process, an increase of T_Q (from 200 to 260 °C) or T_P (from 200 to 400 °C) generally resulted in a higher fraction of RA. Increasing the t_P first led to an increase in the RA fractions, both for the unstrained and strained conditions, with a maximum value of austenite realized at about t_P 100 s, beyond which the RA fraction dropped again at t_P 1000 s obviously as a consequence of greater carbide formation and austenite decomposition. For Steel C (Al-Si) fraction of RA remained lower compared to those of Steel A (High-Al) and Steel B (High-Si). Lower RA fractions of Steel C (Al-Si) can be due to the low amount of silicon alloying (0.48 wt.%) and also the formation of many coarse inclusions such as AlN, AlO, AlMgO and AlN, which can not only be detrimental to tensile ductility, but can also deteriorate the ability of reduced Al in solution to impede the carbide formation [95]. Hence, the effectiveness of Al may not be adequate in stabilizing the austenite during the partitioning process and the resulting fraction of RA would be somewhat lower. In Steel A (High-Al), the content of coarse inclusions was lower, most probably due to relatively lower N-content (0.0010%) compared to that of Steel C (0.0030 %). N-content of Steel B (High-Si) was 0.0031%, but it did not contain any Al, and hence the number of coarse inclusions was lower, similarly as in Steel C (Si-Al).

Prior straining of samples before the QP treatment facilitates refinement of not only the martensitic packets, blocks and laths, but also the lath-like films and small pools of RA. The refining of austenite in the strained samples imparted relatively larger interface areas and, hence, shorter carbon diffusion distances, which resulted in more stable RA, compared to what is seen in the case of unstrained samples [96]. Irrespective of QP steel type, the strained specimens reached high RA fractions compared to corresponding unstrained samples, see Table 6 and Table 7.

RA fractions obtained in TMR-DQP-treated medium carbon High-Al and High-Si steels, were approximately 6 and 10% after DQP processing at T_Q 175 and 225 °C, respectively. Even though Al should be marginally less effective in

retarding the formation of transition carbides than Si, the corresponding RA levels were nearly same [40], [97]. This was presumably due to the higher combined contents of Al and Si (1.66%) in High-Al steel compared to the Si content (0.99%) of High-Si steel. Carbon concentration in the RA also increased with increasing T_Q from 175 to 225 °C due to enhanced diffusion. In contrast, the C-content of austenite should decrease with increasing T_Q, according to the CPE model [48]. At the T_Q 175 °C, a higher martensite fraction holds more supersaturated carbon due to the lower fraction of untransformed austenite, but the diffusion rate was probably too low to equilibrate and enrich a high carbon content in the austenite.

After DQP processing, microstructures contained thin films of interlath austenite, besides RA pools. EBSD scans (step size 40 nm) indicated volume fraction of RA only about 0.6–0.8% for TMR-DQP-processed steels at T_Q 225 °C. These RA levels are substantially lower compared to those determined by XRD, i.e., volume fraction ~10%, suggesting that over 90% of the RA was finely divided as films between the martensite laths because XRD measurements are far more accurate compared to the EBSD measurements, which are affected by the resolution limit (about 0.08 μm) of the technique. On the other hand, the blocky-type RA could generally have lower mechanical stability in comparison to that of film-type morphology [98]. It can mean that a part of RA pools was not stable enough to resist phase transformation during sample preparation for EBSD and, therefore, can partly explain reduced fraction of RA, mainly as pools.

Generally, in the QP processing, relatively lower fractions of RA than predicted are achieved assuming full transfer of carbon from the martensite at a given T_Q [53]. For QP-processed medium-Mn steels, maximum RA was achieved at high T_P 400 °C and at a fixed t_P of 1000 s. For the studied medium-Mn steels, the corresponding maximum C content of RA varied in a narrow range 0.94–1.08% at T_P 350 °C, as shown in Fig. 17.

The carbon content determination of RA was carried out using XRD measurements and were estimated for medium-Mn steels based on the austenite lattice parameter using Equations 1 and 2. XRD measurements provided average results based on the carbon contents of approximately 1–3 mm^2 areas on sample surface layers. The deviation of carbon content in RA at micrometer-scale cannot be verified by XRD, and, therefore, the stability of RA can vary considerably in pools and interlath films as well as from one location to another. This is an important consideration with medium-Mn steels which are strongly segregated.

In the ART process, the T_R temperatures of medium-Mn Steel B were selected in the temperature range, where maximum RA was achieved. The fraction of RA

increased significantly with increasing T_R from 630 to 660 °C until it decreased at still higher temperatures. This is in agreement with previous studies [62], [91]. The RA increased with the holding duration at T_R 630 and 660 °C, whereas the RA fractions decreased with increasing t_R at higher T_R as shown in Fig. 24. Furthermore, from Table 11 and Fig. 24, it is evident that the equilibrium austenite level was reached within 5000 s at T_R 660 °C and practically all the austenite was retained at RT. A longer t_R might result in reduced RA fraction due to the lowering of austenite stability because of grain growth and result in the formation of FM during final cooling. At the T_R 630 °C, the RA fraction of 27% was achieved within t_R 5000 s which approximately corresponded to the equilibrium austenite fraction in Fig. 25. This was possibly a result of the accelerated diffusion in the martensitic laths and fine division of austenite which shortened the diffusion distances [62], [99].

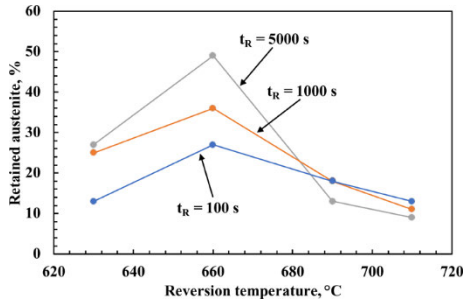

Fig. 24. RA as a function of T_R at different t_R for ART-processed Steel B (Reprinted under CC BY 4.0 license from Publication VI © 2022 Authors).

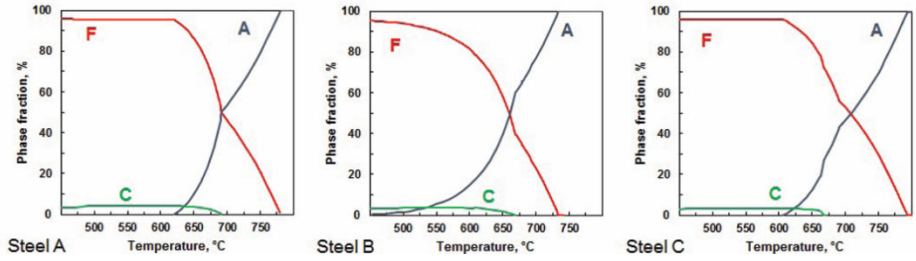

Fig. 25. Equilibrium fractions of austenite (A), ferrite (F) and cementite(C) calculated for Steels A, B and C utilizing the Thermo-Calc software B (Reprinted under CC BY 4.0 license from Publication VI © 2022 Authors).

An examination of medium-Mn Steel B showed that alloying with high Mn and Ni was beneficial in stabilizing a high fraction of RA. At T_R 710 °C, Steel B exhibited lower RA fractions compared to those of Steels A and C. Steel B had pronounced formation of FM during final cooling due to low stability of the high RA fractions. According to equilibrium calculations, in Steel B a 50% austenite fraction was obtained at T_R ~40 °C, lower than that in Steel A and C. This resulted from higher Mn and Ni contents in Steel B and the addition of Mo and V in Steel C.

Both the EBSD and XRD techniques were utilized to determine RA fractions of the QP as well as ART-processed medium-Mn steels. While XRD techniques can be used for measurements of bulk RA fractions, regardless of the size, the EBSD method is limited by its resolution (0.08 μm) that precludes detection of finest RA, mostly as films. Areas of about 485 μm^2 were examined for each specimen by the EBSD technique in the present work. Therefore, the possible differences in the size and morphology of RA grains for these specimens can be indirectly revealed by comparing the RA fractions estimated using the EBSD and XRD measurements.

The RA fractions from EBSD and XRD measurements are close to each other for the QP-processed medium-Mn Steels A, B and C, as listed in Table 15. Thus, it can be suggested that most of the RA in QP-processed steels are in the form of pools, alongside some elongated, lath-shaped grains. Presence of some very fine, interlath RA films could be detected by TEM microscopy. Contrarily, in the case of TMR-DQP-processed High-Al and High-Si steels, most of the RA was identified as finely divided, interlath films between martensite laths. Presumably, as a result of Mn segregation in medium-Mn steels, a fraction of austenite grains in Mn-enriched areas remained untransformed following quenching to T_Q and produced the blocky-shaped morphology of RA [6].

For the ART-processed samples of medium-Mn Steels A and C, the EBSD analyses revealed RA fractions lower than those determined by the XRD measurements (Table 15). From these results, it can be interpreted that there was a significant amount of ultrafine austenite, not detectable due to the resolution limit of the EBSD technique. The ART treatment at a high T_R 710 °C led to austenite growth with globular morphology along the intergranular region and correspondingly the average Mn concentration in austenite decreased [55], [100]. RA grains inside ferrite grains and between martensite laths (acicular, lath-like austenite) have a higher stability compared to the ones at ferrite grain boundaries [101]. During quenching, blocky, or globular austenite transforms to FM, and the RA is stabilized mostly in the form of fine interlath films.

Its seems that in QP-treated medium-Mn steels it was difficult to avoid blocky-shaped RA [102], [103]. To circumvent it, cryogenic tempering in QP process has been developed to produce higher fractions of film-like RA to impart better properties [102]. From Table 15, it can clearly be perceived that the differences in RA fractions estimated using EBSD and XRD equipment are appreciable for the ART specimens, contrary to their QP-processed counterparts. This suggests that for ART-treated samples, considerable RA fractions existed as finely divided interlath films (~ 11, 11 and 19% for Steels A, B and C, respectively) that were undetectable due to the resolution limit of EBSD measurements. Both austenite and ferrite laths remained reasonably narrow (200–300 nm), possibly due to the slow diffusion rate of Mn in austenite [104], thus suggesting the high stability of RA. In the TEM study, a separate selected area electron diffraction (SAED) pattern could not be recorded on austenite grains of the ART-processed sample to be able to distinguish it from the SAED pattern of ferrite. Instead, concurrent diffraction patterns of austenite and ferrite phases were observed (Fig. 22).

Table 15. RA fractions of selected Gleeble simulated samples measured using XRD and EBSD (Reprinted under CC BY 4.0 license from Publication VI © 2022 Authors).

Specimen	RA XRD [vol.%]	RA EBSD [vol.%]
Steel A QP (T_P=350 °C)	10	8
Steel A ART (T_R=710 °C,t_R=1000 s)	22	11
Steel B QP (T_P=350 °C)	20	21
Steel B ART (T_R=660 °C,t_R=5000 s)	49	38
Steel C QP (T_P=350 °C)	17	11
Steel C ART (T_R=710 °C,t_R=5000 s)	24	5

5.2 Mechanical properties

Hardness measurements were carried out to initially assess the influence of microstructural phase constituents. In the QP process, increasing T_P and t_P resulted in consequent decrement of hardness of the samples. The tempering of martensite at a higher T_P and a longer t_P certainly has a remarkable influence on the mechanical properties of the QP-processed High-Al, High-Si and Si-Al steel specimens. Increased softening was obvious not only because of the increased tempering of martensite, but also due to the enhanced RA fractions stabilized at RT. T_Q in the range 200 to 260 °C seems to have a marginal influence on the hardness. In the case

of unstrained samples, the hardness values are of the same level as those of the strained specimens.

For medium-Mn steels, an increase in T_P expectedly resulted in a consequent decrease in hardness, though the hardness drop was small. In medium-Mn Steel A, the fraction of RA was nearly constant in the T_P range of 200–400 °C, which suggests that the decrease in hardness was not because of increase in the RA fractions, as observed previously in a (high) silicon-aluminum QP steel with a lower Mn content and reported in Publication I. Thus, tempering of martensite must be the main reason for this softening. In medium-Mn Steels A, B and C, the carbon contents of RA increased with increasing T_P from 200 to 350 °C, which also resulted in lower contents of carbon in martensite. At T_P 300 and 350 °C, the hardness of medium-Mn Steel C seems to have dropped relatively faster compared to that of medium-Mn Steel A, which might be a result from a significant higher RA fraction. The hardness of medium-Mn Steels A and C corresponding to T_P 400 °C was practically same, 481 and 486 HV, respectively, even though the RA fraction in medium-Mn Steel C was higher (17 vs. 11%). Thus, the variation of hardness in the studied QP-treated steels is quite complex. On the other hand, at T_P 500 °C, the hardness of medium-Mn Steel C was higher than that of medium-Mn Steel A, even though the dilatation experiments indicated some formation of FM in medium-Mn Steel A unlike in the case of Steel C. This suggests that the partitioning at a high T_P can promote formation of pearlite and precipitation of carbides within the austenite films [81].

For the ART-processed medium-Mn steels, hardness evaluation seemed to be even more complex than in the case of QP-processed specimens, as shown in Table 13. Not only the T_R and t_R of ART treatments, but also the heating step to T_R can significantly affect the microstructural evolution and corresponding mechanical properties [63]. A decrease in the heating rate can lead to the formation of austenite grains at different temperatures, thereby resulting in a more heterogenous distribution of Mn among different austenite grains as well as inside an individual austenite grain [105]. Furthermore, a considerable scatter in hardness values in some ART-treated specimens was probably because of the influence of multiphase microstructures, segregation of Mn, Si and Ni, combined with the narrow A_{C1}–A_{C3} range.

As expected, the TMR-DQ processing resulted in slightly higher strengths and hardness values in comparison with those of the corresponding DQP versions. Elongations were comparatively greater at the upper T_Q 225 °C irrespective of steel type, presumably because of the higher RA fractions in tensile specimens. The

corresponding average carbon contents of RA in TMR-DQP specimens was found to be higher, suggesting better thermal stability of RA, thus corroborating higher tensile ductility obtained on these samples.

During TMR-DQP processing, the T_Q temperature seems to have a significant influence on the resultant mechanical properties, even though the difference in T_Q was only 50 °C between the two laboratory rolling experiments, i.e., T_Q of 175 and 225 °C. In contrast, alloying elements such as Si, Al and Cr only had an insignificant effect on the tensile properties of High-Al and High-Si steels.

To determine the stability of RA, the reduction in the RA content with imposed true strain and the corresponding mean carbon contents of the austenite have been measured from different sections of the tensile test samples as well as interrupted tensile-tested specimens from TMR-DQP-processed samples. Increasing the T_Q has been found to increase the RA fraction and its carbon content, and hence the stability of RA [90]. In Fig. 26, the RA fractions, carbon contents of RA and corresponding hardness values, obtained on TMR-DQP-processed High-Al and High-Si steels with T_Q = 225 °C, have been plotted as a function of true strain. The steel composition seems to have only a slight effect on the decreasing amount of the RA fraction during straining. Following straining, the increase in carbon content of RA was significantly higher for Steel A than Steel B. On the other hand, an increased carbon content in austenite due to straining means increased hardness of the martensite that forms during straining, though the difference in hardness between the two steels is small. Very fine, interlath austenite films between martensitic laths can have relatively higher carbon contents due to short diffusion distances and are very stable.

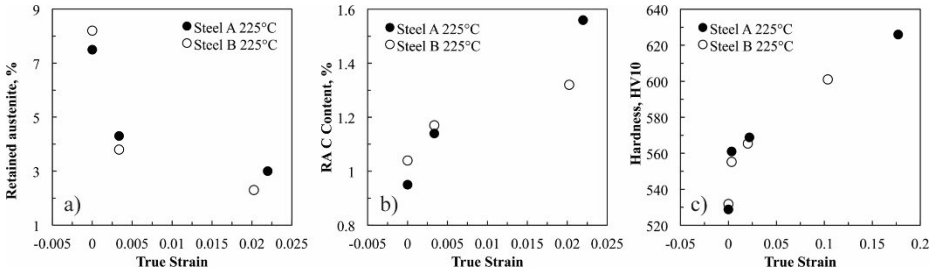

Fig. 26. Summary for the effect of true strain on a) the fraction of RA, b) the carbon content of RA and c) the Vickers hardness 10 kgf (HV10) hardness. Note the different true strain scale in c) (Reprinted under CC BY 4.0 license from Publication IV © 2019 Authors).

True stress-strain curves along with instantaneous work hardening exponents (n) and WHRs for the TMR-DQP-processed High-Al and High-Si steels at T_Q 175 and 225 °C, are illustrated in Fig. 27. Both steels contained higher RA fraction (~10%) in samples quenched at T_Q 225 °C compared to those quenched at T_Q 175 °C, reflecting their higher n values at true strains beyond 0.03. Not only the fraction, but also the stability of RA influenced the n values. Further, the stability differences of RA may result from the shape and size of the RA pools and interlath films as well as the distribution of carbon in austenite, which, in turn, will depend on the T_Q temperature as discerned from different carbon contents in Table 9 [6].

Tensile samples made from TMR-DQP-processed High-Al and High-Si steels had approximately equal PAGS, M_s temperature, volume fraction of RA and nearly identical mean carbon contents in the RA. Consequently, the difference in alloying contents combined with reasonably high RA fraction explains reasonably why the n values and the WHRs of High-Al steel were slightly higher than the corresponding values of High-Si steel at T_Q 225 °C. WHR decreased more slowly at higher T_Q 225 °C than at T_Q 175 °C. This is probably due to higher average carbon content of RA giving it a higher stability.

Even at T_Q 225 °C for TMR-DQP-processed steels, n dropped to low values before a strain of 0.07 was reached. According to XRD measurements, the phase transformation started already at small elongation values and most of the RA had transformed to martensite before UEL was reached. This suggests that RA fraction was too low and unstable, thus transforming too early to fresh martensite during straining, and that its effect on UEL remained moderately low.

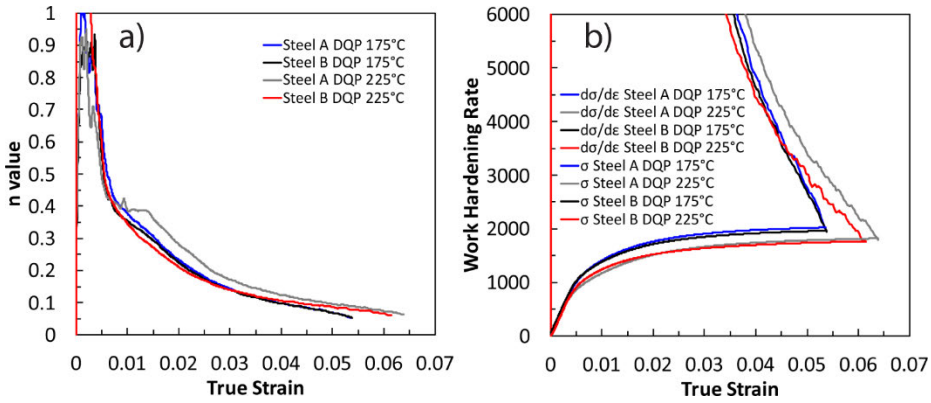

Fig. 27. a) Instantaneous work hardening exponent (*n* value), b) work hardening rate and true stress as a function of true strain for Steel A and B at T_Q 175 and 225 °C (Reprinted under CC BY 4.0 license from Publication IV © 2019 Authors).

The TMR-DQP treatment has a significant effect on the impact toughness of these steels. The Charpy-V impact energies of TMR-DQP-treated steels have been shown to be much higher compared to the corresponding impact energies of the TMR-DQ-processed samples, as shown in Fig. 13. Despite higher YS, the DQP variants at lower T_Q 175 °C showed similar or better transition temperatures, as shown in Fig. 28. The best combination of strength and 28 J transition temperature (T28J) are obtained for High-Si steel at T_Q 175 °C. The effect of steel composition and T_Q on the relationship between strength and transition temperature seems to be due to the microstructural differences that are related to the critical stress for cleavage crack nucleation and propagation. Normally, low-angle grain boundaries are not considered to be effective obstacles to cleavage cracks, but intergranular fracture can mainly occur along the boundaries of the prior austenite which can carry more impurities and segregation of alloying elements than the other high angle boundaries, such as martensitic packet and block boundaries [106], [107]. The lath size of 1.11 µm in the sample with the lowest T28J in Fig. 28 was smaller than that of the other specimens. Contrary to expectations, the lath size was probably a significant factor controlling the transition temperatures due to the appearance of interlath austenite.

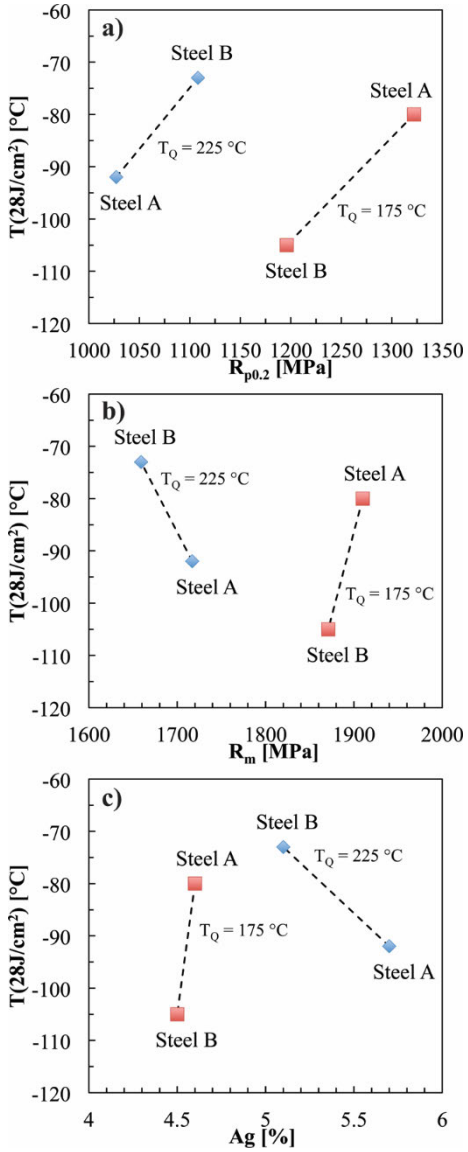

Fig. 28. a) Effect of the yield strength ($R_{p0.2}$), b) tensile strength (R_m) and c) plastic component of uniform elongation (A_g) on 28 J/cm² transition temperature for TMR-DQP-processed steels (Adapted under CC BY 4.0 license from Publication IV © 2019 Authors).

For the TMR-DQP steels, the wear performance was principally dependent on the initial surface hardness of the wear test specimens. The presence of RA, however, did not appear to have any beneficial effect on the wear resistance of TMR-DQP steels, though the excellent low temperature toughness of TMR-DQP samples suggest their better application possibility in sub-zero conditions at the same hardness/strength level as that of the used wear-resistant steels.

The finely divided RA present in DQP steels was expected to impart greater strain hardening capacity in the steels, and hence, better wear resistance against abrasion and impact wear due to TRIP induced martensite formation in the steel. Obviously, strain hardening and strain induced martensite transformation are supposed to be activated depending on the stability of the austenite, thereby improving the wear resistance. The hardening of the surface due to phase transformation is considered as the main criterion in improving the surface behavior to withstand more cutting and ploughing during abrasion and wear testing. However, the wear performance was found to be mostly dependent on the initial surface hardness of the DQP samples, suggesting inadequate stability of the austenite for the desired result. Accordingly, the direct quenched variants exhibited lower mass loss because of the higher initial surface hardness. More work needs to be done to improve the wear-resistance of the DQP steels.

Based on the Gleeble simulation results (hardness approximately 500 HV), a number of selected QP- and ART-processed specimens prepared from laboratory hot-rolled sheets were preliminarily tested for tensile properties. The aim was to enable the estimation of mechanical properties such as tensile strength and elongation on bulk samples. The Gleeble data were suitably analyzed to design the TMR-QP and TMR-ART treatment schedules in respect of reheating, quenching, and subsequent holding temperatures, and times to conduct laboratory hot rolling. Quenching to the targeted T_Q directly after hot rolling was one of the challenging stages of the QP process, whereas annealing the specimens at T_R within the narrow process window was another challenging step during the ART process. The results obtained via the Gleeble simulation and laboratory hot-rolling process in respect of RA fractions, carbon contents of RA and hardness data are listed in Table 16. There are differences between the Gleeble-simulated and laboratory hot-rolled specimens in respect of RA and hardness data, particularly in the case of ART-processed medium-Mn Steels A and B. One reason for these differences is attributed to the challenges that are encountered in controlling the TMR-ART processing.

Table 16. A comparison of RA fractions, carbon contents of RA hardness data of Gleeble simulated and laboratory hot-rolled specimens (Reprinted under CC BY 4.0 license from Publication VI © 2022 Authors).

Material	Gleeble	Hot Rolled	Gleeble	Hot Rolled	Gleeble	Hot Rolled
	RA%	RA%	RA C%	RA C%	HV10	HV10
Steel A-QP (T_Q=100 °C T_P=400 °C t_P=1000 s)	11	6	1.03	1.01	481	514
Steel B-QP (T_Q=100 °C T_P=350 °C t_P=1000 s)	20	16	0.94	0.84	486	506
Steel C-QP (T_Q=150 °C T_P=400° C t_P=1000 s)	17	15	0.99	1.05	486	512
Steel A-ART (T_R=710 °C t_R=1000 s)	22	33	0.46	0.68	477	317
Steel B-ART (T_R=630 °C t_R=1000 s)	25	11	0.49	0.58	361	363
Steel C-ART (T_R=710 °C t_R=5000 s)	24	28	0.63	0.48	464	417

According to the XRD measurements made on samples shown in Table 16 after tensile testing, only the TMR-QP-processed medium-Mn Steels A and C revealed small fractions of stable RA that did not undergo strain induced transformation in tensile tests, suggesting small amounts of highly stabilized RA in these samples compared to practically no perceptible RA in the TMR-QP-processed medium-Mn Steel B after tensile testing. In the case of TMR-ART-processed specimens, the carbon contents of RA were relatively lower compared to those of TMR-QP-treated samples as shown in Table 16 regardless of steel composition and exhibited lower thermal stabilities. Accordingly, most of the RA fractions in these samples transformed to martensite during deformation in tensile tests. The RA fractions of less than 1% were present in TMR-ART-processed medium-Mn Steels A and C. Correspondingly, in medium-Mn Steel B, RA fraction was not detectable.

It seems that RA fractions and its stability varied significantly between different steels and the adopted processing routes. Additionally, one study has demonstrated that the relationship between RA fraction and mechanical properties can be quite scattered [108]. It has also been indicated that the same RA fraction can provide different strength-ductility balances and, alternatively, different RA fractions can result in the same level of strength-ductility balance [65]. This has a direct consequence to the fact that the strength-ductility balance is related to volume fraction and stability of RA (mostly composition and grain size) as well as the strength and morphology of martensite.

By optimizing T_Q, T_P and t_P parameters, it was possible to achieve good combinations of strength and ductility in TMR-QP-processed 3–4% medium-Mn steels as well as in corresponding TMR-ART-treated steels by optimizing T_R and t_R parameters, as shown in Table 14. Even same level of RA (e.g., ~25%) can be

obtained in QP and ART treatments. The UTS x TEL products, however, were quite different depending on the experimental conditions as shown in Table 14. The hardness of the QP-processed medium-Mn Steel B (T_P 400 °C, t_P 1000 s) with 26% of RA fraction was 456 HV, essentially due to the martensitic matrix. In comparison, the hardness of ART-processed medium-Mn Steel B (T_R 660 °C, t_R 100 s) was 383 HV, which is appreciably low due to highly tempered martensitic (ferritic) matrix. The preference of the processing route depends on the desired property combination among others.

5.3 Static recrystallization kinetics for direct quenching and partitioning

Based on the static recrystallization characteristics and kinetics studies on the 2Mn-1Si (High-Si) and 3Mn-1.5Si steels, the flow stress behavior displayed the occurrence of work hardening and dynamic recovery in the temperature range 900 to 1100 °C for specimens deformed mostly to 0.2 strain, with no significant differences in flow stress levels between these two steels. Similar observations were made earlier for the 3 and 5% Mn steels [109], [110]. Additionally, these two steels seemed to have a weak dependence of SRX on strain rate. In Publication II, fractional softening equations have been developed, which give reasonable predictions of the SRX kinetics for both steels, and the time for 50% recrystallization was exponentially proportional to the inverse of temperature and directly proportional to the product of strain, strain rate and grain size all raised to respective powers. These equations can be used to predict the recrystallization times for the two steels during recrystallization-controlled rolling, thereby avoiding partial recrystallization and ensuring fine grains sizes during the rough rolling stage of thermomechanical rolling. It was demonstrated that increasing the contents of Mn and Si made the recrystallization kinetics less sensitive to strain, strain rate and temperature, i.e., the powers of strain and strain rate became less negative and the activation energy of recrystallization was marginally reduced.

6 Future considerations

During QP processing, the characteristics and kinetics of partitioning were investigated for unstrained and strained samples in Publication I in order to clarify the influence on subsequent dilatation behavior, microstructure development, RA stabilization and related carbon content. One unexpected result of this study was getting partially recrystallized microstructures in strained samples, even though the deformation temperatures were quite low, such as 800 °C. It could be interesting and useful to investigate more deformation conditions to clarify the conditions that prevent recrystallization from occurring. It can be supposed that a fully deformed, pancaked structure without partial recrystallization would result in highly refined and randomized transformed microstructures containing mainly finely divided film-like RA that could impart high mechanical properties, including low temperature toughness.

During various investigations on processing, structures, and properties of QP/DQP steels reported in Publications I, III, IV, V, it was found that even a quantity as low as 0.0030 wt.% nitrogen can deteriorate TEL values for steels containing Al and can cause significant scatter in impact toughness. According to SEM-EDS examinations, these steels contain a high level of alumina inclusions. When the nitrogen content was further reduced to a level of 0.0010 wt.% in Al-bearing QP steels, the tensile ductility improved significantly and was as good as those of steels without Al alloying. Therefore, it will be interesting to find out the limit of nitrogen quantity which will deteriorate ductility properties in such steels processed through the QP/DQP route. If the exact limit can be found out in the future, I would like to name it the “hedgehodge” limit. In addition, it will be interesting to investigate whether the problem can be circumvented without any specific need to control the nitrogen content below the normal level of 0.003 wt.%, which can make the process expensive.

According to Publication IV, contrary to expectations, the lath size of martensite was probably a significant factor in controlling the transition temperatures due to the appearance of interlath austenite. Further study is required to confirm this observation.

Based on the results of Publication VI, it could be interesting to investigate the ART processing of Steels A and C samples at lower T_R like what has been done for Steel B. On the other hand, studies on Medium-Mn steel should be continued with slightly different compositions (high Mn contents) and/or ART heat treatments based on the results of this study. At the same time, particular attention should be paid on controlling the furnace treatments to minimize the variation of temperature,

as this study clearly revealed that the processing window for ART processing is generally very narrow.

7 Summary and conclusions

The research work done in this thesis aimed at studying new QP- and ART-processed experimental steels with industrially relevant laboratory hot rolling experiments. These hot rolling experiments were designed based on the results of preliminary Gleeble simulations, as described in relevant details. The key aspects of the study were to develop appropriate combinations of microstructures for new experimental steels to accomplish the desired combinations of strength, ductility, and toughness. RA played an important role in achieving sufficient ductility in essentially martensitic structures. The aim of this study was to provide an up-to-date understanding regarding possibilities and challenges existing with the DQP and ART processing, when trying to impart desired high mechanical properties in medium carbon (0.3C) steels with relatively inexpensive alloying additions. Many techniques, such as LOM, LSCM, FESEM, EBSD, EDS, STEM, EPMA and XRD, were utilized to carry out detailed microstructural characterization of the materials. The mechanical properties were evaluated in respect of hardness, tensile and Charpy V impact toughness properties. Based on the studies, the summary of the main results and related conclusions can be outlined as follows:

- During the QP treatment, apart from carbon partitioning from supersaturated martensite to untransformed austenite, isothermal holding (partitioning) resulted in austenite decomposition to bainite and isothermal martensite, followed by possible formation of some untempered, occasionally twinned, high-carbon FM during final cooling, thereby stabilizing a fraction of RA at RT. This process was observed in all (high) silicon-aluminum steels, regardless of the composition.
- There was a systematic increase in fraction of RA with partitioning time, both for the unstrained and strained conditions for all (high) silicon-aluminum steels. Deformed specimens showed only marginally higher fractions of RA compared to corresponding unstrained samples.
- T_Q in the range of 200 to 260 °C only has a minor effect on the hardness of (high) silicon-aluminum steels.
- Deformation in austenite in T_{NR} temperature regime prior to QP treatment did not accelerate formation of bainite during partitioning in the case of (high) silicon-aluminum steels, contrary to its accelerated tempering of martensite.
- Deformation in the T_{NR} temperature range, in effect, resulted in partially recrystallized microstructures for (high) silicon-aluminum steels.

- In (high) silicon-aluminum steels, the decomposition behavior of RA during partitioning was closely similar regardless of composition, i.e., the effect of alloying addition on the decomposition behavior was minor.
- In TMR-DQP-treated high-Al and high-Si steels, RA fraction increased from 6.5 to 10% as T_Q increased from 175 and 225 °C. Accordingly, the respective average carbon content of RA increased from 0.60 to 0.94 wt.%. Most of the RA was finely divided as interlath austenite between martensite laths, whereas small fractions of RA existed as micron-sized pools.
- Not only the volume fraction of RA, but also the decrease in the lath size of martensite and interlath RA (i.e., refinement of lath structure) seemed to have improved the impact toughness, at least in the case of TMR-DQP-treated high-silicon steel. Samples with most finely divided RA as films (e.g., ECD value of 1.11 μm) between martensite resulted in the lowest transition temperatures (e.g., T28J temperature of −105 °C) in Charpy-V impact tests, even though the fraction of RA (6.6%) was moderately low.
- Wear performance was mostly dependent on the initial surface hardness, but the presence of RA, however, did not improve the wear resistance of DQP-processed steels, presumably due to inadequate stability of RA.
- The TMR-DQP process can provide the desired processing route when aiming to improve the strength-ductility combination with noticeably improved low temperature toughness. YS and UTS levels of 1200 MPa and 1870 MPa, respectively, combined with TEL level of 12% could be reached in laboratory-scale hot rolling simulations of High-Si steel.
- Most of the RA had blocky morphology in QP-processed medium-Mn steels. Utilizing the ART process enabled achieving higher RA fraction compared to that obtained in QP process steels. On the other hand, the highest carbon contents in RA were achieved only via the QP process. After the ART processing with annealing at higher T_R temperatures, microstructures essentially contained ferrite (TM), film-like interlath RA, cementite, and FM.
- In the case of medium-Mn steels, it seems that the combined effect of Mn and Si suppress the bainitic transformation, similarly as Mo and V do during QP processing.
- Alloying with high Mn (4 wt.%) and Ni (2 wt.%) was found to be beneficial for stabilizing high RA fractions (up to 49%) by the ART processing under the conditions T_R = 660 °C and t_R = 5000 s, close to equilibrium levels, as predicted by the thermodynamic analysis using the Thermo-Calc software.

- Alloying with Mo and V only had a minor effect in respect of stabilizing the RA fractions, carbon contents of RA, M_s temperature and hardness values for the ART-processed samples.
- The implementation of TMR-DQP processing on the laboratory rolling mill was somewhat challenging and might have influenced the microstructures and mechanical properties that are sensitive to the T_Q temperatures. Similarly, controlling of ART processing at correct T_R temperatures in the narrow processing windows was quite challenging.

8 Novel features

The following results are believed to be novel at the time of publishing:

- One unexpected finding was that the deformation at low temperature 800 °C resulted in a partially recrystallized structure containing fine recrystallized grains in (high) silicon-aluminum steels.
- In the case of (high) silicon-aluminum steels, deformation close to T_{NR} did not accelerate formation of bainite during QP processing, and one reason for that could be partial recrystallization resulting in lowering of dislocation density.
- T_Q seems to have significant influence on the mechanical properties of high-aluminum and high-silicon steels, and even a small difference of 50 °C in quenching temperature from 175 to 225 °C can lead to large differences in mechanical properties. In contrast, alloying elements such as Si, Al and Cr had insignificant effect on the tensile strength and elongation.
- Normally, low angle boundaries are not considered to be effective obstacles in the propagation of cleavage cracks. The lath size of 1.11 μm (ECD) of the high-silicon steel samples with the lowest 28 J transition (T28J) temperature was smaller than other specimens. Contrary to expectations, the lath size is probably a significant factor controlling the transition temperature due to the appearance of interlath austenite.
- One notable effect of DQP process on the properties of steel was in respect of improving remarkably the Charpy V impact toughness, when compared with those obtained on DQ-processed samples. Via the TMR-DQP process can reach practically as high UTS (1910 MPa) as via TMR-DQ process (2086 MPa) and completely better impact toughness (T28J ≤ −60 °C vs. >>40 °C).
- It seems that most of the RA in QP-processed medium-Mn steels are in the form of pools alongside some elongated lath-shaped grains. The presence of some very fine interlath RA could also be detected by TEM. As a result of Mn segregation, a fraction of austenite grains in Mn-enriched areas presumably remained untransformed following quenching to T_Q and resulted in the blocky-shaped morphology of RA.
- In QP processing, a quantity as low as 0.0030 wt.% nitrogen can deteriorate TEL values for steels containing Al. When the nitrogen content was further reduced to a level of 0.0010 wt.% in Al-bearing QP steels, the tensile ductility improved significantly.

References

[1] D. Fan, N. Fonstein, and H. Jun, “Effect of Microstructure on Tensile Properties and Cut-Edge Formability of DP, TRIP, Q&T and Q&P Steels,” *AIST Trans.*, vol. 13, pp. 180–185, 2015.

[2] N. Fonstein, *Advanced High Strength Sheet Steels*, 1st ed. Cham: Springer International Publishing, 2015.

[3] A. K. Behera and G. B. Olson, “Prediction of Carbon Partitioning and Austenite Stability via Non-equilibrium Thermodynamics in Quench and Partition (Q&P) Steel,” *Jom*, vol. 71, no. 4, pp. 1375–1385, 2019.

[4] D. De Knijf, C. Föjer, L. A. I. Kestens, and R. Petrov, “Factors influencing the austenite stability during tensile testing of Quenching and Partitioning steel determined via in-situ Electron Backscatter Diffraction,” *Mater. Sci. Eng. A*, vol. 638, pp. 219–227, 2015.

[5] D. De Knijf, R. Petrov, C. Föjer, and L. A. I. Kestens, “Effect of fresh martensite on the stability of retained austenite in quenching and partitioning steel,” *Mater. Sci. Eng. A*, vol. 615, pp. 107–115, 2014.

[6] E. Pereloma, A. Gazder, and I. Timokhina, “Retained Austenite: Transformation-Induced Plasticity,” *Encycl. Iron, Steel, Their Alloy.*, no. June, pp. 3088–3103, 2016.

[7] M. C. Somani, D. A. Porter, P. Karjalainen, T. Rasmus, and A. M. Hirvi, “Patent Application Publication US 2014/0299237 A1,” 2014.

[8] A. Arlazarov, A. Hazotte, O. Bouaziz, M. Gouné, and F. Kegel, “Characterization of microstructure formation and mechanical behavior of an advanced medium Mn steel,” *Mater. Sci. Technol. Conf. Exhib. 2012, MS T 2012*, vol. 2, pp. 1124–1131, 2012.

[9] S. Lee, S. J. Lee, and B. C. De Cooman, “Austenite stability of ultrafine-grained transformation-induced plasticity steel with Mn partitioning,” *Scr. Mater.*, vol. 65, no. 3, pp. 225–228, 2011.

[10] B. W. Darvell, “Steel and Cermet,” in *Materials Science for Dentistry*, Elsevier, 2018, pp. 540–554.

[11] H. Luo, J. Shi, C. Wang, W. Cao, X. Sun, and H. Dong, “Experimental and numerical analysis on formation of stable austenite during the intercritical annealing of 5Mn steel,” *Acta Mater.*, vol. 59, no. 10, pp. 4002–4014, 2011.

[12] D. A. Porter, K. E. Easterling, and M. Y. Sherif, *Phase Transformations in Metals and Alloys*, Fourth. Boca Raton: CRC Press, 2021.

[13] G. Krauss, “Martensite in steel: Strength and structure,” *Mater. Sci. Eng. A*, vol. 273–275, pp. 40–57, 1999.

[14] S. Morito, X. Huang, T. Furuhara, T. Maki, and N. Hansen, “The morphology and crystallography of lath martensite in alloy steels,” *Acta Mater.*, vol. 54, no. 19, pp. 5323–5331, 2006.

[15] S. Morito, Y. Adachi, and T. Ohba, “Morphology and crystallography of Sub-blocks in ultra-low carbon lath martensite steel,” *Mater. Trans.*, vol. 50,

no. 8, pp. 1919–1923, 2009.
[16] E. I. Galindo-Nava and P. E. J. Rivera-Díaz-Del-Castillo, “A model for the microstructure behaviour and strength evolution in lath martensite,” *Acta Mater.*, vol. 98, pp. 81–93, 2015.
[17] S. Li, G. Zhu, and Y. Kang, “Effect of substructure on mechanical properties and fracture behavior of lath martensite in 0.1C-1.1Si-1.7Mn steel,” *J. Alloys Compd.*, vol. 675, pp. 104–115, 2016.
[18] T. J. Headley and J. A. Brooks, “A new Bcc-Fcc orientation relationship observed between ferrite and austenite in solidification structures of steels,” *Metall. Mater. Trans. A Phys. Metall. Mater. Sci.*, vol. 33, no. 1, pp. 5–15, 2002.
[19] S. M. C. van Bohemen and J. Sietsma, “The kinetics of bainite and martensite formation in steels during cooling,” *Mater. Sci. Eng. A*, vol. 527, no. 24–25, pp. 6672–6676, 2010.
[20] A. Borgenstam, P. Hedström, M. Hillert, P. Kolmskog, A. Stormvinter, and J. Ågren, “On the symmetry among the diffusional transformation products of austenite,” *Metall. Mater. Trans. A Phys. Metall. Mater. Sci.*, vol. 42, no. 6, pp. 1558–1574, 2011.
[21] A. M. Ravi, “Understanding bainite formation in steels,” Delft University of Technology, 2019.
[22] Z. G. Yang and H. S. Fang, “An overview on bainite formation in steels,” *Curr. Opin. Solid State Mater. Sci.*, vol. 9, no. 6, pp. 277–286, 2005.
[23] D. Kim, S. J. Lee, and B. C. De Cooman, “Microstructure of low C steel isothermally transformed in the M S to M f temperature range,” *Metall. Mater. Trans. A Phys. Metall. Mater. Sci.*, vol. 43, no. 13, pp. 4967–4983, 2012.
[24] P. K. Kantanen, V. Javaheri, M. C. Somani, D. A. Porter, and J. I. Kömi, “Effect of deformation and grain size on austenite decomposition during quenching and partitioning of (high) silicon-aluminum steels,” *Mater. Charact.*, vol. 171, p. 110793, Jan. 2021.
[25] P. Kantanen *et al.*, “Microstructures and mechanical properties of three medium-Mn steels processed via quenching and partitioning as well as austenite reversion heat treatments,” *Mater. Sci. Eng. A*, vol. 847, no. March, p. 143341, Jul. 2022.
[26] S. K. Liu and J. Zhang, “The influence of the Si and Mn concentrations on the kinetics of the bainite transformation in Fe-C-Si-Mn alloys,” *Metall. Trans. A*, vol. 21, no. 6, pp. 1517–1525, 1990.
[27] M. J. Santofimia, L. Zhao, and J. Sietsma, “Overview of mechanisms involved during the quenching and partitioning process in steels,” *Metall. Mater. Trans. A Phys. Metall. Mater. Sci.*, vol. 42, no. 12, pp. 3620–3626, 2011.
[28] F. Xu, Y. Wang, B. Bai, and H. Fang, “CCT curves of low-carbon Mn-Si steels and development of water-cooled bainitic steels,” *J. Iron Steel Res.*

Int., vol. 17, no. 3, pp. 46–50, Mar. 2010.
[29] D. Quidort and Y. Bréchet, "The role of carbon on the kinetics of bainite transformation in steels," *Scr. Mater.*, vol. 47, no. 3, pp. 151–156, Aug. 2002.
[30] F. G. Caballero and H. K. D. H. Bhadeshia, "Very strong bainite," *Curr. Opin. Solid State Mater. Sci.*, vol. 8, no. 3–4, pp. 251–257, Jun. 2004.
[31] X. Y. Long, J. Kang, B. Lv, and F. C. Zhang, "Carbide-free bainite in medium carbon steel," *Mater. Des.*, vol. 64, pp. 237–245, Dec. 2014.
[32] M. C. Somani, D. A. Porter, L. P. Karjalainen, P. P. Suikkanen, and R. D. K. Misra, "Process design for tough ductile martensitic steels through direct quenching and partitioning," *Mater. Today Proc.*, vol. 2, pp. S631–S634, 2015.
[33] J. G. Speer, D. V. Edmonds, F. C. Rizzo, and D. K. Matlock, "Partitioning of carbon from supersaturated plates of ferrite, with application to steel processing and fundamentals of the bainite transformation," *Curr. Opin. Solid State Mater. Sci.*, vol. 8, no. 3–4, pp. 219–237, 2004.
[34] M. J. Santofimia, L. Zhao, R. Petrov, C. Kwakernaak, W. G. Sloof, and J. Sietsma, "Microstructural development during the quenching and partitioning process in a newly designed low-carbon steel," *Acta Mater.*, vol. 59, no. 15, pp. 6059–6068, 2011.
[35] E. de Moor, S. Lacroix, A. J. Clarke, J. Penning, and J. G. Speer, "Effect of retained austenite stabilized via quench and partitioning on the strain hardening of martensitic steels," *Metall. Mater. Trans. A Phys. Metall. Mater. Sci.*, vol. 39, no. 11, pp. 2586–2595, 2008.
[36] J. G. Speer, F. C. R. Assunção, D. K. Matlock, and D. V. Edmonds, "The 'quenching and partitioning' process: background and recent progress," *Mater. Res.*, vol. 8, no. 4, pp. 417–423, 2005.
[37] A. J. Clarke *et al.*, "Carbon partitioning to austenite from martensite or bainite during the quench and partition (Q&P) process: A critical assessment," *Acta Mater.*, vol. 56, no. 1, pp. 16–22, 2008.
[38] D. V. Edmonds, K. He, F. C. Rizzo, B. C. De Cooman, D. K. Matlock, and J. G. Speer, "Quenching and partitioning martensite-A novel steel heat treatment," *Mater. Sci. Eng. A*, vol. 438–440, no. SPEC. ISS., pp. 25–34, 2006.
[39] E. Kozeschnik and H. K. D. H. Bhadeshia, "Influence of silicon on cementite precipitation in steels," *Mater. Sci. Technol.*, vol. 24, no. 3, pp. 343–347, 2008.
[40] E. De Moor, S. Lacroix, L. Samek, J. Penning, and J. G. Speer, "Dilatometric Study of the Quench and Partitioning Process," *3rd Int. Conf. Adv. Struct. Steels*, pp. 1–6, 2006.
[41] E. J. Seo, L. Cho, and B. C. De Cooman, "Application of quenching and partitioning (Q&P) processing to press hardening steel," *Metall. Mater. Trans. A Phys. Metall. Mater. Sci.*, vol. 45, no. 9, pp. 4022–4037, 2014.
[42] H. K. D. H. Bhadeshia and D. V. Edmonds, "The bainite transformation in

a silicon steel," *Metall. Trans. A*, vol. 10, no. 7, pp. 895–907, 1979.
[43] D. T. Pierce *et al.*, "Microstructural evolution during quenching and partitioning of 0.2C-1.5Mn-1.3Si steels with Cr or Ni additions," *Acta Mater.*, vol. 151, pp. 454–469, 2018.
[44] G. I. Rees, J. Perdrix, T. Maurickx, and H. K. D. H. Bhadeshia, "The effect of niobium in solid solution on the transformation kinetics of bainite," *Mater. Sci. Eng. A*, vol. 194, no. 2, pp. 179–186, 1995.
[45] H. Hu, G. Xu, L. Wang, Z. Xue, Y. Zhang, and G. Liu, "The effects of Nb and Mo addition on transformation and properties in low carbon bainitic steels," *Mater. Des.*, vol. 84, no. 2, pp. 95–99, Nov. 2015.
[46] P. M. Kaikkonen, M. C. Somani, I. H. Miettunen, D. A. Porter, S. T. Pallaspuro, and J. I. Kömi, "Constitutive flow behaviour of austenite at low temperatures and its influence on bainite transformation characteristics of ausformed medium-carbon steel," *Mater. Sci. Eng. A*, vol. 775, no. January, pp. 9–11, 2020.
[47] D. Kim, J. G. Speer, and B. C. De Cooman, "Isothermal transformation of a CMnSi steel below the MS temperature," *Metall. Mater. Trans. A Phys. Metall. Mater. Sci.*, vol. 42, no. 6, pp. 1575–1585, 2011.
[48] J. Speer, D. K. Matlock, B. C. De Cooman, and J. G. Schroth, "Carbon partitioning into austenite after martensite transformation," *Acta Mater.*, vol. 51, no. 9, pp. 2611–2622, 2003.
[49] E. J. Seo, L. Cho, and B. C. De Cooman, "Kinetics of the partitioning of carbon and substitutional alloying elements during quenching and partitioning (Q&P) processing of medium Mn steel," *Acta Mater.*, vol. 107, pp. 354–365, 2016.
[50] H. Y. Li, X. W. Lu, W. J. Li, and X. J. Jin, "Microstructure and mechanical properties of an Ultrahigh-Strength 40SiMnNiCr steel during the one-step quenching and partitioning process," *Metall. Mater. Trans. A Phys. Metall. Mater. Sci.*, vol. 41, no. 5, pp. 1284–1300, 2010.
[51] I. Tsukatani, S. Hashimoto, and T. Inoue, "Effects of Silicon and Manganese Addition on Mechanical Properties of High-Strength Hot-Rolled Sheet Steel Containing Retained Austenite," *ISIJ Int.*, vol. 31, no. 9, pp. 992–1000, 1991.
[52] W. Huo *et al.*, "Effect of Nb contents on microstructure characteristics and yielding behavior of Fe–4Mn–2Al-0.2C steel," *Mater. Sci. Eng. A*, vol. 819, no. May, pp. 1–12, 2021.
[53] E. De Moor, J. G. Speer, D. K. Matlock, J.-H. Kwak, and S.-B. Lee, "Effect of Carbon and Manganese on the Quenching and Partitioning Response of CMnSi Steels," *ISIJ Int.*, vol. 51, no. 1, pp. 137–144, 2011.
[54] D. W. Suh, S. J. Park, T. H. Lee, C. S. Oh, and S. J. Kim, "Influence of Al on the microstructural evolution and mechanical behavior of low-carbon, manganese transformation-induced-plasticity steel," *Metall. Mater. Trans. A Phys. Metall. Mater. Sci.*, vol. 41, no. 2, pp. 397–408, 2010.

[55] Y. K. Lee and J. Han, “Current opinion in medium manganese steel,” *Mater. Sci. Technol. (United Kingdom)*, vol. 31, no. 7, pp. 843–856, 2015.

[56] J. Han, S. J. Lee, J. G. Jung, and Y. K. Lee, “The effects of the initial martensite microstructure on the microstructure and tensile properties of intercritically annealed Fe-9Mn-0.05C steel,” *Acta Mater.*, vol. 78, pp. 369–377, 2014.

[57] P. J. Gibbs, E. De Moor, M. J. Merwin, B. Clausen, J. G. Speer, and D. K. Matlock, “Austenite stability effects on tensile behavior of manganese-enriched- austenite transformation-induced plasticity steel,” *Metall. Mater. Trans. A Phys. Metall. Mater. Sci.*, vol. 42, no. 12, pp. 3691–3702, 2011.

[58] S. Lee, S. J. Lee, S. Santhosh Kumar, K. Lee, and B. C. D. Cooman, “Localized deformation in multiphase, ultra-fine-grained 6 Pct Mn transformation-induced plasticity steel,” *Metall. Mater. Trans. A Phys. Metall. Mater. Sci.*, vol. 42, no. 12, pp. 3638–3651, 2011.

[59] J. M. Jang, S. J. Kim, N. H. Kang, K. M. Cho, and D. W. Suh, “Effects of annealing conditions on microstructure and mechanical properties of low carbon, manganese transformation-induced plasticity steel,” *Met. Mater. Int.*, vol. 15, no. 6, pp. 909–916, 2009.

[60] H. S. Yang and H. K. D. H. Bhadeshia, “Austenite grain size and the martensite-start temperature,” *Scr. Mater.*, vol. 60, no. 7, pp. 493–495, 2009.

[61] W. Q. Cao, C. Wang, J. Shi, M. Q. Wang, W. J. Hui, and H. Dong, “Microstructure and mechanical properties of Fe-0.2C-5Mn steel processed by ART-annealing,” *Mater. Sci. Eng. A*, vol. 528, no. 22–23, pp. 6661–6666, 2011.

[62] A. Arlazarov, M. Gouné, O. Bouaziz, A. Hazotte, G. Petitgand, and P. Barges, “Evolution of microstructure and mechanical properties of medium Mn steels during double annealing,” *Mater. Sci. Eng. A*, vol. 542, pp. 31–39, 2012.

[63] J. Han and Y. K. Lee, “The effects of the heating rate on the reverse transformation mechanism and the phase stability of reverted austenite in medium Mn steels,” *Acta Mater.*, vol. 67, pp. 354–361, 2014.

[64] E. J. Seo, L. Cho, Y. Estrin, and B. C. De Cooman, “Microstructure-mechanical properties relationships for quenching and partitioning (Q&P) processed steel,” *Acta Mater.*, vol. 113, pp. 124–139, 2016.

[65] A. Arlazarov, M. Ollat, J. P. Masse, and M. Bouzat, “Influence of partitioning on mechanical behavior of Q&P steels,” *Mater. Sci. Eng. A*, vol. 661, pp. 79–86, 2016.

[66] F. HajyAkbary *et al.*, “Analysis of the mechanical behavior of a 0.3C-1.6Si-3.5Mn (wt%) quenching and partitioning steel,” *Mater. Sci. Eng. A*, vol. 677, pp. 505–514, 2016.

[67] A. Bhattacharya, P. K. Bokinala, R. Mitra, and D. Chakrabarti, “Relative effect of C and Mn on strength-toughness of medium Mn steels,” *Mater. Sci. Technol. (United Kingdom)*, vol. 35, no. 1, pp. 55–67, 2019.

[68] Z. C. Li, H. Ding, R. D. K. Misra, and Z. H. Cai, “Microstructure-mechanical property relationship and austenite stability in medium-Mn TRIP steels: The effect of austenite-reverted transformation and quenching-tempering treatments,” *Mater. Sci. Eng. A*, vol. 682, no. November 2016, pp. 211–219, 2017.

[69] A. Zarei Hanzaki, P. D. Hodgson, and S. Yue, “Retained austenite characteristics in thermomechanically processed Si-Mn transformation-induced plasticity steels,” *Metall. Mater. Trans. A Phys. Metall. Mater. Sci.*, vol. 28, no. 11, pp. 2405–2414, 1997.

[70] E. V. Pereloma, I. B. Timokhina, M. K. Miller, and P. D. Hodgson, “Three-dimensional atom probe analysis of solute distribution in thermomechanically processed TRIP steels,” *Acta Mater.*, vol. 55, no. 8, pp. 2587–2598, 2007.

[71] J. Wang and S. Van der Zwaag, “Stabilization mechanisms of retained austenite in transformation-induced plasticity steel,” *Metall. Mater. Trans. A Phys. Metall. Mater. Sci.*, vol. 32, no. 6, pp. 1527–1539, 2001.

[72] E. Jimenez-Melero *et al.*, “Martensitic transformation of individual grains in low-alloyed TRIP steels,” *Scr. Mater.*, vol. 56, no. 5, pp. 421–424, 2007.

[73] I. Y. Pyshmintsev, M. De Meyer, B. C. De Cooman, R. A. Savray, V. P. Shveykin, and M. Vermeulen, “The influence of the stress state on the plasticity of transformation induced plasticity-aided steel,” *Metall. Mater. Trans. A*, vol. 33, no. 6, pp. 1659–1667, Jun. 2002.

[74] T. Nyyssönen, M. Isakov, P. Peura, and V. T. Kuokkala, “Iterative Determination of the Orientation Relationship Between Austenite and Martensite from a Large Amount of Grain Pair Misorientations,” *Metall. Mater. Trans. A Phys. Metall. Mater. Sci.*, vol. 47, no. 6, pp. 2587–2590, 2016.

[75] V. Javaheri, S. Kolli, B. Grande, and D. Porter, “Insight into the induction hardening behavior of a new 0.40% C microalloyed steel: Effects of initial microstructure and thermal cycles,” *Mater. Charact.*, vol. 149, pp. 165–183, 2019.

[76] V. Javaheri, A. Pohjonen, J. I. Asperheim, D. Ivanov, and D. Porter, “Physically based modeling, characterization and design of an induction hardening process for a new slurry pipeline steel,” *Mater. Des.*, vol. 182, p. 108047, Nov. 2019.

[77] D. J. Dyson and B. Holmes, “Effect of alloying additions on the lattice parameter of austenite,” *J. Iron Steel Inst.*, vol. 208, pp. 469–474, 1970.

[78] N. H. Van Dijk *et al.*, “Thermal stability of retained austenite in TRIP steels studied by synchrotron X-ray diffraction during cooling,” *Acta Mater.*, vol. 53, no. 20, pp. 5439–5447, 2005.

[79] S. S. Babu *et al.*, “In-situ observations of lattice parameter fluctuations in austenite and transformation to bainite,” *Metall. Mater. Trans. A Phys. Metall. Mater. Sci.*, vol. 36, no. 12, pp. 3281–3289, 2005.

[80] V. Ratia, I. Miettunen, and V.-T. Kuokkala, “Surface deformation of steels in impact-abrasion: The effect of sample angle and test duration,” *Wear*, vol. 301, no. 1–2, pp. 94–101, Apr. 2013.

[81] J. Hidalgo, C. Celada-Casero, and M. J. Santofimia, “Fracture mechanisms and microstructure in a medium Mn quenching and partitioning steel exhibiting macrosegregation,” *Mater. Sci. Eng. A*, vol. 754, no. March, pp. 766–777, 2019.

[82] D. P. Koistinen and R. E. Marburger, “A general equation prescribing the extent of the austenite-martensite transformation in pure iron-carbon alloys and plain carbon steels,” *Acta Metall.*, vol. 7, pp. 59–60, 1959.

[83] S. M. C. van Bohemen and J. Sietsma, “Martensite formation in partially and fully austenitic plain carbon steels,” *Metall. Mater. Trans. A Phys. Metall. Mater. Sci.*, vol. 40, no. 5, pp. 1059–1068, 2009.

[84] S. Sakui, T. Sakai, and K. Takeishi, “HOT DEFORMATION OF AUSTENITE IN A PLAIN CARBON STEEL.,” *Trans Iron Steel Inst Jpn*, vol. 17, no. 12, pp. 718–725, 1977.

[85] C. M. Sellars and G. J. Davies, “Hot working and forming processes : proceedings of an International Conference on Hot Working and Forming Processes,” 1980, pp. 3–15.

[86] L. P. Karjalainen, M. C. Somani, D. A. Porter, and R. A. Morgridge, “Development of a new regression model for the recrystallisation kinetics of hot-deformed austenite,” in *The 5th International ESAFORM Conference on Material Forming*, 2002, pp. 603–607.

[87] M. C. Somani, L. P. Karjalainen, D. A. Porter, and R. A. Morgridge, “Regression Modeling of the Recrystallisation Kinetics of Austenite,” in *International Conference on Thermomechanical Processing: Mechanisms, Microstructure and Control*, 2003, pp. 436–441.

[88] A. J. Kaijalainen, P. P. Suikkanen, T. J. Limnell, L. P. Karjalainen, J. I. Kömi, and D. A. Porter, “Effect of austenite grain structure on the strength and toughness of direct-quenched martensite,” *J. Alloys Compd.*, vol. 577, no. SUPPL. 1, pp. S642–S648, 2013.

[89] J. Hannula *et al.*, “Effect of Boron on the Strength and Toughness of Direct-Quenched Low-Carbon Niobium Bearing Ultra-High-Strength Martensitic Steel,” *Metall. Mater. Trans. A Phys. Metall. Mater. Sci.*, vol. 48, no. 11, pp. 5344–5356, 2017.

[90] J. Chiang, B. Lawrence, J. D. Boyd, and A. K. Pilkey, “Effect of microstructure on retained austenite stability and work hardening of TRIP steels,” *Mater. Sci. Eng. A*, vol. 528, no. 13–14, pp. 4516–4521, May 2011.

[91] M. Soleimani, A. Kalhor, and H. Mirzadeh, “Transformation-induced plasticity (TRIP) in advanced steels: A review,” *Mater. Sci. Eng. A*, vol. 795, no. August, 2020.

[92] M. C. Somani, D. A. Porter, L. P. Karjalainen, and R. D. K. Misra, “On Various Aspects of Decomposition of Austenite in a High-Silicon Steel

during Quenching and Partitioning," *Metall. Mater. Trans. A Phys. Metall. Mater. Sci.*, vol. 45, no. 3, pp. 1247–1257, 2014.
[93] A. Kaijalainen, N. Vähäkuopus, M. Somani, S. Mehtonen, D. Porter, and J. Kömi, "The Effects of Finish Rolling Temperature and Niobium Microalloying on the Microstructure and Properties of a Direct Quenched High-Strength Steel," *Arch. Metall. Mater.*, vol. 62, no. 2, pp. 619–626, 2017.
[94] C. Celada-Casero, C. Kwakernaak, J. Sietsma, and M. J. Santofimia, "The influence of the austenite grain size on the microstructural development during quenching and partitioning processing of a low-carbon steel," *Mater. Des.*, vol. 178, 2019.
[95] F. G. Wilson and T. Gladman, "Aluminium nitride in steel," *Int. Mater. Rev.*, vol. 33, no. 1, pp. 221–286, Jan. 1988.
[96] C. Y. Wang, J. Shi, W. Q. Cao, and H. Dong, "Characterization of microstructure obtained by quenching and partitioning process in low alloy martensitic steel," *Mater. Sci. Eng. A*, vol. 527, no. 15, pp. 3442–3449, 2010.
[97] A. di Schino *et al.*, "Manganese Effect on Q&P CMnSi Steels," *Mater. Sci. Forum*, vol. 879, no. January, pp. 430–435, 2016.
[98] B. B. He and M. X. Huang, "On the Mechanical Stability of Austenite Matrix After Martensite Formation in a Medium Mn Steel," *Metall. Mater. Trans. A Phys. Metall. Mater. Sci.*, vol. 47, no. 7, pp. 3346–3353, 2016.
[99] X. Tan, Y. Xu, X. Yang, Z. Liu, and D. Wu, "Effect of partitioning procedure on microstructure and mechanical properties of a hot-rolled directly quenched and partitioned steel," *Mater. Sci. Eng. A*, vol. 594, pp. 149–160, 2014.
[100] X. Zhang, G. Miyamoto, T. Kaneshita, Y. Yoshida, Y. Toji, and T. Furuhara, "Growth mode of austenite during reversion from martensite in Fe-2Mn-1.5Si-0.3C alloy: A transition in kinetics and morphology," *Acta Mater.*, vol. 154, pp. 1–13, 2018.
[101] C. Song, H. Yu, L. Li, T. Zhou, J. Lu, and X. Liu, "The stability of retained austenite at different locations during straining of I&Q&P steel," *Mater. Sci. Eng. A*, vol. 670, pp. 326–334, 2016.
[102] K. Wang *et al.*, "Toughening optimization on a low carbon steel by a novel Quenching-Partitioning-Cryogenic-Tempering treatment," *Mater. Sci. Eng. A*, vol. 743, no. 3, pp. 259–264, 2019.
[103] J. Sun and H. Yu, "Microstructure development and mechanical properties of quenching and partitioning (Q&P) steel and an incorporation of hot-dipping galvanization during Q&P process," *Mater. Sci. Eng. A*, vol. 586, pp. 100–107, Dec. 2013.
[104] C. Wang *et al.*, "Development of ultrafine lamellar ferrite and austenite duplex structure in 0.2C5Mn steel during ART-annealing," *ISIJ Int.*, vol. 51, no. 4, pp. 651–656, 2011.
[105] S. Jing, H. Ding, Y. Ren, and Z. Cai, "A new insight into annealing

parameters in tailoring the mechanical properties of a medium Mn steel," *Scr. Mater.*, vol. 202, p. 114019, Sep. 2021.
[106] J. Han *et al.*, "The effects of prior austenite grain boundaries and microstructural morphology on the impact toughness of intercritically annealed medium Mn steel," *Acta Mater.*, vol. 122, pp. 199–206, 2017.
[107] O. Dmitrieva *et al.*, "Chemical gradients across phase boundaries between martensite and austenite in steel studied by atom probe tomography and simulation," *Acta Mater.*, vol. 59, no. 1, pp. 364–374, Jan. 2011.
[108] D.-W. Suh and S.-J. Kim, "Medium Mn transformation-induced plasticity steels: Recent progress and challenges," *Scr. Mater.*, vol. 126, pp. 63–67, Jan. 2017.
[109] A. Grajcar and R. Kuziak, "Dynamic Recrystallization Behavior and Softening Kinetics in 3Mn-1.5Al TRIP Steels," in *Applications of Engineering Materials*, 2011, vol. 287, pp. 330–333.
[110] A. Grajcar and R. Kuziak, "Softening Kinetics in Nb-Microalloyed TRIP Steels with Increased Mn Content," in *Advanced Manufacturing Technology, ADME 2011*, 2011, vol. 314, pp. 119–122.

Original publications

I Kantanen, P. K., Javaheri, V., Somani, M. C., Porter, D. A., & Kömi, J. I. (2021). Effect of deformation and grain size on austenite decomposition during quenching and partitioning of (high) silicon-aluminum steels. *Materials Characterization, 171,* 110793. https://doi.org/10.1016/j.matchar.2020.110793

II Somani, M. C., Porter, D. A., Karjalainen, L. P., Kantanen, P. K., Kömi, J. I, & Misra D. K. (2019). Static recrystallization characteristics and kinetics of high-silicon steels for direct quenching and partitioning. *International Journal of Materials Research, 110 (2019) 3,* 183–193. https://doi.org/10.3139/146.111744

III Kantanen, P. K., Somani M. C., Porter D. A., Kömi, J. I., & Misra, D. K. (2018). Microstructures and mechanical properties of tough ductile ultrahigh-strength steels processed through direct quenching and partitioning. *Materials Science Forum*, *941,* 468–473. https://doi.org/10.4028/www.scientific.net/MSF.941.468

IV Kantanen, P., Somani, M., Kaijalainen, A., Haiko, O., Porter, D., & Kömi, J. (2019). Microstructural characterization and mechanical properties of direct quenched and partitioned high-aluminum and high-silicon steels. *Metals*, *9*(2), 256. https://doi.org/10.3390/met9020256

V Haiko, O., Somani, M., Porter, D., Kantanen, P., Kömi, J., Ojala, N., & Heino, V. (2018). Comparison of impact-abrasive wear characteristics and performance of direct quenched (DQ) and direct quenched and partitioned (DQ&P) steels. *Wear*, *400–401*, 21–30. https://doi.org/10.1016/j.wear.2017.12.016

VI Kantanen, P., Anttila, S., Karjalainen, P., Latypova, R., Somani, M., Kaijalainen, A., & Kömi, J. (2022). Microstructures and mechanical properties of three medium-Mn steels processed via quenching and partitioning as well as austenite reversion heat treatments. *Materials Science & Engineering: A*, 847, (2022), 143341. https://doi.org/10.1016/j.msea.2022.143341

Original publications are not included in the electronic version of the dissertation.

[1] https://creativecommons.org/licenses/by/4.0/

857. Sone, Su Pyae (2022) Proactive resource allocation in spectrum sharing with radar systems via ML-based wireless network time series forecasting

858. Huynh, Lam (2022) From 3D sensing to dense prediction

859. Ismail, (2022) Monitoring ecohydrological process and forest dynamics in a tropical peatland

860. Juntti, Mirva (2022) Public service productization : a constructive approach on research, development and innovation process of University of Applied Sciences

861. Nikula, Riku-Pekka (2022) Automated methods for vibration-based condition monitoring of rotating machines

862. Bhattacharjee, Joy (2022) Assessment of changes in hydrology and water quality in peat-dominated catchments due to foreseen changes in bioeconomy-driven landuses

863. Keikkala, Ville (2022) Development of vertical stirred mill grinding disc and chamber design : effect on grinding efficiency and media behaviour and laboratory to plant size scale-up study

864. Tervo, Henri (2023) Non-metallic inclusions in steels and their effect on the toughness and ductility : ultra-high-strength steels and high strength offshore steels

865. Siponkoski, Tuomo (2022) Advanced piezoelectric composites : development and properties

866. Shi, Henglin (2023) Learning-based human action and affective gesture analysis

867. Pálvölgyi, Petra (2023) Synthesis of porous dielectric materials for future wireless high frequency applications

868. Kovacevic, Ivana (2023) Advanced network slicing and computational offloading for latency limited communications

869. Ikkala, Lauri (2023) Airborne remote sensing as a tool for monitoring topographical and hydrological changes on northern degraded and restored peatlands

870. Virpiranta, Hanna (2023) Development of biological treatment for sulfate- and metals-containing cold mining-impacted waters

871. Alzaza, Ahmad (2023) Cementitious binders for construction in northern cold regions

Book orders:
Virtual book store
https://verkkokauppa.omapumu.com/fi/

UNIVERSITY OF OULU P.O. Box 8000 FI-90014 UNIVERSITY OF OULU FINLAND

ACTA UNIVERSITATIS OULUENSIS

ISBN 978-952-62-3606-3 (Paperback)
ISBN 978-952-62-3607-0 (PDF)
ISSN 0355-3213 (Print)
ISSN 1796-2226 (Online)

UNIVERSITY OF OULU